# The Precipitation Hardening and Annealing Behavior of a Laminated Al Alloy System

By

Lihua Liao

A thesis
presented to the University of Waterloo
in fulfillment of the
thesis requirement for the degree of
Doctor of Philosophy
in
Mechanical Engineering

Waterloo, Ontario, Canada, 2013

## Author’s Declaration

I hereby declare that I am the sole author of this thesis. This is a true copy of the thesis, including any required final revisions, as accepted by my examiners.

I understand that my thesis may be made electronically available to the public.

## Abstract

The laminated system processed using Fusion$^{TM}$ technology is reported to contain a compositional gradient between the different layers. The interface region exhibits various precipitation characteristic during the subsequent heat treatment. The precipitation behavior at the interface region and core layer of a laminated AA3xxx-AA6xxx alloy system is investigated and discussed. The precipitation hardening capacity at the interface region is shown to scale with the existing compositional gradient. TEM observations reveal the precipitates at the interface region with a larger size and a lower number density than those at the core layer. A yield strength model developed for bulk AA6xxx series is employed to predict precipitate hardening behavior of the laminated sheet, and the modeling result shows an agreement with the measured values using a mass correction.

The annealing behavior of the laminated system is investigated in a wide temperature range and at various deformation levels. The size and aspect ratio of the recrystallized grains are found to be determined by the interaction between recrystallization and precipitation, and by dissolution/coarsening of pre-existing precipitates. Under the condition of a low annealing temperature and a high deformation level, recrystallization initiates first at the interface region and then progresses into the core layer along the compositional gradient. The preferential onset of recrystallization at the interface is attributed to a higher driving pressure and a lower Zener drag pressure due to a low volume fraction of precipitates. Nucleation from large particles and grain boundaries is found to be operative nucleation mechanism in this system.

# Acknowledgements

I would like to acknowledge and extend my sincere thanks to my advisor Dr. Esmaeili. I appreciate her comprehensive guidance, support during my Ph.D. study. I am also very grateful for her help with my personal life.

Dr. Haiou Jin, Dr. Xiang Wang, and Dr. Vahid Fallah are warmly thanked for their invaluable contribution to EBSD and TEM studies. I also would like to thank Dr. Fred Pearson, Dr. Julia Huang, and Mr. Gong from Canadian Center for Transmission Electron Microscopy, McMaster University for helping me with TEM observation and preparation of TEM films and foils.

Many thanks to Drs. Mati Raudsepp and Edith Czech of the Dept. of Earth and Ocean Sciences, UBC, for conducting the EPMA tests. This work would also not be possible without assistance from people who have helped me. They are Panthea Sepeherband, Brain Langelier, Nasim Bakhi Zadeh, Yuquang Ding, Peng Peng.

The following support for this work was from Ontario Ministry of Research and Innovation, University of Waterloo, Natural Sciences and Engineering Research Council of Canada (NSERC), and Novelis Inc.

Finally, I would like to thank my family for their support, love, encouragement and understanding. I would like to dedicate this work to my parents, my husband, and my daughter for always being there for me.

# Table of Contents

## List of Figures

# List of Tables

# Chapter 1 Introduction

In this chapter, the application of Al sheets and the fabrication technology of the studied laminated sheet are first introduced. The precipitation and recrystallization behavior of the two different layers are then reviewed. After a brief summary of the current studies of the laminated sheet, the scope and objectives of the work are given in detail.

## 1.1 The application and fabrication of laminated Al sheets

With the increasing demand for energy conservation and emissions control, aluminum alloys have become more attractive to the automotive industry due to their high strength, low density, good formability, and good corrosion resistance [1–4]. Aluminum sheets are of particular interest to replace steel in vehicles. This replacement in mainstream cars can be realized if various cost and processing-property related issues can be addressed. Choices of Al alloys, temper and fabrication processes can be manipulated to satisfy the demands of specific applications to achieve  a wide range of properties [2]. However, intensive research in the composition-processing-structure relationship is needed for a successful outcome.

Cladding of alloy sheets has been used for many years to impart combinations of certain properties that cannot be achieved in a monolithic material to the cladded sheet. During the last several decades, many methods of producing clad Al products, including roll bonding, diffusion bonding, explosive cladding, and continuous casting, have been developed [5–12]. However, the adherence issue of the mating surface between the clad and core layers could

not be resolved properly, thus limiting the improvement of the strength of the laminated sheets [13]. To overcome such a challenge, a new technology that allows commercial production of multi-alloy aluminum ingots to be obtained by simultaneous solidification of multi alloy layers into a single aluminum rolling ingot, has been recently introduced by Novelis [14]. By its traditional direct-chill mold with extra heat removal apparatus, as shown in Figure 1-1, the bi-layer ingots are free of inclusions, oxide films and porosity between the layers [15]. The multi-layer ingots can then to be processed by the same hot and cold rolling routes used for conventional monolithic alloys. The particular advantage of such a laminated system is the enhanced ductility/bendability [16].

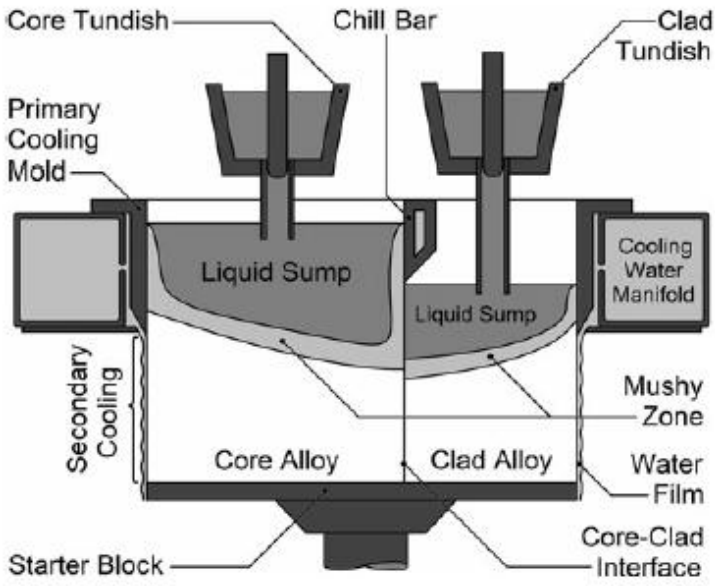


Figure 1-1. Schematic presentation of the Novelis Fusion$^{TM}$ technology casting apparatus [17].

## 1.2 Precipitation hardening of Al alloys

The high strength that can be achieved in Al alloys is due to the precipitation hardening during aging processes. The precipitates act as obstacles to the moving dislocations thus improving the yield strength of Al alloys [18]. The strength of precipitation hardenable Al alloys is well-known to be closely connected to the size, number density, and volume fraction of precipitate phases [19]. Heat treatable Al-Mg-Si-(Cu), i.e. AA6xxx alloys, are an important group of aluminum alloys that can be significantly strengthened through age hardening [20,21]. The types of precipitates and precipitation sequence have been extensively studied for Al-Mg-Si-(Cu) systems. The results have shown that multiple metastable phases are formed during aging, and that the characteristics depends on the alloy composition and the aging stage [22–33]. The modeling of precipitation kinetics and precipitation hardening of Al alloys have been well developed [30,34–43]. Using different approaches, the evolution of the mean radius and the size distribution of particles during aging has been modeled in several studies [36,37,39]. The yield strength of Al alloys has also been successfully modeled by applying the dislocation theory of precipitation hardening, and precipitation kinetics concepts [40–43].

## 1.3 Annealing behavior of Al alloys

The recrystallization behavior of Al alloys has been the subject of many studies in the past [44–56]. These studies have been intensively focused on the effect of precipitation during annealing and the role of second phase particles on the recrystallization behavior [52–56].

During annealing, precipitation and recrystallization can occur simultaneously or in sequence, depending on their kinetics at the annealing temperatures and the deformation levels [52,53]. It has been reported that when precipitation takes place prior to recrystallization, the onset of recrystallization is retarded due to a decreased driving pressure, and the recrystallized grain structure is considerably affected by the newly-formed precipitates due to the anisotropic Zener pinning pressure during annealing [57–65]. The effect of pre-existing second phase particles on the recrystallization characteristics are affected by the distribution, volume fraction, and size of particles, and particle-matrix interfacial energy [52,53,66]. Although very coarse and largely-spaced particles have little effect on the grain boundary pinning, their presence prior to deformation may significantly affect the recrystallized microstructure due to the well-known particle stimulated nucleation (PSN) effect [49,52,54]. The effect of solutes on the mobility of grain boundaries has also been the subject of a number of studies [52,67–76]. Solutes also exert a pinning pressure on the moving boundary by increasing the activation energy for grain boundary mobility [52,68,70,73]. However, the level of pinning can significantly vary with the alloy composition [68].

The recrystallization behavior of monolithic AA3xxx and AA6xxx alloys has also been the subject of many studies [61,63,64,77–83]. Those investigations have found that the pre-existing fine particles and solutes have strong effects on the recrystallization behavior under different levels of deformations. Precipitation of Mn-containing particles during the annealing of supersaturated Al-Mn alloys is reported to strongly retard recrystallization and

lead to a coarse elongated recrystallized grain structure [60,61,64,77]. The elongated grain structure of the recrystallized Al-Mn alloy has been shown to be caused by pinning effects from those precipitates that nucleate heterogeneously on the boundaries with large misorientations during the initial stage of annealing [61,64]. The precipitation in a supersaturated Al-Mn alloy has been demonstrated to first take place preferentially at grain boundaries with high angles, while it occurs at the low angle boundaries at a longer annealing time [61].

It is also reported that the precipitation before recrystallization is responsible for the elongated grain structure, while at high temperatures equiaxed grain structure is obtained due to the faster kinetics of recrystallization [77]. The interaction between precipitation and recrystallization in precipitation-hardening Al-Mg-Si alloys has also been the subject of several studies [39, 52, 53]. Recrystallization temperature has been reported to increase due to the pinning of precipitates, and the recrystallized grain structure can be elongated or equiaxed depending on the distribution of precipitates formed before the initiation of recrystallization [84,85]. Due to the complex precipitation reaction in the Al-Mg-Si-(Cu) system, the effect of precipitation on the related recrystallized grain structure is concluded to be determined by the distribution of the possible precipitates (including β″, β′, and $Mg_2Si$) and their size before recrystallization [86,87]. The nucleation phenomenon in recrystallization of both AA3xxx and AA6xxx has been investigated in a few studies so far [61,82,86,88]. However, it has been found challenging to elaborate on the mechanisms of nucleation and the occurrence of the possible mechanisms in these alloys.

## 1.4 Laminated alloy system fabricated using Fushion$^{TM}$ technology

The laminated system fabricated by Fusion$^{TM}$ technology is a promising material, in the sense that the clad layer has desirable surface properties and formability. The laminated systems therefore contain combined proprieties that cannot achieved from a monolithic material [14]. Preliminary studies on the laminated AA3xxx-AA6xxx systems have demonstrated significant enhancement of mechanical properties compared to the monolithic core alloys [16,89].

Gupta et al. [14] have studied the distribution of Mg and Si across the interface of the laminated system AA4045-X900 (Al-1.5 wt.% Mn-0.6 wt.% Cu-0.2 wt.% Mg-0.2 wt.% Fe) produced using Fusion$^{TM}$ technology, and it demonstrated that new particles form due to the diffusion of Si and Mn. The laminated system AA3xxx-AA6xxx has also been studied and modeled for compositional characteristics of the interface region in both the hot rolled condition, and hot rolled and solutionized conditions by Foroozmehr and co-workers. They have shown that a compositional gradient exists in the hot rolled samples, and this compositional gradient at the interface region leads to a fast dissolution of particles at the interface region than at the core layer during the solution treatment [90].

The laminated alloys system AA3xxx-AA6xxx was processed using Fusion$^{TM}$ technology with AA3xxx as the clad layer and AA6xxx as the core layer in a lab scale. It is a system containing a core layer (AA6xxx) that can be strengthened by aging, and a clad layer (AA3xxx) that does not show age hardening, but has high ductility. The through-thickness microstructures of the annealed laminated sheet can have significant influence on their

formability. Therefore, the application of laminated sheets for automotive panels requires thorough investigations of their recrystallization and precipitation behavior. However, there has been a lack of research investigations on the precipitation and recrystallization behavior of the laminated sheets, since most of the work has been on focused on the cladding process itself or the mechanical properties of the final products [5–9,11,12,91–95]. The studies on the recrystallization of the laminated sheets are also limited to the combination of pure metals [96–98].

It is well known that precipitation kinetics varies with the composition of the material, and finally leads to different distributions of precipitates for the materials with composition variations (i.e. laminated sheets and gradient materials). The precipitation behavior and precipitation modeling on such materials are of importance and have not been studied for Al alloys. The complexity of precipitation arising in the presence of a compositional gradient across the interface region can significantly affect the recrystallization behavior of the laminated sheet. Therefore, gaining a more thorough and in-depth knowledge of the aging and annealing behavior of the laminated sheets with precipitation hardening capacity is essential to optimize the thermal-mechanical processes and their potential future use. The new knowledge can also be helpful in designing novel combinations of alloys for future laminated Al alloy products.

## 1.5 Scope and Objectives

The objectives of this research are to (a) study the precipitate distribution and precipitation hardening of the interface region and core layer of the laminated AA3xxx-AA6xxx system with special emphasis on the interface featuring composition gradients of solutes participating precipitation, (b) investigate the annealing behavior of different layers of the laminated sheet under various deformation levels and annealing temperatures, (c) provide a fundamental approach for studying and understanding the precipitation and annealing behavior associated with compositional gradients of the multilayer materials with precipitation capacity. The current research is the first to study the precipitation and annealing behavior of a laminated sheet fabricated using Fusion$^{TM}$ technology. With the research findings, new combinations of laminated sheets and proper thermal mechanical processes can be designed in order to achieve optimum properties.

The above objectives are achieved through conducting the following investigations:

1. The precipitates and precipitation hardening of the aged laminated sheet, including both the AA6xxx core layer and the interface region, are characterized. The precipitation hardening of the core layer and interface between the clad and core layers is studied by hardness measurement on the surface defined by the rolling and normal directions during aging. The microstructure is examined using transmission electron microscopy to reveal the precipitation characteristics of the core layer and interface region. The composition gradient of the interface region is characterized using electron probe micro-analysis. The precipitation kinetics and precipitation

hardening are also studied using differential scanning calorimetry, isothermal calorimetry and a yield strength modeling.

2. Two different cold rolled sheets with 60% and 80% thickness reductions are employed for the study of annealing behavior. The particle distribution in the cold rolled sheets is characterized using transmission electron microscopy and scanning electron microscopy. The interface is studied and defined by the electron probe microanalysis.

3. The recrystallization behavior of the clad and core layers of the laminated sheets with various levels of deformation and annealed at different temperatures is investigated. Softening behavior during annealing is studied by hardness measurement. Characterization of recrystallized microstructure and the distribution of particles are studied by scanning electron microscopy in backscatter mode and electron backscatter diffraction. The recrystallization behavior is further studied with focus on:

    - The effect of composition gradient existing between the clad and core layers on the recrystallization behavior is investigated. Precipitation reaction during the annealing is studied using differential scanning calorimetry and scanning electron microscopy.

    - Active recrystallization nucleation mechanisms are investigated. Nucleation from large particles and grain boundaries is studied using scanning electron microscopy for both fully recrystallized and partially recrystallized conditions.

# Chapter 2 Literature review

## 2.1 Precipitation in AA6xxx alloys

In this section, the existing literature for the precipitation behavior of AA6xxx alloys has been reviewed. The review starts with the precipitation sequence and hardening mechanisms of AA6xxx alloys. The modeling of precipitation kinetics and yield strength is then reviewed.

### 2.1.1 Precipitation phases of AA6xxx alloys

The precipitation phases in the Al-Mg-Si family have been studied intensively, and the precipitation scheme is generally accepted to occur in the following steps [20,99]:

$$\text{SSSS} \longrightarrow \text{GP Zones} \longrightarrow \beta'' \longrightarrow \beta' \longrightarrow \beta$$

where SSSS is the supersaturated solid solution. GP zones are one of the metastable precipitation phase with fully coherent interface with the matrix, and exist at an early stage of aging [20,31,100]. The precipitate β″ phase is reported as needle-shaped phase along $<100>_{Al}$ with monoclinic C-centered crystal structure. With increasing aging time, β″ precipitates grow into rod-like β′ that have a hexagonal crystal structure. The corresponding final equilibrium phase is $Mg_2Si$ (β) with cubic $Ca_2F$ structure [31].

With the addition of Cu, the mechanical properties of the AA6xxx series have been improved significantly, and the precipitation phases and their sequence have become more complex. Due to the addition of Cu, the quaternary Q phase is reported for Al-Mg-Si-Cu system, and

metastable Q″ and Q′ are the precursors of the lath-shaped stable phase Q containing Al, Cu, Mg, and Si [21,24,26,101]. The phases Q″, Q′ and Q are reported to exist at different aging stages with various crystal structures and shapes [101]. The precipitation sequence of AA6111 has been investigated at different aging conditions using differential scanning calorimetry (DSC), and the precipitation sequence has been suggested as [101]:

$$\text{SSSS} \longrightarrow \text{GP Zones} \longrightarrow \beta'' \text{ and } Q'' \longrightarrow Q' \text{ and } \beta' \text{ (or } \beta') \longrightarrow Q \text{ and } \beta$$

Both β″ and Q′ are reported to be precipitation hardening phases in Al-Mg-Si-Cu family. TEM results have shown that β″ exists in a considerably larger number density than the Q′ phase in AA6111 aged at 180 $^{o}$C for 15 mins, 30 mins, 1 h and 7 hrs [101].

### 2.1.2 **Interaction between precipitates and dislocations**

Precipitates can act as obstacles to the moving dislocations during deformation, in which yield strength is improved. The fundamental strengthening mechanism for precipitation hardening depends on the nature of interaction between precipitates and dislocations [18,42]. There are two main types of precipitation-dislocation interaction mechanisms: the shearing mechanism and the Orowan mechanism. Precipitates are cut by a gliding dislocation and leave fractured precipitates behind. Dislocations bow out between the precipitates and rejoin together by leaving dislocation loops around the particles [102]. In a recent study on the Al-Mg-Si-Cu alloy, it has been shown that precipitates which form at early stages are shearable and precipitates which form at the later stages of aging are non-shearable [42,103]. For a

shearing mechanism system, the possible precipitates are GP zones and β″. When precipitates are larger and widely spaced, they are by-passed instead of being cut by moving dislocations.

The transition from shearable to non-shearable precipitates during the aging process is controlled by the nature of the precipitates. In the research conducted on AA 6111 [102], the slip lines with fractured precipitate are observed for under-aged and peak-aged samples, which indicates shearing mechanism takes place. The over-aged sample with precipitates shows no such evidence of shearing mechanism due to the larger size of precipitates. Esmaeili's yield strength model on AA 6111 [41] shows a good match with experimental results by assuming shearable precipitates at under-aged and peak-aged conditions.

### 2.1.3 **Precipitation hardening modeling**

Precipitation hardening modeling has been intensively studied for Al alloys with various precipitation kinetics models [30,35,37,38,40–43,99,104]. The precipitation nucleation rate is well agreed to be varied during aging with a specific incubation time [36]. The driving pressure for nucleation is proportional to the concentration of the matrix [52]. The growth rate of precipitates is suggested to be proportional to the diffusion coefficient and the compositional gradient formed at the interface between the precipitate and the matrix [105]. At a constant temperature, such nucleation and growth rates delineate a C-type curve for the relationship between the starting time of precipitation and temperatures, which indicates the fastest precipitation rate is obtained at an intermediate temperature range [106]. The small

activation energy for nucleation of precipitates at a high temperature range and the reduced diffusivity at a low temperature range both attribute to a slow process of precipitation.

By different approaches, evolution of the mean radius or the size distribution of particle distribution during aging can be modeled for both isothermal aging and non-isothermal aging [35,36,39,107]. With the modeled precipitation kinetics, the yield strength of Al alloys has been well modeled by employing the theory of precipitation hardening [30,34,37,38,41].

### 2.1.4 **Precipitation in AA 3xxx alloy**

The homogenized AA3xxx alloy does not demonstrate apparent precipitation hardening during aging, since the solubility of Mn in Al is extremely low with 1.82 wt.% Mn at the eutectic temperature of 658.5$^{o}$C [108]. It has also been reported that the decomposition of supersaturated Al-Mn binary alloys is very sluggish, and precipitates display various morphologies at different temperatures [109–111]. Orthorhombic $Al_6$(Mn,Fe) and cubic Al(Mn,Fe)Si are the two dominant dispersions in the AA 3xxx alloy [108,111]. The size of dispersoids Al(Mn,Fe)Si is less than 50 nm, which indicates a high thermal stability at the investigated temperature of 375$^{o}$C for 24 h [112]. The related phase for AA3003 is calculated by Foroozmehr et al. [90] and given in Figure 2-1, and it shows $Al_6$(Mn,Fe) presents at the temperature higher than 300$^{o}$C. The fraction of Al(Mn,Fe)Si dispersoids increases with the amount of Si, and it is more stable than $Al_6$(Mn,Fe) at lower temperatures [112,113]. Addition of Cu has also been reported to enhance the decomposition of the supersaturated solid solution [26]. The work of Li et al. [112] has shown that α-Al(Mn,Fe)Si dispersoids

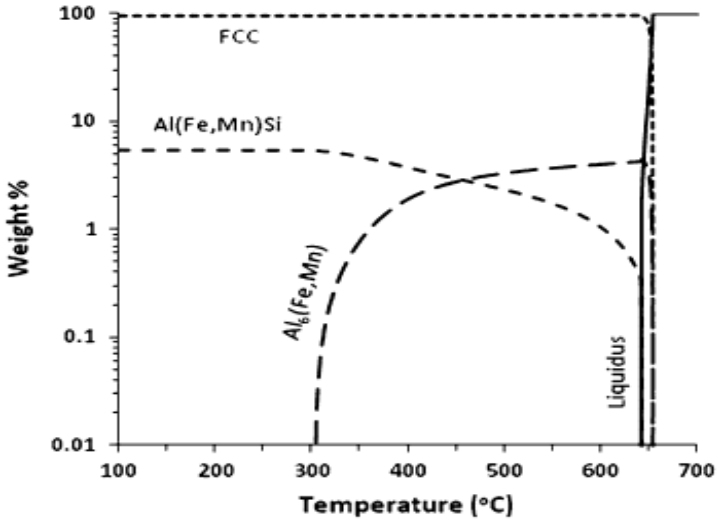


Figure 2-1. Equilibrium phases for AA3003 alloys calculated using Factsage [90].

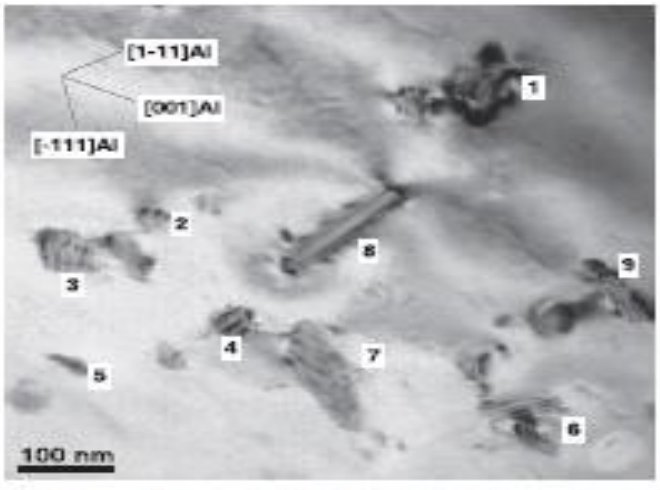


Figure 2-2. Morphology of Al(Mn,Fe)Si dispersoids in AA 3003 as heated to 500$^{o}$C <101>$_{Al}$ zone axis (block-shaped marked as 1-6, and plate-shaped marked as 7-9) [112].

formed in AA3003 during heating to 500$^{o}$C are partially coherent with the matrix as shown in Figure 2-2. Due to the partial coherence with the matrix and relatively high thermal

stability, Al (Mn, Fe)Si dispersoids are expected to play an important role in the recrystallization of AA3xxx.

## 2.2 Precipitation in deformed Al alloys

It has been well known that deformation prior to heat treatment can significantly accelerate the precipitation process by providing extra nucleation sites [114–116]. Dislocations generated by deformation provide short-cut paths for diffusion of solutes. In addition, the lattice distortion in the vicinity of dislocations assists the formation of nuclei by reducing the total strain energy of embryo [117,118]. It has been shown the peak-aged condition with the nucleation of β″ has been reached faster during the aging of a deformed AA6xxx compared to the aging of an un-deformed condition [119]. Zhen et al. [100] have suggested that the formation of GP zones and the transition of β″ into β′ are promoted by the increased density of dislocations generated by cold deformation. Similar trends have also found in AA3xxx. Chen et al. [118] has studied and modeled the effect of deformation on the precipitation behavior of $MnAl_6$ and $MnAl_{12}$ in a deformed AA3003. As depicted in Figure 2-3, it have shown that (a) precipitation on both dislocations and boundaries is accelerated; (b) with a higher density of dislocations, the nose of the C-curve shifts to a lower temperature and a shorter time; (c) the precipitation process is slightly delayed due to recovery featuring a decreasing dislocation density and (d) the initiation time for precipitation is shortened greatly compared to the homogeneous precipitation due to the micro-segregation of solute Mn at the dislocation network.

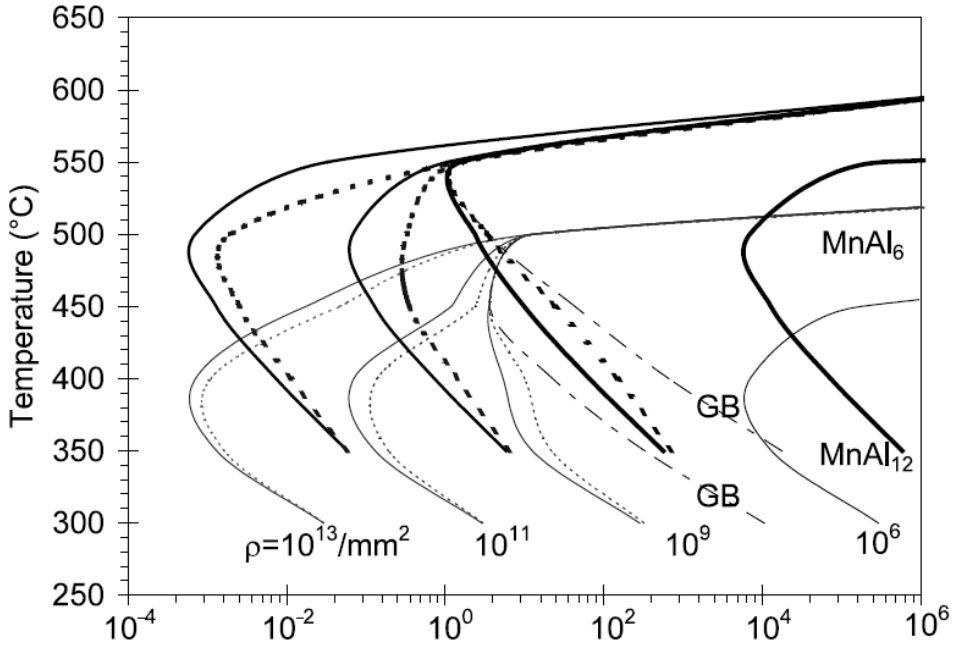


Figure 2-3. The effect of the dislocation density and recovery on the C-curve of the precipitation in AA3003. (Solid lines, dislocation effects; dotted lines, recovery effect; dash-dotted lines, grain boundary nucleation) [118].

### 2.3 Annealing of the deformed Al alloys

During cold deformation of metals and alloys, a high level of energy is stored due to the increased density of dislocations, thus giving rise to an unstable deformed microstructure [52]. During annealing, the unstable grains with a high density of dislocations inside tend to be replaced by new, undeformed grains through recovery, recrystallization and grain growth. The stored energy decreases gradually by dislocation rearrangement and annihilation during recovery. Recrystallization follows recovery in sequence, or the two steps might overlap. New dislocation-free grains form inside a deformed material during recrystallization by

consuming the deformed grains. Growth of recrystallized nuclei driven by the surface energy reduction can take place in two different ways: normal grain growth and abnormal grain growth. In the latter, only a few grains are able to grow into a much larger size. Since the beginning of the 20$^{th}$ century when the concept of recrystallization was identified [52], the fundamentals of recrystallization of pure Al have been extensively studied.

### 2.3.1 **The deformed state**

The nature of the recrystallization behavior including the formation of nuclei and their growth greatly depends on the characteristics of the deformed substructure. In this section, the deformation structure and the effect of pre-existing particles on the structure are reviewed.

During cold working, the microstructure changes with various grain shapes and sizes. An increasing area of grain boundaries is often accompanied by an increasing density of dislocations and their interaction as well [120]. A typical deformed Al microstructure is that high density of dislocations usually accumulates and forms dislocation walls [52]. Understanding the internal structure of a deformed grain is critical for comprehending the deformed structure and the following annealing behavior. It is well known that the substructure is mainly determined by the extent of cold work. For Al alloys a low rolling strain of ~0.2 usually results in a uniform-equiaxed cellular structure due to its high stacking-fault energy, [121]. With increasing rolling strain, the substructure becomes elongated with a smaller size, and the misorientation between the subgrains increases as well. The empirical

equation between the deformation strain and the size of subgrains is reported as follows [121,122]:

$$\bar{\delta} = 0.35 + 0.17/\varepsilon \qquad (2\text{-}1)$$

where $\bar{\delta}$ and $\varepsilon$ are the mean diameter of subgrains in μm and true strain, respectively. The average misorientation has also reported to increase rapidly with the strain and to follow the relationship established for cold-deformed pure Al [121]:

$$\bar{\delta}\bar{\theta}/b = N \qquad (2\text{-}2)$$

where $\bar{\theta}$, and $b$ are the mean misorientation and the magnitude of Burgers vector, respectively. $N$ is a constant. The mean size and misorientation of subgrains have also been predicted by Chen and coworkers [121] as a function of strain for cold rolled Al. It shows that both size and misorientation of the deformed grains increase with the strain, while the increasing rate is greater for a lower strain.

In addition to the deformed strain, the presence of the particles in the deformed alloys affects the subgrain structure significantly. In the case that a particle is strong enough to withstand the shear stress caused by dislocation loops around them, Orowan loops can be generated [52,53]. During cold rolled deformation, a fine dispersion of particles lead to a further increase in dislocation density and in the level of homogeneity of dislocations compared to the particle-free matrix. The increase in dislocation density during deformation arises from both the trapping of existing dislocations and the generation of new dislocations.

### 2.3.2 **Recrystallization nucleation sites**

Nucleation of new grains during recrystallization initializes at regions where have high local misorientation, and can provide high driving pressure for nucleation [52]. It has been recognized that deformation bands inside grains, shear bands, highly misoriented deformation zones around large particles and previous high angle boundaries are heterogeneities that can act as nucleation sites [52]. In most cases, more than one nucleation mechanism could take place. Various effective nucleation mechanisms might be active and follow a sequence or compete depending on the deformation conditions that includes the deformation levels and microstructure characteristics of the cold-deformed material such as the original grain size and particle distribution [123,124]. In the following section, potential operative nucleation mechanisms are discussed in detail.

*Nucleation from various bands*

During deformation, deformation bands and shear bands, which are deformation heterogeneities, can be nucleation sites during recrystallization. Deformation bands are generated by heterogeneous deformation inside a grain [52]. Multiple fragments with a single aligning direction in each region, produced through the activation of various slip systems, are called deformation bands. The aligning direction of the deformation bands to the rolling direction varies with deformation strain. Jazaeri and Humphrey's study [125] has shown that the deformation bands aligned at ~$40^{o}$ to the rolling direction of Al-0.1 wt.% Mg with a 50% thickness reduction as shown in Figure 2-4 (a). Furthermore, with a reduction of up to 70%, the deformation bands became increasing aligned with the rolling direction as shown in

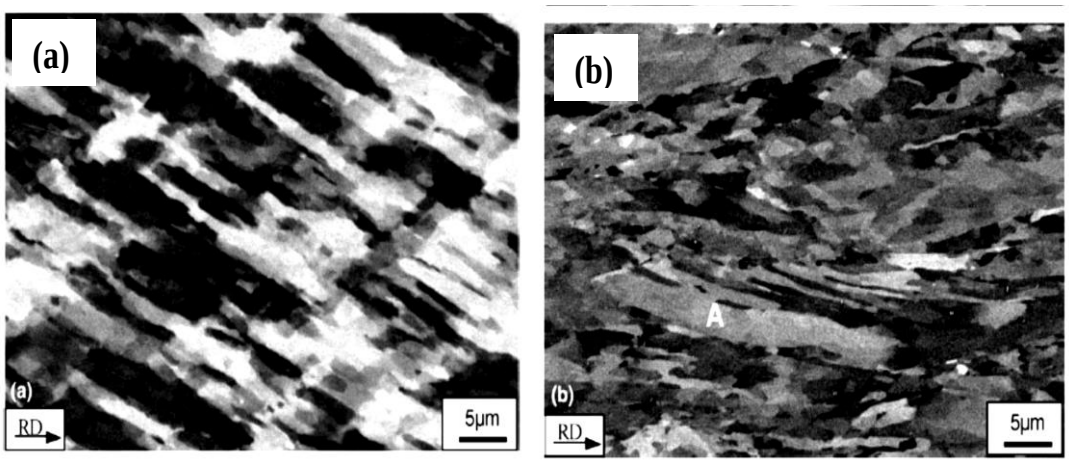


Figure 2-4. SEM backscattered images for the cold rolled Al-Mn with thickness reduction of (a) 50% and (b) 70% [125].

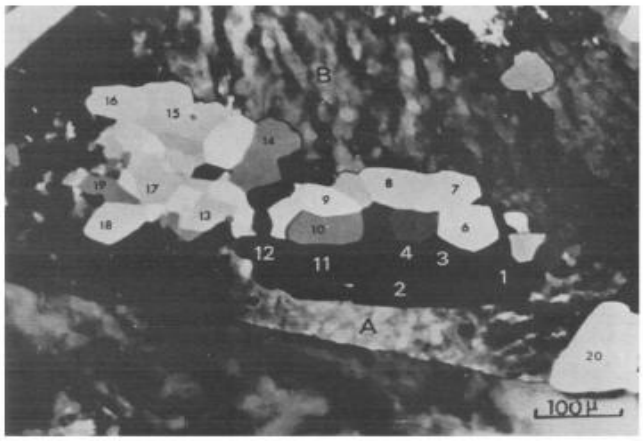


Figure 2-5. Recrystallization nucleation on a deformation band in the deformed pure Al with a 40% deformation and annealed at 328$^{o}$C for 70 mins [126].

Figure 2-4 (b). Nucleation at deformation bands of a cold-compressed pure Al was also studied, and small recrystallized grains were found to nucleate at the deformation bands as shown in Figure 2-5 [126].

Shear bands are the results of plastic instability, and are resolvable under optical microscopy at $35^{o}$ to the rolling plane and parallel to the transverse direction [52]. Shear bands have been found in a deformed Al-Mg alloy with an 85% thickness reduction as shown in Figure 2-6 (a). During annealing, those shear bands have been observed to be nucleation sites as indicated by A and B in Figure 2-6 (b) [127]. The study has also revealed that the nucleation at shear bands took place earlier than nucleation at previous boundaries [127].

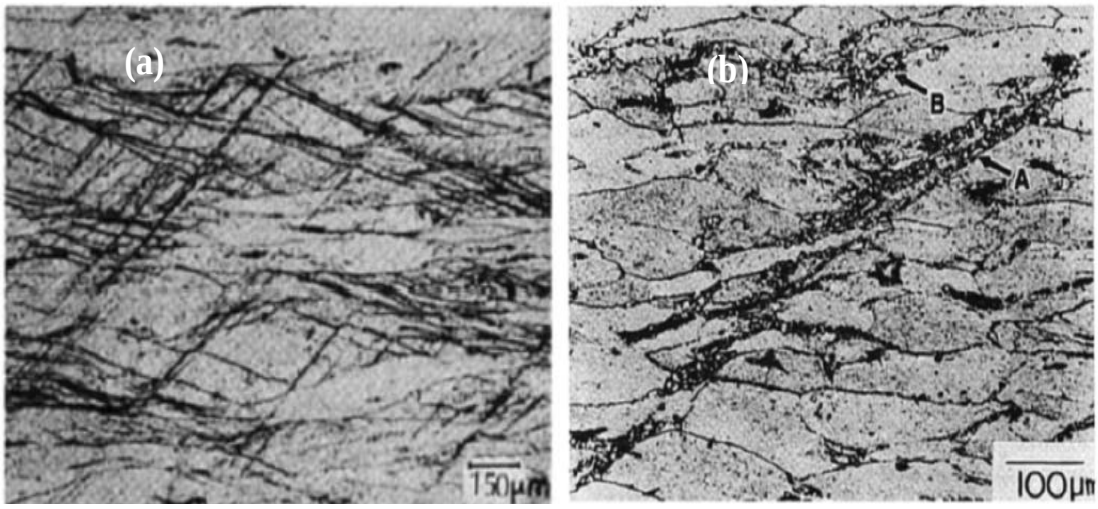


Figure 2-6. (a) shear bands produced in Al-4.8 wt. % Mg alloy and (b) nucleation at shear band after annealing at 275°C for 4.5 mins [127].

*Nucleation around large particles*

It has been well established that a coarse dispersion of large particles accelerates recrystallization by representing as nucleation sites, which is called particle stimulated nucleation (PSN) [49,52,86,123,128]. Deformation zones featuring localized and concentrated strain at the particle-matrix interface were found around large particles during

cold work, as shown in Figure 2-7. Deformation zones include two distorted regions and rotated zones. In the distorted regions, the deformed grains are elongated in the rolling direction, whereas in the rotated zones, the deformed grains are rotated and less elongated. High dislocation density and large orientation gradient have been reported in the rotated zone with the largest misorientation at the particle-matrix interface, therefore facilitating the occurrence of PSN [52].

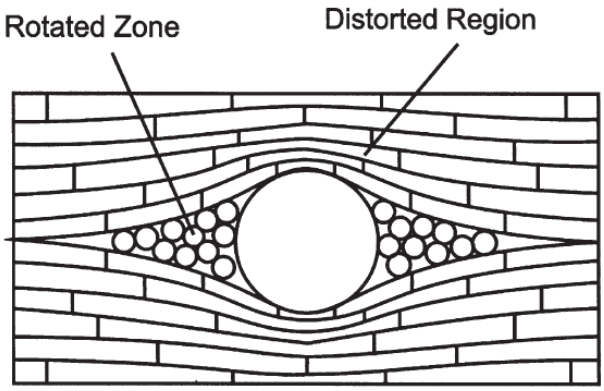


Figure 2-7. Schematic drawing of the deformation zone around a large particle [52].

It is clear that not all the pre-existing large particles can be nucleation sites during annealing. Particles must reach a critical size to be successful nucleation sites, and the critical size is smaller for a higher level of deformation. In addition to the size of large particles, it is also shown that the final recrystallized grain size is related closely to the space between large particles [129]. PSN can also take place in the area containing multiple small particles which are called particle clusters. When particles are closely distributed, the deformation zones associated with each particle can overlap and form a big joint deformation zone which

facilitates the growth of nuclei into recrystallized grains in the deformation zone [56]. In addition to the size and interparticle spacing, other factors that can increase the stored energy around large particles might facilitate PSN. Troeger and coworker [86] have suggested that particles on the interface between the deformation bands are more capable of being PSN sites than those on the grain boundaries due to their larger surface area. Furthermore, PSN has also been reported to be more effective adjacent to large particles that distribute along the previous grain boundaries due to the presence of an extraordinary energy source from the deformation bands or previous grain boundaries [130]. Sites of large particles therefore play a key role in the efficiency of PSN.

*Nucleation from original high angle boundaries*

There are two different nucleation mechanisms associated with original high angle boundaries: strain induced boundary migration (SIBM) and classical nucleation from grain boundaries. SIBM was first observed at many metals by Beck and Sperry [131]. As can be seen in Figure 2-8, by bulging of the segment of a previous grain boundary, an recrystallized area with a decreased dislocation density forms behind the moving boundaries during the annealing of a deformed pure Al with a 40% thickness reduction [126]. The new grains formed in this way have similar orientation to the parent grains that they grew from. The moving direction of the boundary can be opposite for different segments. This mechanism is generally operative at a low level of deformation. Bellier and Doherty have first confirmed that SIBM was the dominant recrystallization mechanism for pure Al with reductions lower than 20% when annealed at 328$^{o}$C for 42 hrs [126]. However, Beck and Sperry [131] have

later found that the mechanism was operative till 40% thickness reductions for pure Al. It is also reported that SIBM plays an important role during the recrystallization for a homogeneously deformed microstructure [132–136].

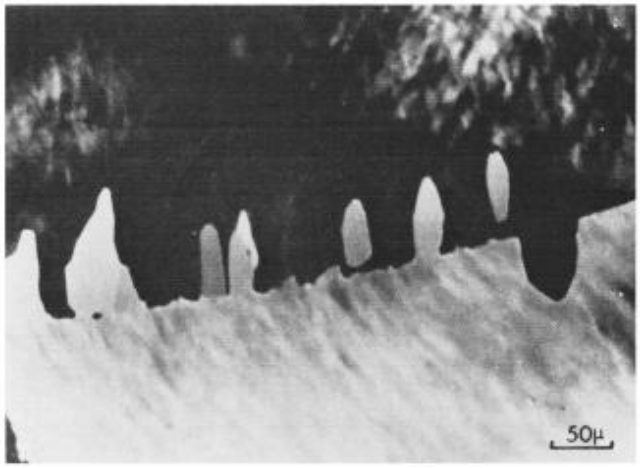


Figure 2-8. Evidence of SIBM in deformed pure Al with 40% reduction and annealed at 328$^{o}$C for 1 h [126].

SIBM may occur either by the migration of the boundary associated with several subgrains (Multiple SIBM) or by the bowing of the boundary adjacent to a single large subgrain (Single SIBM), as shown schematically in Figure 2-9 (a) and (b), respectively. Multiple SIBM is driven by the difference in the density of dislocations on the two sides of the boundaries, and is expected to take place in a deformed microstructure with a low subgrain misorientation and poorly-defined dislocation cells [52]. Single subgrain SIBM dominates in a deformed microstructure containing subgrains with misorientations larger than 1$^{o}$ and similar stored energy. In this case, there is no detectable substructure behind the bulge shown in Figure 2-9 (b). Due to the bulging of high angle boundaries, the misorientation of the neighboring

subgrains formed during cold deformation is inherited in the recrystallized grains [52]. However, there is no simple relationship between the recrystallized grains nucleated from the high angle boundaries and parent grains.

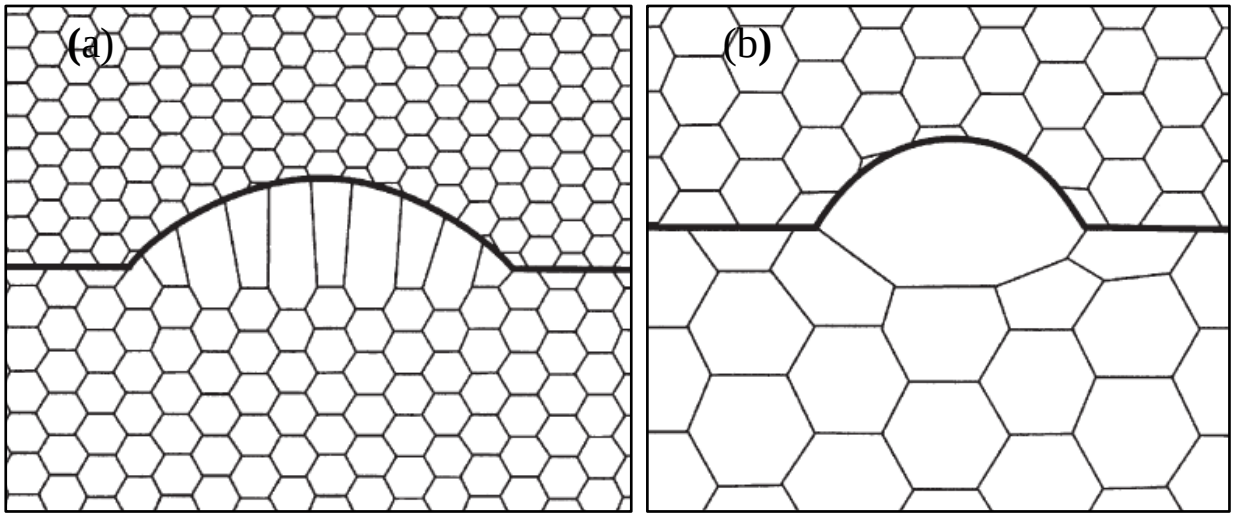


Figure 2-9. SIBM of (a) multiple subgrains and (b) single subgrain [52].

The dispersion of fine precipitates reduces the driving pressure for recrystallization and facilitates the occurrence of multiple-subgrains SIBM. A pre-existing high angle boundary with a length of up to 1 mm was found to migrate by SIBM as shown in Figure 2-10 during recrystallization of an Al-0.12 wt. % Sc alloy. An typical SIBM character affected by precipitates has been proposed by Somerday and Humphrey [61]. They have shown that the length of the bowing boundary towards the side with higher energy is limited by the pinning effect due to a dispersion of small precipitates on the boundaries. With the continuous

bowing of the boundaries, a broad recrystallized structure formed by the joining of subgrains was separated by low angle boundaries [61].

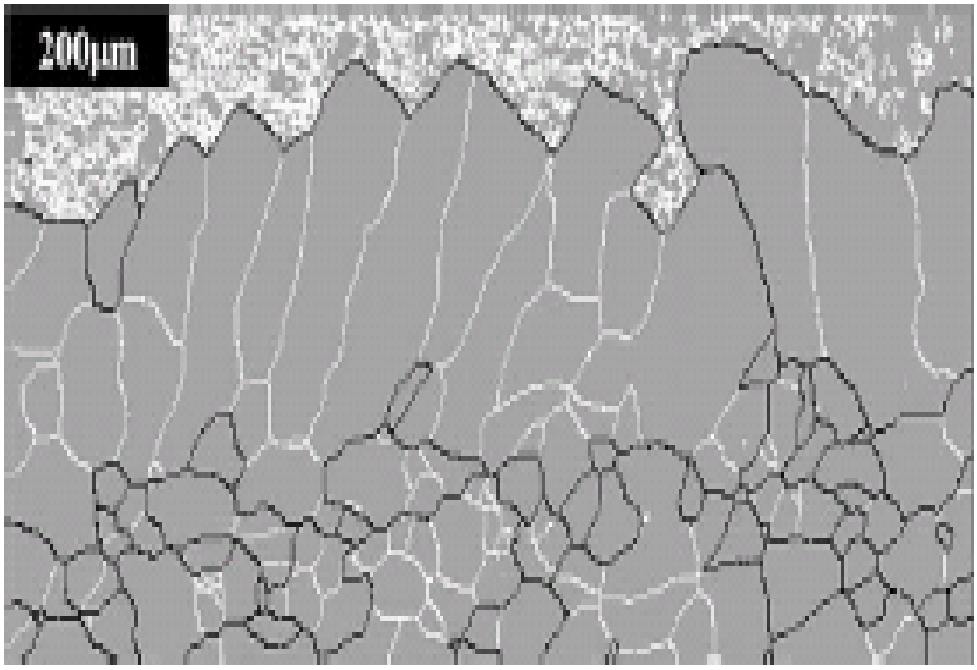


Figure 2-10. EBSD map showing broad front of SIBM in an Al-0.12 wt. % Sc sample annealed at 425$^{o}$C for 20 s. The high angle boundaries are shown as black and low angle boundaries are as white [72].

### 2.3.3 **Pinning effect from dispersions of small particles**

For an alloy system containing a dispersion of small precipitates, the pinning on grain boundaries is termed as Zener drag pressure $P_Z$. The value of $P_Z$ depends on the distribution of precipitates including the volume fraction *f* and the radius *r*. There are various forms of the equations of calculating the value of $P_z$, however, it is agreed that the amount of Zener drag

pressure is proportional to $f/r$ [52]. Due to the dispersion of small precipitates, the initiation of the recrystallization and the growth rate of recrystallized grains can be extremely retarded or even prohibited.

The Zener pinning pressure on subgrain boundaries decreases the mobility of the subgrains, which retards or even inhibits subgrains to reach the critical size. The dispersion of small particles therefore can also have an effect on the efficiency of PSN. With the presence of small precipitates, the net driving pressure $P$ is the driving pressure from the accumulated dislocations $P_D$, and reduced by the Zener drag pressure $P_Z$ as given in the following equation [52]:

$$P = P_D - P_Z \tag{2-3}$$

$$P_D = \alpha \rho G b^2 \tag{2-4}$$

where $\alpha$ is a constant, $\rho$ and $b$ are dislocation density and the magnitude of Burger's vector, $G$ is the shear modulus. The related critical size of large particles $R_{CP}$ to be effective nucleation sites when Zener drag pressure is applied follows [52,53]:

$$R_{CP} = \frac{4\,\gamma}{P_D - P_Z} \tag{2-5}$$

Based on equation (2-5), it is clear that PSN is effective with a larger size of particles with the existence of Zener drag pressure.

The overall pinning effect on two types of evolution of grain size is shown in Figure 2-11. $D_{LIM}$ and $D_N$ denote the overall recrystallized grain size and the size of recrystallized grain

nucleated by PSN, respectively. A higher volume fraction of smaller particles yields a smaller recrystallized grain size from the curve of $D_{LIM}$. On the other hand, the recrystallized grain size shows an opposite trend if PSN takes place, which is attributed to the decreased number of nuclei due to the increased critical size.

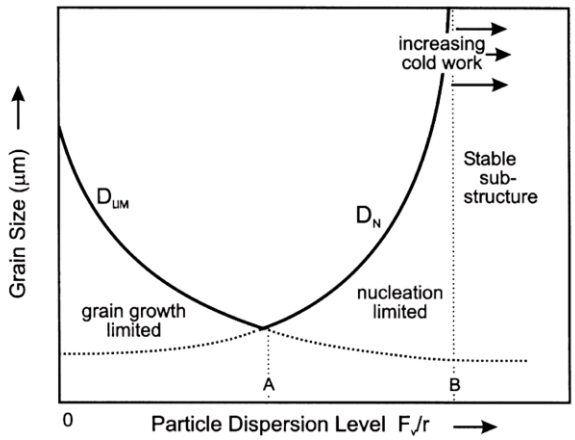


Figure 2-11. The effect of the particle parameters on the recrystallized grain size [52].

### 2.3.4 **Interaction between recrystallization and precipitation**

The effect of both large particles and small precipitates on the recrystallization behavior was explained in general in the above sections. However, the study of annealing behavior becomes more complicated due to the interaction between precipitation and recrystallization. During annealing of alloys with precipitation capability, precipitation and recrystallization can occur simultaneously or in sequence, while also affecting each other. In this section, the competition between recrystallization and precipitation, and its effect on the recrystallized microstructure are reviewed.

*Competition between recrystallization and precipitation during annealing*

The competition between precipitation and recrystallization during annealing depends on their kinetics, and both of which are affected by annealing temperatures. The time to start recrystallization $t_R$ at a annealing temperature is given by the following equation [53]:

$$t_R = k_R \cdot exp\frac{Q_R}{RT} \qquad (2\text{-}6)$$

where $k_R$ and $Q_R$ are a constant factor and the activation energy for the formation of a recrystallization front, respectively. *R* and *T* are the molar gas constant and temperature in *K*, respectively. The velocity of a recrystallized boundary *V* is given by [52]:

$$V = M(P_D - P_Z) \qquad (2\text{-}7)$$

where *M* is the boundary mobility and follows an Arrhenius relationship with temperatures [52]:

$$M = M_0 \exp(-Q/RT) \qquad (2\text{-}8)$$

where $M_0$ is a constant and Q is the activation energy. The kinetics of recrystallization increases with annealing temperatures due to a faster initiation of recrystallization and higher velocity of the recrystallized front. In addition to annealing temperatures, deformation levels increase the recrystallization kinetics due to a higher stored energy that indicates a higher driving pressure.

Precipitation generally takes place the fastest at an intermediate temperature due to a lower driving pressure for precipitation nucleation at a higher temperature and to a slower diffusion of solutes at a lower temperature [106]. A temperature $T_C$ could be found at which recrystallization and precipitation can take place at the same time, which indicates the kinetics of precipitation and recrystallization meets at the same point. Recrystallization therefore generally precedes precipitation at the temperature higher than $T_c$, whereas, precipitation precedes recrystallization in the lower temperature range.

*The effect of concurrent precipitation and recrystallization on the recrystallized grain structure*

Precipitation taking place before recrystallization and during annealing has been reported to increase the recrystallization temperature, and to have a decisive effect on the morphology of recrystallized grains [64,65,77]. When precipitation takes place before recrystallization, it decreases the driving pressure for recrystallization due to the existence of Zener drag pressure. Also the newly-formed precipitates are preferentially located at some high angle boundaries [64,137], which yields a non-uniform distribution of Zener drag pressure from the newly-formed small precipitates.

Tangen and coworkers' research on the annealing of a cold rolled AA3013 has presented that elongated recrystallized grains are found at lower annealing temperatures than *Tc* (a critical temperature below which recrystallization precedes precipitation), and equiaxed recrystallized grains are observed at a high annealing temperature, as shown in Figure

2-12 [64]. During annealing at the low temperature range, which allows precipitation taking place before recrystallization, an elongated recrystallized grain structure has been obtained since newly-formed precipitates show a preferred distribution along the subgrain boundaries that aligns along the rolling direction. When annealed at the higher temperature, the kinetics of recrystallization is higher than that of the precipitation, and the corresponding recrystallized nuclei grow isotropically without the pinning effect from the concurrently-formed precipitates. This effect of concurrent precipitation on elongated recrystallized grains can also be overcome by heat treatments before cold rolling. Studies have shown that by an aging treatment in which free solutes precipitate before cold work and annealing, equiaxied recrystallized grains were obtained [58,138].

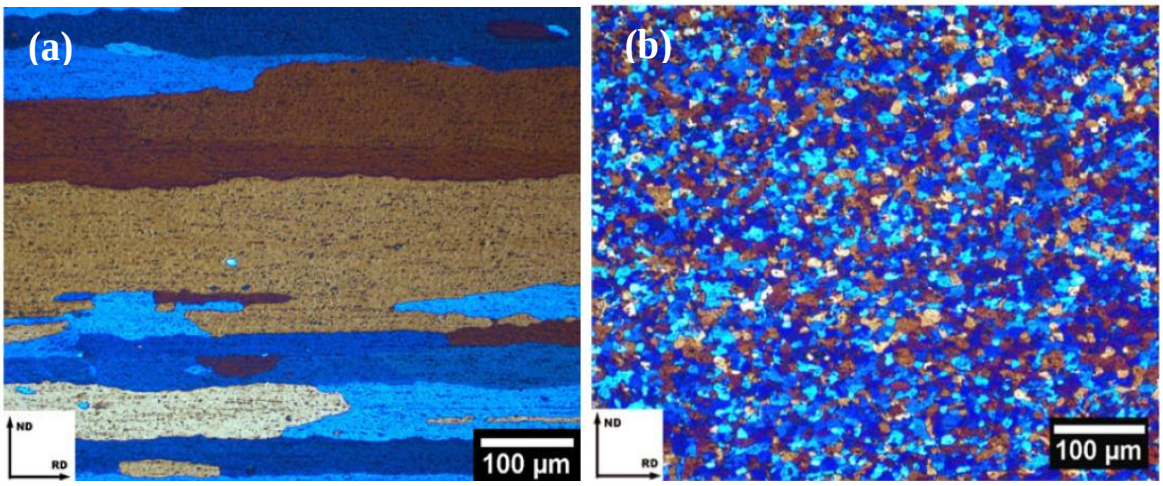


Figure 2-12. Recrystallized grain structure of a cold rolled AA3013 at (a) a temperature lower than *Tc* and (b) a temperature higher than *Tc* [64].

To conclude, precipitates formed during annealing preferentially locate at high angle boundaries in the rolling direction, which leads to an elongated grain structure. By aging treatment before cold-rolling, the pre-existing precipitates usually present a more uniform distribution than those formed after cold work and during annealing. As a result, a uniform Zener drag pressure allows recrystallized grains to grow isotropically.

### 2.3.5 **Recrystallization of AA6xxx alloys**

The annealing behavior of AA 6xxx alloys has been studied experimentally and numerically for the recrystallized microstructure and texture. Several studies have demonstrated that the complex precipitation in the Al-Mg-Si-(Cu) system plays a significant role in the recrystallized microstructure and mechanical properties [58,83,85,86,139–142].

Due to the high stacking fault energy of Al alloys, large well-defined cell structures are expected to form during deformation, which facilitate the formation of new recrystallization grains [52,143]. However, small precipitates existing before cold-rolling in AA6xxx system hinder the formation of cell structure of dislocations, and give rise to a less clearly defined cell structure [85]. For AA6xxx alloys, different precipitates include β″, β′, Q′, and Q″ et al. formed at low temperature range have a fine dispersion and various shapes. These fine precipitates can also obstruct the movement of dislocations and inhibit the motion of grain boundaries during the recrystallization process. Lillywhite and coworkers have observed that boundary migration of the recrystallization front was controlled by the transformation from a metastable phase into a stable phase or particle coarsening during annealing [87]. The effect

of the pre-existing different dispersions of precipitates on the recovery process, recrystallized microstructure and related texture has been intensively studied [85,140,141,144]. However, there is little information on the effect of precipitates formed during industrial thermal cycles or formed during annealing, which greatly influence the final microstructure and properties of sheet products.

PSN is found to be an effective nucleation mechanism in AA6xxx alloys. Lillywhite and coworkers have shown evidence of nucleation from large particles for a cold rolled Al-Mg-Si alloy [87]. Recrystallized grains are also found to nucleate at the large Fe-based constituent phases for AA6111 during annealing [84]. Significant effort has been made to obtain fine grain size in order to take advantage of PSN, however, traditional thermal-mechanical processing by means of overaging, cold rolling and final annealing does not always lead to a refinement of grains through PSN [145]. It is then concluded that the distribution of particles has a decisive effect on the efficiency of PSN, and it also concluded that not all of large particles can be nucleation sites. However, large particles near grain boundaries and deformation bands are often found more capable to be nucleation sites [130]. Another reported operative nucleation mechanism in AA6xxx is SIBM. Yamamoto and coworkers [82] have investigated the annealing behavior of a cold rolled Al-Mg-Si with 30% thickness reduction using in-situ TEM. They have observed the nucleation mechanism of multiple subgrains SIMB with the feature showing a migrating boundary dragged by small angle boundaries behind a 30% cold rolled Al-Mg-Si alloy annealed at 400$^{o}$C [82]. However, the

SIMB nucleation mechanism was not found in the same material with a 50% thickness reduction.

The influence of different alloying elements on recrystallization has also been established for AA6xxx. Transition elements such as Fe and Mn can form large particles, and these particles tend to weaken the recrystallization texture and to refine the final grain size by providing nucleation sites [144]. Due to the presence of a certain volume fraction of precipitates, a weak texture is usually found in AA6xxx alloys [146].

### 2.3.6 **Recrystallization of AA3xxx alloys**

The recrystallization of homogenized AA3xxx alloys and the competition between recrystallization and precipitation of Mn-containing phases in these alloys have been attentively investigated [57,60–65,70,77–80,118,137,138,147–157]. The recrystallization behavior of AA3xxx is affected strongly by Mn in solid solution and the precipitation kinetics of Mn-containing phases at annealing temperatures [64,65,77,80,118,138,149,151]. It has been reported that the precipitation of Al-Mn phases dominates the annealing process in a low temperature range, whereas recrystallization starts earlier than precipitation in a high temperature range [60,138]. However, the selection of the annealing temperature range is dependent on the level of deformation and free Mn solute [80,157].

The annealing condition where both precipitation and recrystallization occur has also been studied [61,64,65,80,153,157]. It's well-known that if precipitation takes place prior to recrystallization or concurrently with recrystallization during annealing, the recrystallized

microstructure with elongated grains and distinguished texture characteristics might develop [57,64,153]. Tangen and coworkers' study [64] has shown that the recrystallized grains are elongated due to the precipitate formation along the boundaries aligning in the rolling direction. It has been concluded that a coarse grain structure with a dominant P component and a relatively strong rotated cube texture is generated at temperatures where precipitation takes place before recrystallization. On the other hand, a fine equiaxied recrystallized grain structure with a weak P texture is obtained when precipitates are present prior to the cold rolling [64].

Nucleation mechanisms in AA3xxx alloys including particle stimulated nucleation (PSN) from large particles and stress induced boundary movement (SIBM) from grain boundaries have also been evaluated [61,63,137,138,150,155,158]. Furrer and Hausch have studied the recrystallization behavior of an Al-1 wt.% Mn alloy fabricated from an industrial process line, and provided evidence of PSN near large constituent particles [150]. The study has also shown that PSN mechanism was facilitated by the existence of precipitate free zone around the large particles [150]. This PSN mechanism has been later supported by other studies [63,155]. In addition, SIBM has been found to occur in a high purity 90% cold rolled Al-1.3 wt.% Mn alloy during annealing at temperatures between 648 and 773 K [61] and an 80% cold rolled Al-1.3 wt.% Mn alloy annealed at 661 and 673 K [158]. Somerday and Humphreys [61] have shown a large number of low angle boundaries behind the broad recrystallization front, and related the occurrence of this mechanism to the effect of temperature on the driving pressure for recrystallization and precipitation. In the case of the

80% cold rolled pure Al-Mn alloy, Ping et al. [158] have suggested the large initial grain size, Mn in solution and low annealing temperature favor this nucleation mechanism. SIBM has also been found to be an operative nucleation mechanism for deformed pure Al, and certain other alloys (see section 2.3.2 for more details) [55,126,131,132,136].

# Chapter 3 General Methodology

The materials used in this work and related processing information are first introduced in detail. This is followed by the heat treatments, microstructure characterization, and related experimental techniques employed in this work.

## 3.1 Material

The laminated bi-layer AA3003-X609 material was provided by the Novelis Global Technology Center in the form of a 5 mm thick hot rolled plate and a 2 mm thick cold rolled sheet, with AA3003 and X609 alloys as the clad and core layers, respectively. The nominal chemical compositions of the AA3003 and X609 layers are given in Table 3-1.

Table 3-1. Nominal chemical composition of the alloy layers in wt. %.

| Component | Si | Cu | Mg | Mn | Fe |
|---|---|---|---|---|---|
| X609 (Core) | 1.14 | 0.45 | 0.52 | 0.15 | 0.23 |
| AA3003 (Clad) | 0.22 | - | - | 1.07 | 0.57 |

Cold rolling was applied to the 2 mm cold rolled sheet in order to obtain 1 mm thick sheets with an 80% reduction.

## 3.2 Heat treatment

The as-received 5 mm hot rolled laminated plate was employed for the studying of precipitation hardening. Aging heat treatments were conducted at different temperatures

between 160°C and 210°C, immediately after solutionizing at 560°C for 1 h in an air furnace and water quenching. Aging times and temperatures are listed in Table 3-2. Samples for aging times shorter than 1 h were solutionized in a salt bath, water quenched and then aged in an oil bath. This aging treatment was conducted at Novelis Research & Technology Center.

Table 3-2**.** The studied precipitation conditions.

| Temperature (°C) | Time | Atmosphere for heat treatment |
|---|---|---|
| 160 | 1-6 h | air |
| 180 | 1-4 h | air |
| 200 | 1-3 h | air |
| 210 | 0-1 h | oil bath |

Isothermal annealing treatments were conducted on the 2 mm thick and 1 mm thick cold-rolled sheets at temperatures below the solutionizing temperature of the core alloy (i.e. 540°C), and the solutionizing temperature [90]. The annealing conditions are listed in Table 3-3. All samples were water quenched at the end of the annealing treatment.

Table 3-3**.** The studied annealing conditions.

| Sheet thickness | Sheet designation | Temperature ($^{o}$C) | Time | Atmosphere for heat treatment |
|---|---|---|---|---|
| 2 mm | 60% CR sheet | 380 | 1 h | air |
| | | 420 | 1 h | air |
| | | 480 | 1 h | air |
| | | 540 | 30 s | salt bath |
| | | 540 | 60 s | salt bath |
| 1 mm | 80% CR sheet | 380 | 1 h | air |
| | | 420 | 1 h | air |
| | | 540 | 30 s | salt bath |
| | | 540 | 60 s | salt bath |
| | | 300 | 1-24 h | air |

## 3.3 Microstructure characterization

In the following section, the characterization methods are explained in detail. All characterization was conducted on the longitudinal surface of the sheet material, which is defined as the plane formed along the rolling direction (RD) and normal direction (ND).

### 3.3.1 Microhardness measurement

Vickers microhardness tests were carried out with an MHTA series 200 hardness tester, and a load of 200 g. Each reported hardness value was the average of 5 separate indentation measurements. Standard deviation was calculated for error bars assuming a normal distribution. The locations used for measuring the hardness of the clad and core layers were the centers of the respective layers, as shown schematically in black in Figure 3-1.

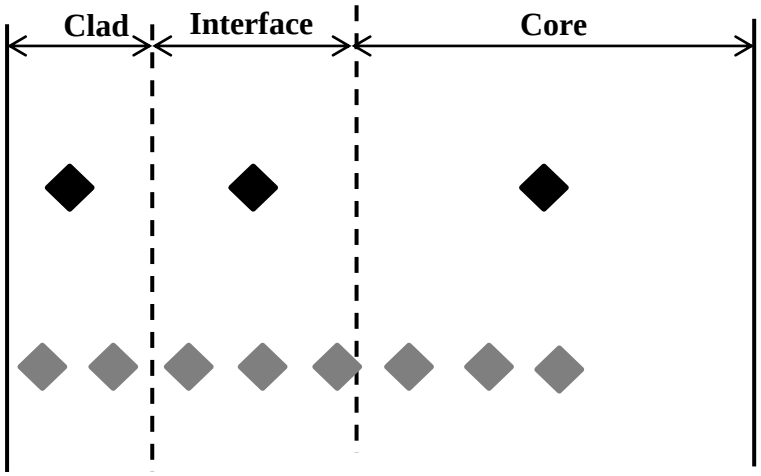


Figure 3-1. Schematic showing the positions for hardness measurement (black indentation marks representative hardness for three layers' grey indentation marks: hardness profile along the distance).

A hardness profile along the ND of the material was obtained by moving the sample stage incrementally in the direction perpendicular to the edge of the clad surface, as indicated in grey in Figure 3-1. The distance between two neighboring indentations was kept to be greater than 2.5 times the diameter of the indentations, in order to avoid potential strain hardening effects.

### 3.3.2 **Calorimetry measurement**

A SETARAM C 80 Calorimeter was used for isothermal calorimetry (IC) and differential scanning calorimetry (DSC) experiments. During testing of samples, the reference vessel was kept empty. For each experiment, a high purity Al sample, with a mass similar to that of the alloy samples, was tested to obtain the reference heat flow trace. The final trace was obtained by subtracting the trace for the pure Al sample from that of the sample. Multiple tests were conducted for each reported test condition to ensure repeatability.

IC tests were conducted at 160°C, 180°C, 200°C, and 210°C. The IC samples were cut along the transverse direction (TD) to an approximate dimension of $5 \times 7 \times 7$ $mm^3$, and a mass of 0.6 g. The tests were conducted with the introduction of the sample into the test vessel after the calorimeter was stabilized for 1 hour at the test temperature.

DSC tests were conducted at the temperature range of 25 to 300$^{o}$C with a heating rate of 0.5°C /min. DSC samples were in similar shape as IC samples but have an approximate mass of 0.4 g. The samples were introduced to the test vessel before heating starts.

### 3.3.3 **Optical microscopy**

Metallurgical samples were prepared by first grinding with SiC paper from 600 grit up to 1200 grit, using water for lubricant and cooling. The samples were then polished with successively finer diamond abrasives of 1 and 0.25 μm, respectively. A suspension of colloidal silica (approximately 0.06 μm particle size) was used for the final polishing step. Keller's solution (190 ml distilled water, 5 ml nitric acid, 3 ml hydrochloric acid, 2 ml hydrofluoric acid) was employed for etching, and it was performed by immersing the samples in the etchant for about 2 mins.

### 3.3.4 **Electron probe micro-analysis (EPMA)**

EPMA was conducted to obtain the compositional profile across the cross section of the solutionized material in ND. The tests were conducted on two samples, and 2 lines across the cross section were tested on each sample to ensure repeatability. A fully-automated CAMECA SX-50 instrument was used in wavelength-dispersion mode with the excitation voltage of 15 kV and beam current of 20 nA. The peak count time is 10 seconds every 5 seconds in a spot diameter of 1 μm. These conditions resulted in an interaction volume approximately 3 μm in diameter. Although the measurement locations were set to not be on visible (400×) particles, the presence of finely-dispersed solute-rich particles within the interaction volume was generally unavoidable. The lack of a smooth variation across the

cross section for some compositional profiles is attributed to the effects of these particles. More information on EPMA tests can be found in the ref. [90]. EPMA tests were conducted at the University of British Columbia by Drs. Mati Raudsepp and Edith Czech.

### 3.3.5 **Scanning electron microscopy (SEM)**

SEM was conducted using a LEO FESEM-1530 microscope operating at 10 kV in backscattered mode. The samples for SEM were prepared by mechanical grinding and mechanical polishing, as well as electro-polishing. Electro-polishing was performed at -30$^{o}$C and 9 V for approximately 1 min in a solution of 30 vol.% nitric acid and 70 vol.% methanol. Qualitative composition data on the phases was obtained by Energy Dispersive Spectroscopy (EDS).

### 3.3.6 **Transmission electron microscopy (TEM)**

TEM analyses were performed using a PHILIPS CM-12 microscope operating at 120 kV. There were two types of TEM foils prepared from aged and as-deformed conditions, respectively. For aged condition, TEM foils were obtained from both the interface region and the core layer. However, TEM foil was only prepared for the core layer. The TEM samples for the interface region and core layers were obtained from the approximately 0.3 mm from the clad and the middle of the core layer, respectively, as given in Figure 3-2

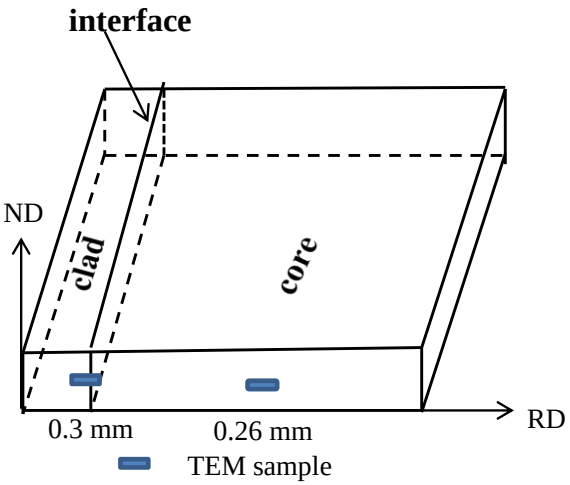


Figure 3-2. Schematic presentation of the locations for TEM samples.

TEM foil for the interface region was prepared by focused ion beam (FIB) milling. The FIB-cut specimen, shown by a circle in Figure 3-3 (a), was obtained from the clad surface. The specimen was then removed along the transverse direction (TD) as shown in Figure 3-3 (b). The FIB milling was done at Canadian Center for Electron Microscopy by Julie Huang.

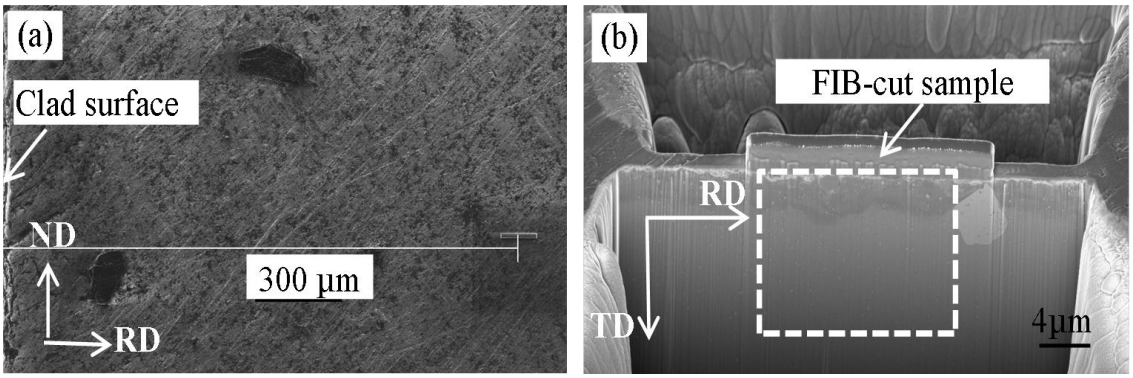


Figure 3-3. Information for obtaining the FIB-cut specimen for (a) specimen along RD and (b) Magnified view of the specimen.

The TEM foils for the core layer for the 5 mm plate were prepared by mechanical grinding of the plate sample to an approximate thickness of 70~90 μm. Discs with a diameter of 3 mm were punched from the foil following grinding, which were then twin-jet electro-polished to perforation with a solution of 30% nitric acid and 70% methanol at -35°C and 35 V. The preparation was done by Xiang Wang at McMaster University.

TEM foils of the core layer for the 2 mm sheet were prepared in the same manner as for the 5 mm plate. Due to a smaller size in the RD for the 2 mm sheet than the 3 mm diameter of the standard TEM discs, the discs could not be punched to form a full circle. However, a same twin-jet electro-polishing was employed, and details on obtaining the discs are given in Figure 3-4. The electro-polishing was prepared by Wenhe Gong at Canadian Center for Electron Microscopy.

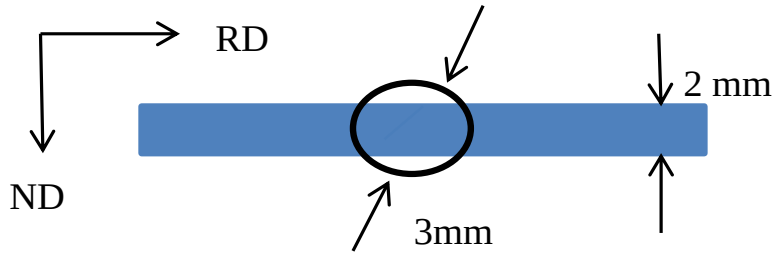


Figure 3-4. The obtaining method of TEM samples from the 2 mm cold rolled foil.

### 3.3.7 **Electron backscatter diffraction (EBSD)**

EBSD was performed by Haiou Jin using a Philips XL30S field emission gun SEM, equipped with a Nordlys II detector, operating at 25 kV. Samples for EBSD were

mechanically ground, and then polished using a vibratory polisher for 8 hours with 0.05 μm colloidal silica. The polished samples were finally etched with 0.5% HF for 10 seconds. A step size of 1 μm was employed for scanning an area of 563 μm × 422 μm. The grain structure analysis was performed with HKL Channel 5 software. Because of the limitations of the angular accuracy of the EBSD technique, misorientations of less than $2.5^{o}$ were excluded from the EBSD results. Grain and subgrain boundaries with misorientation between $2.5^{o}$ and $15^{o}$ are defined as low angle boundaries. High angle boundaries are denoted to boundaries with misorientation greater than $15^{o}$.

# Chapter 4 Precipitation behavior of the AA3xxx-X609 laminated system

This chapter reports on the precipitation behavior of the laminated material through both experiments and modeling. The characterization of precipitates and the study of precipitation hardening are conducted using TEM and hardness measurements. A model is built to predict the precipitation hardening at different aging conditions.

## 4.1 Introduction

AA6xxx alloys can be significantly age-hardened, and the precipitation behavior of the monolithic alloys has been extensively studied [21,24,27–29,32,33,101]. In the current laminated material, the precipitation behavior of the core layer of AA6xxx is expected to be similar to the monolithic material. However, during co-casting and subsequent thermal-mechanical processing, an interface region containing a dynamic compositional gradient is reported to exist in the laminated system [14,90]. It is well known that the precipitation behavior strongly depends on the material composition, including the solute content and the ratio of solutes forming the precipitates [26,106]. The existence of the compositional gradient may therefore play a significant role in the precipitation behavior of the laminated sheet, but there have not been any previous investigations conducted on laminated systems involving AA6xxx alloys containing such a gradient. This work is the first report focused on providing basic understanding of the precipitation hardening behavior of a heat-treatable Al alloy co-cast with a non-heat treatable Al alloy. The compositional gradient across the laminate, and

its change with solution heat treatment processes, may affect the precipitation hardening behavior and result in location-dependent characteristics. A modeling approach developed for monolithic AA6xxx alloys [41] is utilized in order to evaluate the precipitation kinetics of the bulk system and the yield strength of the core material.

## 4.2 Experimental methodology

Isothermal aging was conducted on the 5 mm hot rolled laminated plate for different aging conditions. Aging treatment, hardness measurement, IC and DSC are detailed in section 3.2 and section 3.3. The method of analyzing IC and DSC data is referred to ref. [41]. TEM on precipitation distribution is done following the procedures given in section 3.3.

## 4.3 Results

### 4.3.1 The as-received condition

As seen from the SEM micrograph of the cross-sectional area of the as-received sample shown in Figure 4-1, the clad region contains a larger population of coarse particles, while the particles becomes much finer towards the core area. EDX analysis verified that the large particles in both the clad and core layers, resolvable in Figure 4-1 (a), are particles containing Mn, Fe or Si as shown in Figure 4-1 (b) and (c). Thermodynamic analysis using the FactSage 6.3 software package and the FTlite database [159] was previously used to predict the type and stability temperature ranges for the dispersed secondary phases, considering both the core and clad alloy compositions [90]. Those results have shown that the secondary phases are AlFeMnSi, $Al_3FeSi$, $Al_2Cu$, $Mg_2Si$, and Si for the core alloy, and $Al_6$(Mn,Fe) and

AlFeMnSi phases for the clad [90]. It is therefore concluded that the large particles formed at a high temperature in the laminated material, and resolvable in Figure 4-1, are possibly constituent particles containing Fe, Mn or Si.

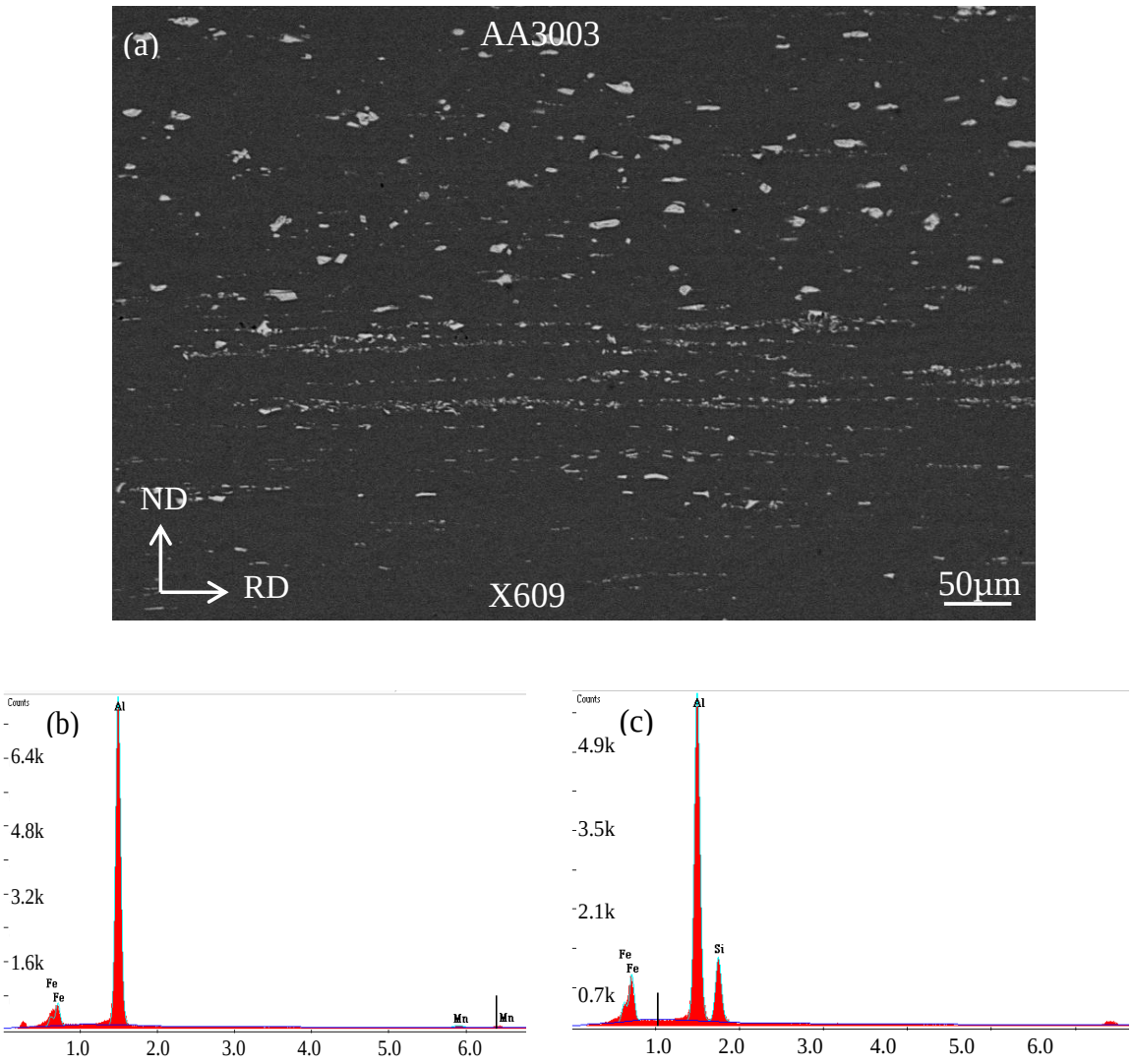


Figure 4-1. (a) Particle distribution along the cross section of the as-received 5 mm thick plate, EDX spectra for large particles in (b) the clad layer and (c) the core layer.

The hardness profile across the cross section of the hot rolled laminated system given in Figure 4-2, and displays a generally increasing trend from the clad surface towards the interface. The highest value is 75 HV, located between 260 μm and 300 μm from the clad surface, and followed by a stable value of around 70 HV into the core layer.

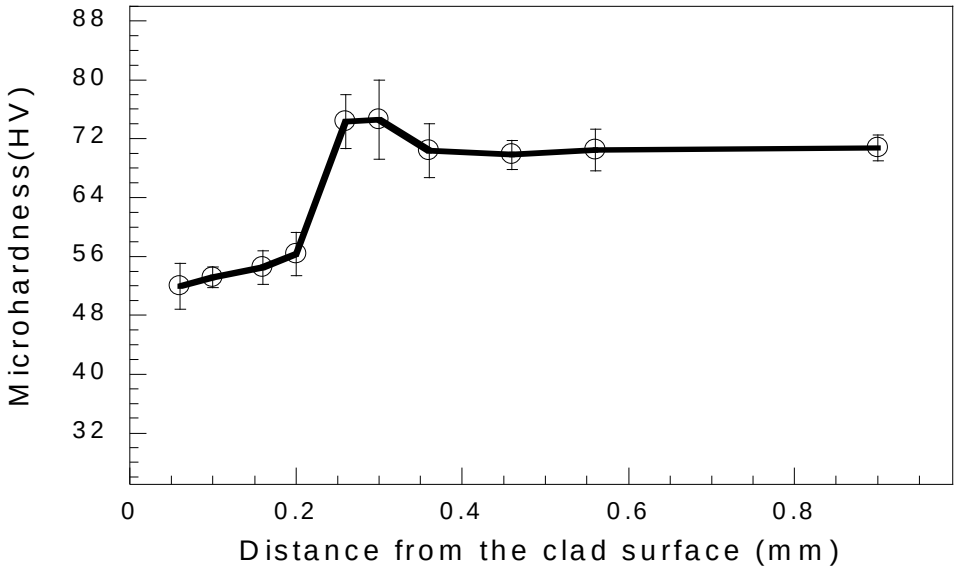


Figure 4-2. The hardness profile along the cross section of the as-received 5 mm thick plate.

The through-thickness distribution of solutes has been studies by Foroozmehr et al. [90] and given in Figure 4-3. A composition gradient of Mg, Si, Cu and Mn is found at the interface region between the clad layer and core layer, and the interface region was defined to start from approximately 0.35 mm to 0.5 mm.

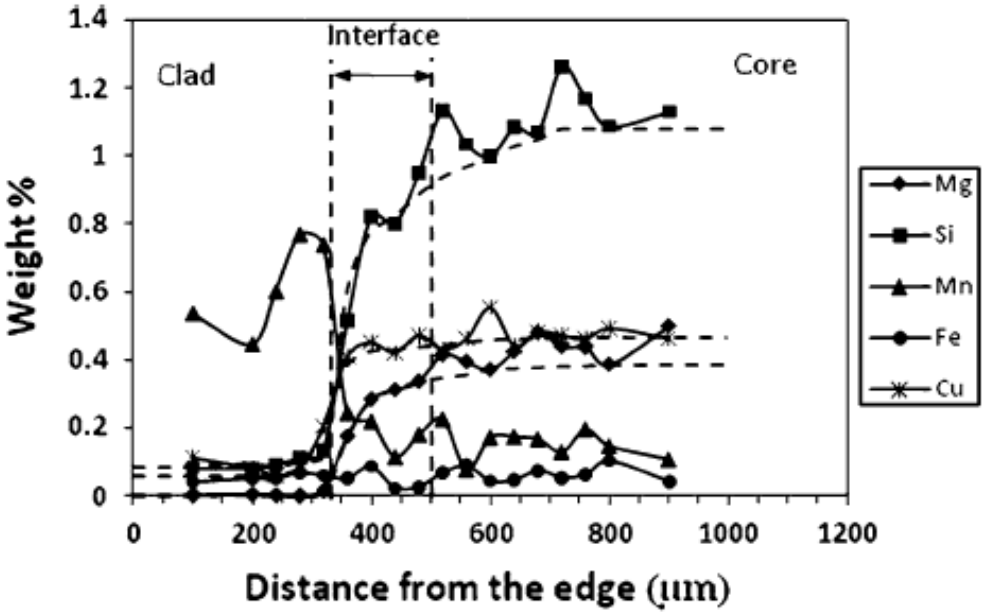


Figure 4-3. Through-thickness EMPA profile of the as-received 5 mm thick plate [90].

### 4.3.2 **The as-quenched condition**

After solutionizing at 560$^{o}$C for 1 h, large constituent particles are still found to be stable at that temperature, and are observed in the as-quenched condition, shown in Figure 4-4. However, small precipitates of $Al_2Cu$, $Mg_2Si$, and Si phases are expected to dissolve completely within 1 h at that temperature, based on a related EMPA study [90]. The dissolution of fine secondary phases during solutionizing thus leads to an enrichment of free solutes for Mg, Si and Cu in the as-quenched matrix.

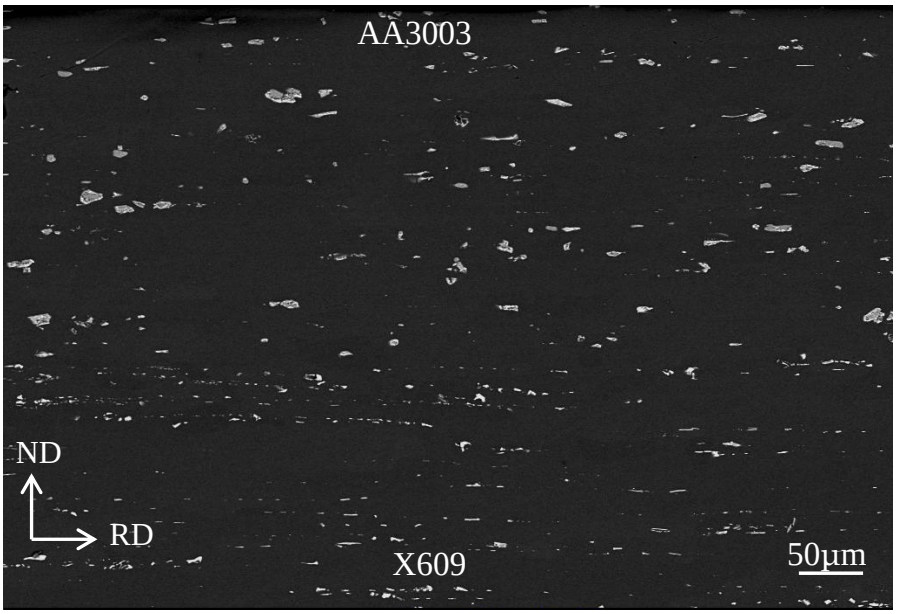


Figure 4-4. Particle distribution along the cross section of the as-quenched 5 mm thick plate.

The corresponding hardness profile along the cross section after the solutionizing is given in Figure 4-5. Compared to the as-received condition (Figure 4-2), it is clear that solutionizing decreases the hardness significantly for all the layers. The profile also shows that the hardness of the interface region still increases with the distance from the clad surface towards the core layer. The hardness of the clad and core layers are about 32 HV and 53 HV, respectively. Comparison between Figure 4-2 and Figure 4-5 also suggests that the highest hardness value for the hot rolled condition at the interface region disappears after the solutionizing treatment.

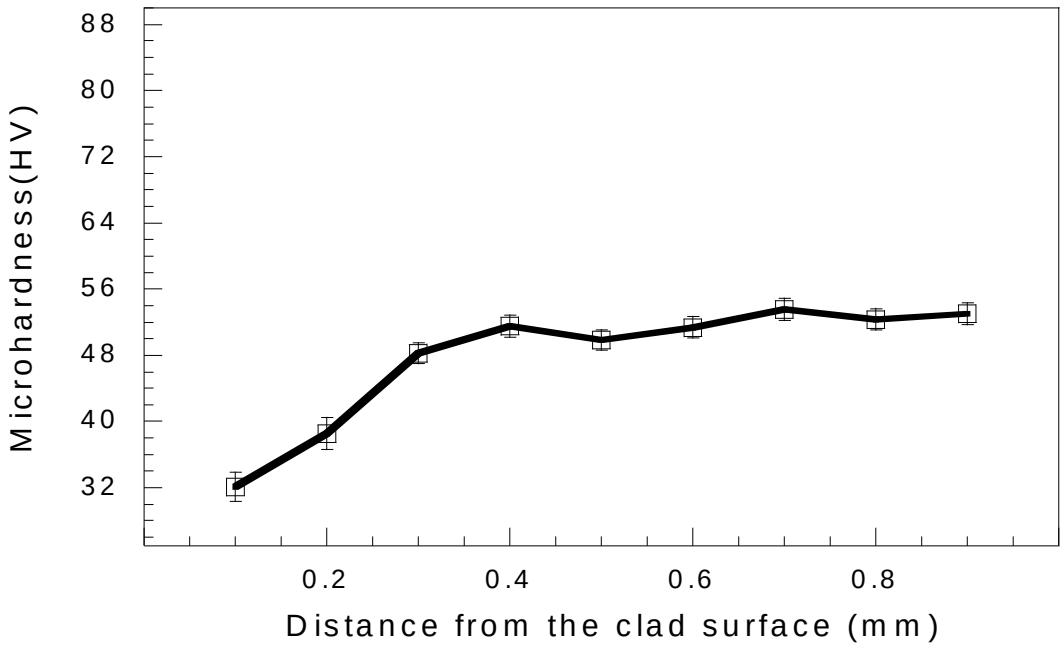


Figure 4-5. Hardness distribution along the cross-section of the quenched 5 mm thick plate.

The EMPA profile of the solutionizing and quenched condition was measured and given in Figure 4-6. During solutionizing at 560$^{o}$C, the interface becomes enriched in the content of Mg, Si, and Cu due to dissolution of precipitates, and the diffusion of Mg, Si, and Cu towards the clad side. In this way, the interface grows into a wider layer, located approximately between 0.2 mm (the distance where content of Mg, Si and Cu starts to show a higher content than that at the core layer) and 0.6 mm (where the content of Mg, Si and Cu is close to the average of the core layer) from the clad surface, as shown in Figure 4-6. There is no apparent change in the content of either Mn or Fe as shown in Figure 4-6, since particles containing Mn and Fe are stable at the solutionizing temperature. It should be noted that the uneven trend of the compositional profiles, which is particularly prevalent for the as-received

material's profiles, is due to the presence of large second phase particles containing that particular element within the interaction volume of the electron beam during EPMA.

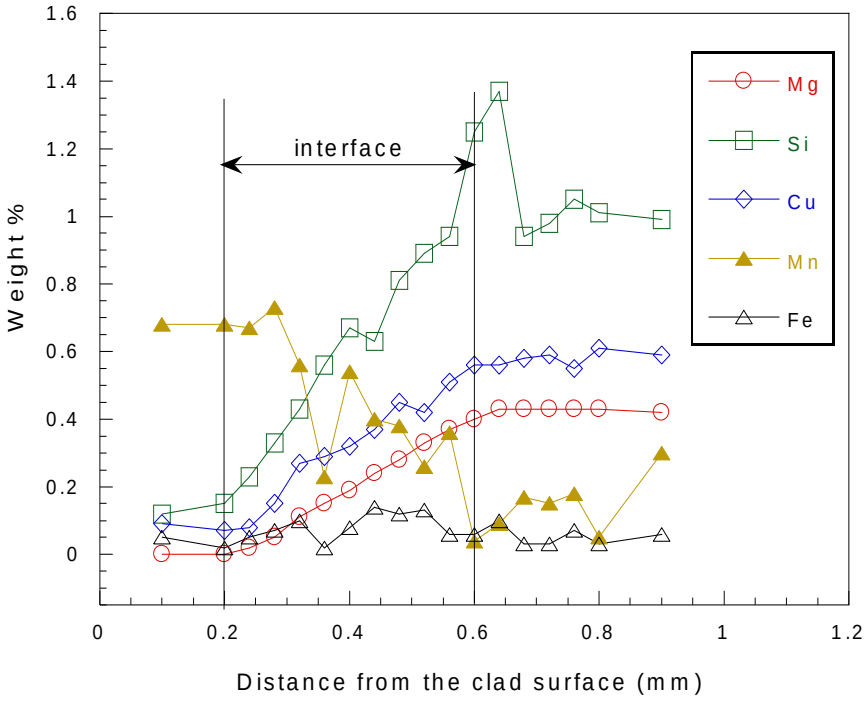


Figure 4-6. Definition of the interface region using solute distributions for the solutionized 5mm thick plate.

Based on the particle distribution as shown in Figure 4-4 and EPMA results as shown in Figure 4-6, the interface can be classified into two sections: (i) the section on the clad side (0.2 to 0.3 mm from the clad surface) which demonstrates a dispersion of large constituent particles and contains similar content of Mn as the clad layer; (ii) the section on the core side (0.3 to 0.6 mm from the clad surface) which displays a dispersion of smaller constituent

particles, and contains a lower content of Mn than the clad. Both sections demonstrate an increasing content of Mg, Si, and Cu from the clad surface towards the core layer.

### 4.3.3 **Hardness evolution during aging**

The composition-related hardness dependence for different aging temperatures and times has also been studied, with results presented alongside the hardness for the as-quenched condition in Figure 4-7 and Figure 4-8. The hardness at the interface region gradually is found to increases with time at 180$^{o}$C as shown in Figure 4-7. In addition, the hardness is also found to increase with the distance from the clad surface. The hardness near the clad side shows a steeper gradient than the hardness closer to the core layer. The hardness evolution at 200$^{o}$C, as given in Figure 4-8, displays a similar trend as that at 180$^{o}$C. However, in the first hour of aging, the extent of the precipitation hardening at 200$^{o}$C is greater than at 180$^{o}$C. The precipitation hardening ability of the interface region scales with the solute concentration in the as-quenched condition, as shown in Figure 4-6.

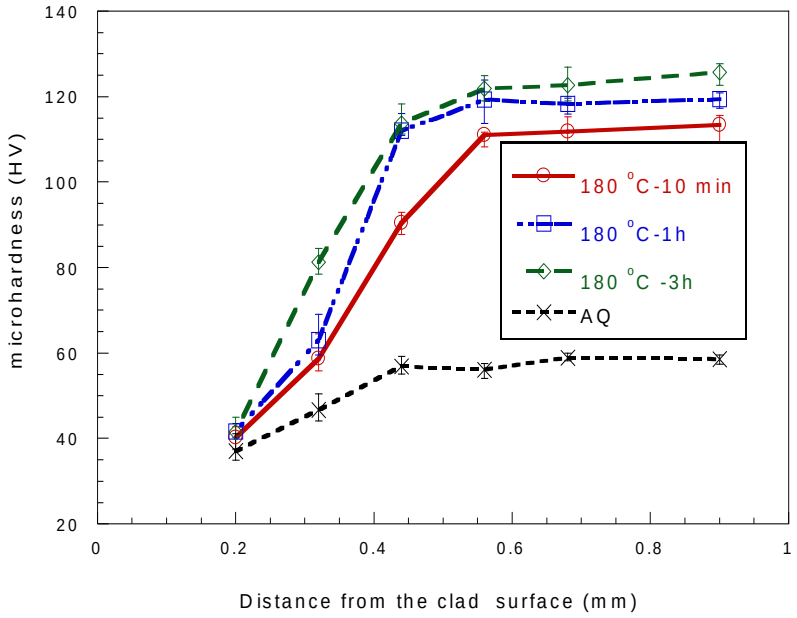


Figure 4-7. The composition-related hardness evolution with aging time at 180°C (AQ designates as-quenched condition).

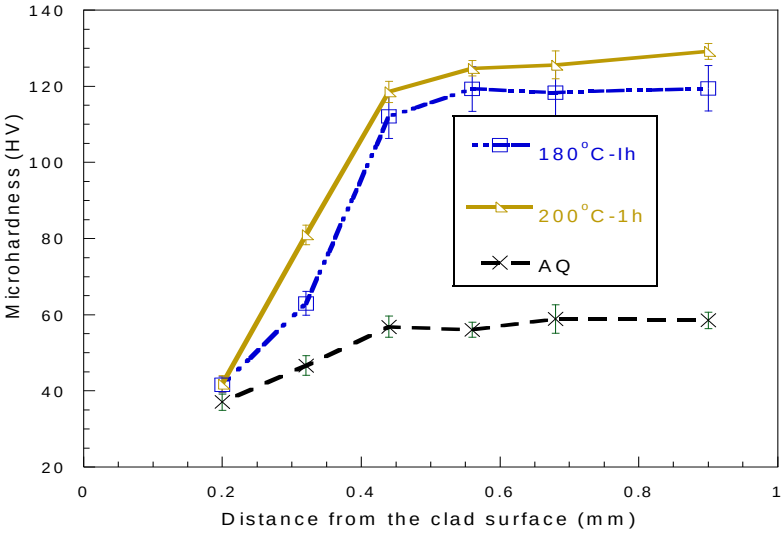


Figure 4-8. Evolution of the hardness profile with aging for different aging temperatures (AQ designates as-quenched condition).

### 4.3.4 **Calorimetry tests**

The heat flow of the laminated AA3003-X609 was measured using a sample from the laminated plate that includes both the clad and core layers. However, the heat flow at the investigated temperature range is mainly attributed to the precipitation reaction in the core layer with little rare effect from the interface between the clad and core layers. The heat flow is then calculated by applying a mass correction. Since the 5 mm-thick laminate plate contains approximately 0.2 mm-thick clad layer, the effective mass correction is applied, and obtained by multiplying the ratio of the mass of the core layer and interface region to the total mass. The ratio is set as 0.96 ((5-0.2)/5), assuming that the densities of AA3xxx and AA6xxx are very close.

IC tests were conducted at various temperatures for solutionized and quenched samples. The results in Figure 4-9 show that a higher peak is observed at a higher aging temperature. Figure 4-9 also suggests that the time to reach the peak of the heat flow is shorter, and the time to reach the end of the peak, $t_f$, is larger at a higher aging temperature. This observation indicates faster precipitation kinetics for a higher aging temperature within the investigated temperature range. The $t_f$ determined using the IC traces are about 6 hrs for 160$^o$C, 3 hrs for 180$^o$C, 2 hrs for 200$^o$C, and 1 h for 210$^o$C. The traces show the typical trends observed in precipitation hardening for AA6xxx alloys [43].

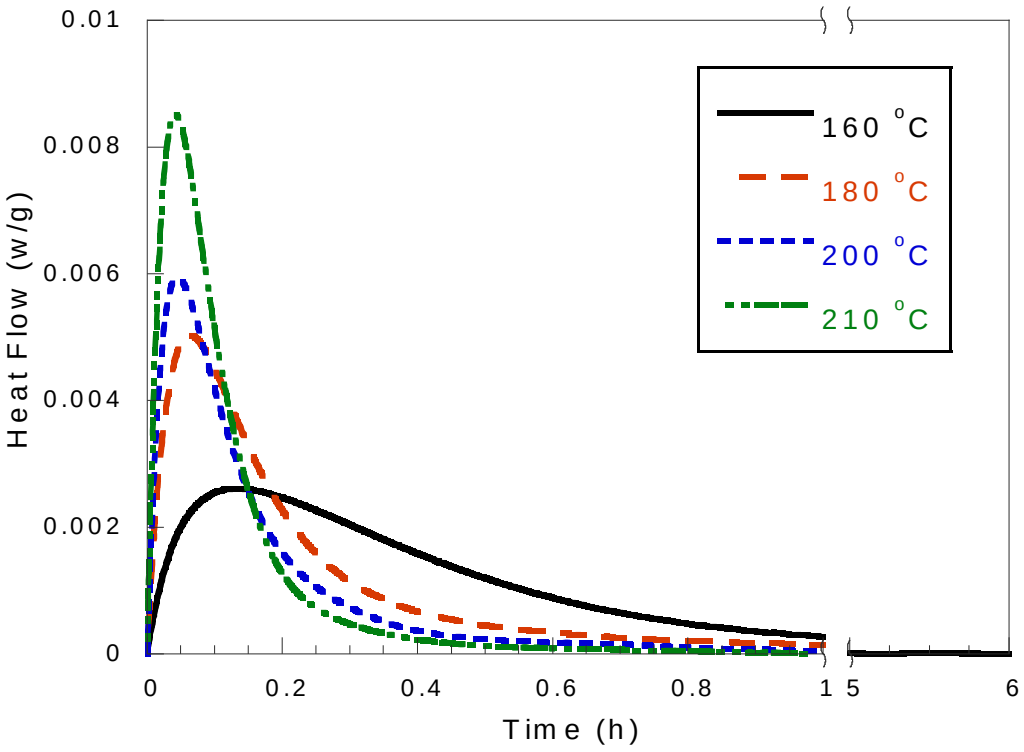


Figure 4-9. IC trace for 5 mm thick plate at various temperatures.

DSC was also employed to investigate the possible precipitation reactions. The results are given in Figure 4-10, with four exothermal peaks, presented as I, II, III, and IV labeled on the DSC trace. The temperatures at which the peaks centered are approximately 50°C, 200°C, 240°C and 270°C, respectively. Those peaks represent the formation of precipitates including GP zones, β″, β′ and Q phase for AA6xxx [101]. The as-quenched laminated sheet with the clad layer removed is also included in Figure 4-10 for comparison. It shows a similar DSC trace to the as-quenched bulk laminated sheet with same peak temperatures, therefore the

four exothermal peaks can be attributed to the interface region and the core layer. Generally, the DSC trace is similar to a typical trace of AA6xxx.

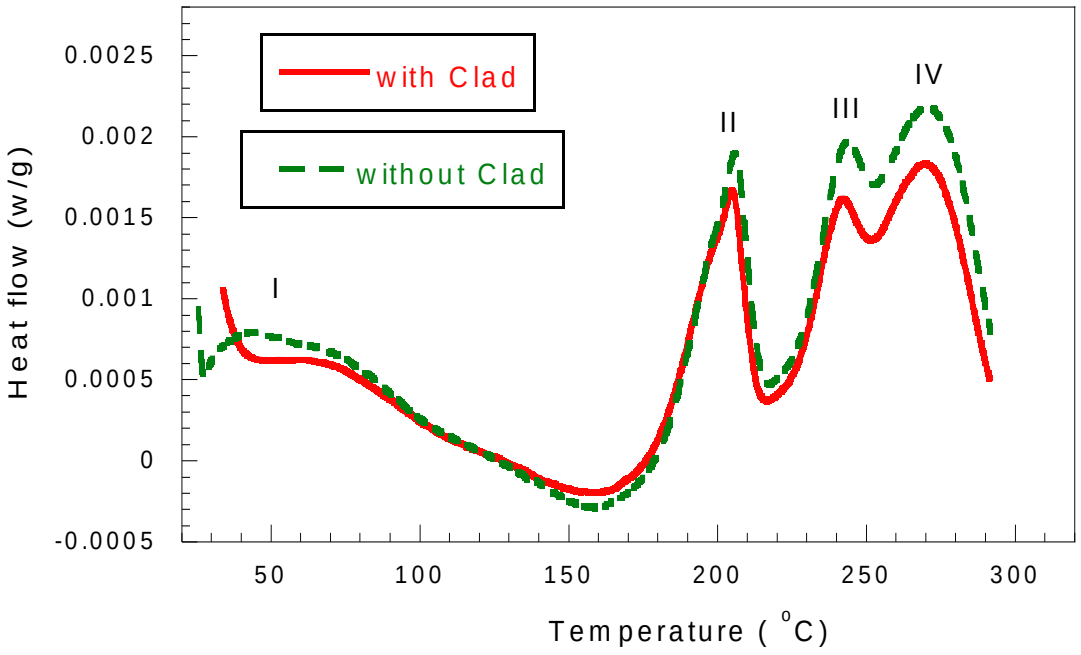


Figure 4-10. DSC traces for the as-quenched 5 mm thick plate with the clad layer and without the clad layer.

### 4.3.5 **TEM characterization**

The precipitate distribution in the core layer and clad-core interface region was examined by TEM for the samples aged at 180°C for 1 h. Figure 4-11 presents the microstructure of the aged core layer observed using $<001>_{Al}$ zone axis. It is clear that a fine distribution of precipitates with a high number density is present in the core layer. The appearance of the

precipitates and the streaks on the selected area diffraction patterns (SADPs) are in agreement with those of β" precipitates [20,101].

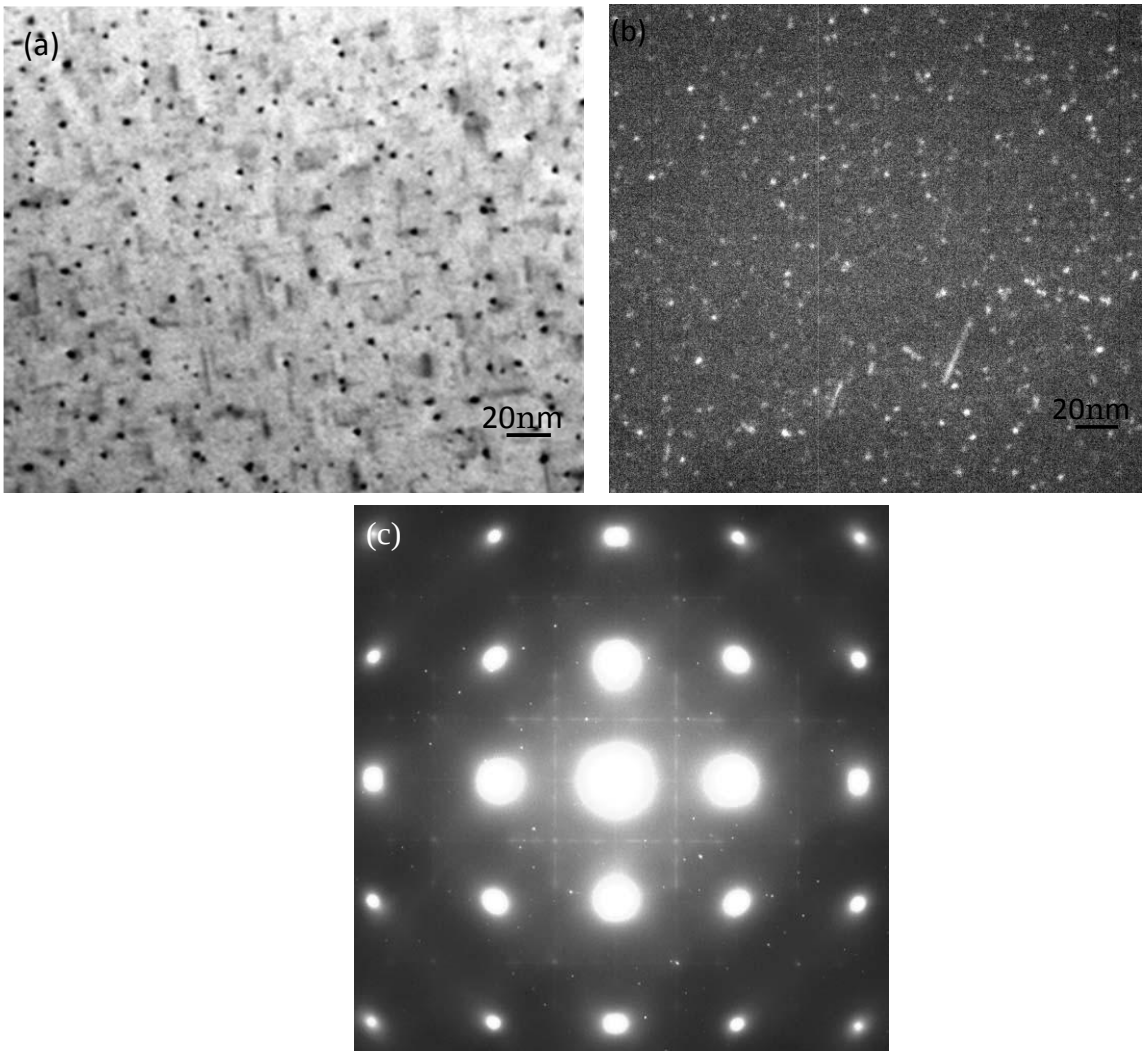


Figure 4-11. TEM micrographs of the microstructure of the core layer along <100> $_{Al}$ zone axis showing β″ precipitates: (a) Bright field images, (b) dark field image, and (c) SADP (TEM conducted by Xiang Wang).

These fine needle-shaped β″ are between 12 and 20 nm in length with a diameter of about 3 nm in the cross section. Matrix strain contrast around the precipitates can also be observed. The core area was also observed using $<011>_{Al}$ zone axis, as shown in Figure 4-12. No obvious diffraction spots from the precipitates can be seen in Figure 4-12 (b) due to the overlap with the matrix spots [160]. Generally, the precipitates in the core layer are distributed very fine and homogeneously.

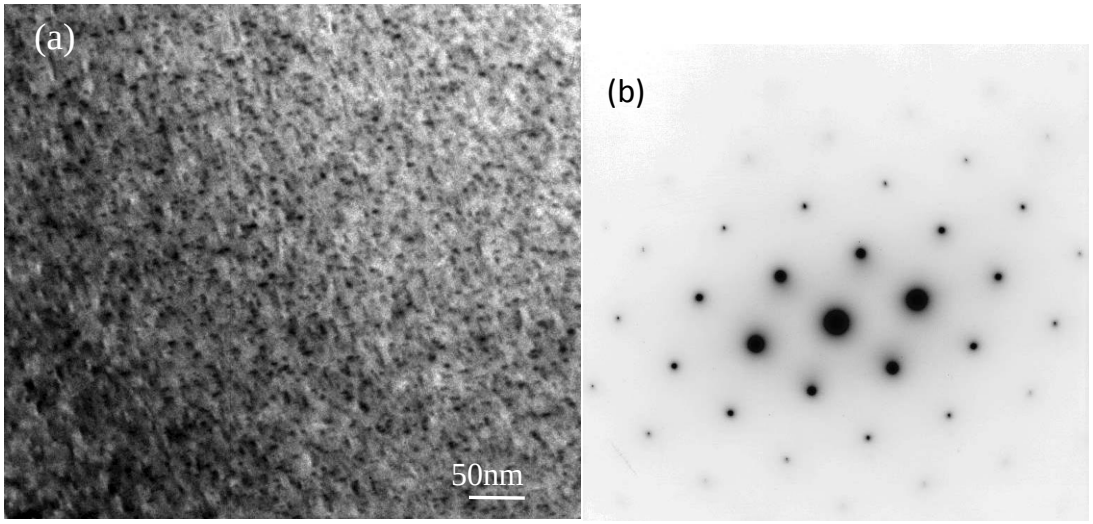


Figure 4-12. TEM micrographs of the microstructure of the core layer along $<011>_{Al}$ zone axis showing β″ precipitates: (a) Bright field image and (b) SADP (TEM conducted by X. Wang).

The distribution of precipitates at the location of 0.3 mm from the clad surface, representative of the interface region, is given in Figure 4-13. It should be noted that due to the very limited thinned area of the FIB-cut sample, only one grain was suitable for observation. The grain, however, could not be tilted to the $<001>_{Al}$ zone axis with a double-tilt stage. The FIB-cut

sample was therefore observed using <011>$_{Al}$ zone axis. Figure 4-13 shows the distribution of very fine precipitates in the interface region. A large fraction of dislocations is also visible. These dislocations might have formed during the FIB cutting process. By qualitatively comparing Figure 4-12 (a) and Figure 4-13 (a) from the same zone axis, it is concluded that precipitates are coarser and in a lower number-density in the interface region than in the core layer.

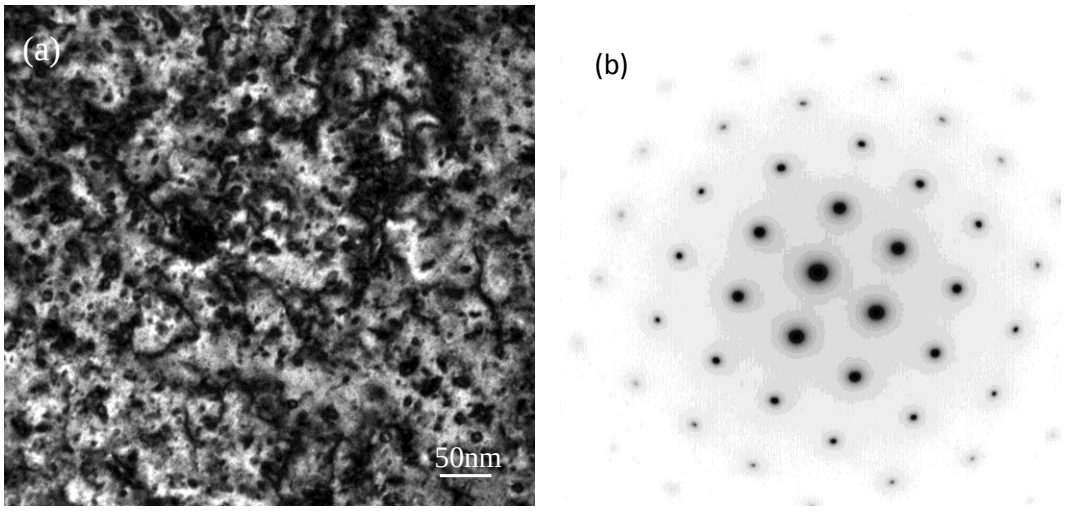


Figure 4-13. (a) Bright field image for interface region and (b) the SADP along <011>$_{Al}$ zone axis (TEM conducted by X. Wang).

### 4.3.6 **Modeling of precipitation hardening**

*JMAK modeling*

The IC traces as shown in Figure 4-9 can be used to obtain the evolution process of the heat flow as a function of time at the aging temperature by calculating the ratio of the instant heat

flow to the total heat flow [41]. Base on the evolution of heat flow with aging time during isothermal aging as given in Figure 4-9, the relative volume fraction $f_r$ can be estimated by dividing the area under the curve for a specific time $t$ by the total area of the whole curve in Figure 4-9. The calculated function $f_r$ with time is given in Figure 4-14. The result suggests that the increase in the relative heat flow with aging time is faster at a higher temperature, which indicates a shorter aging time to reach the unity with a volume fraction of 1 at a higher aging temperature.

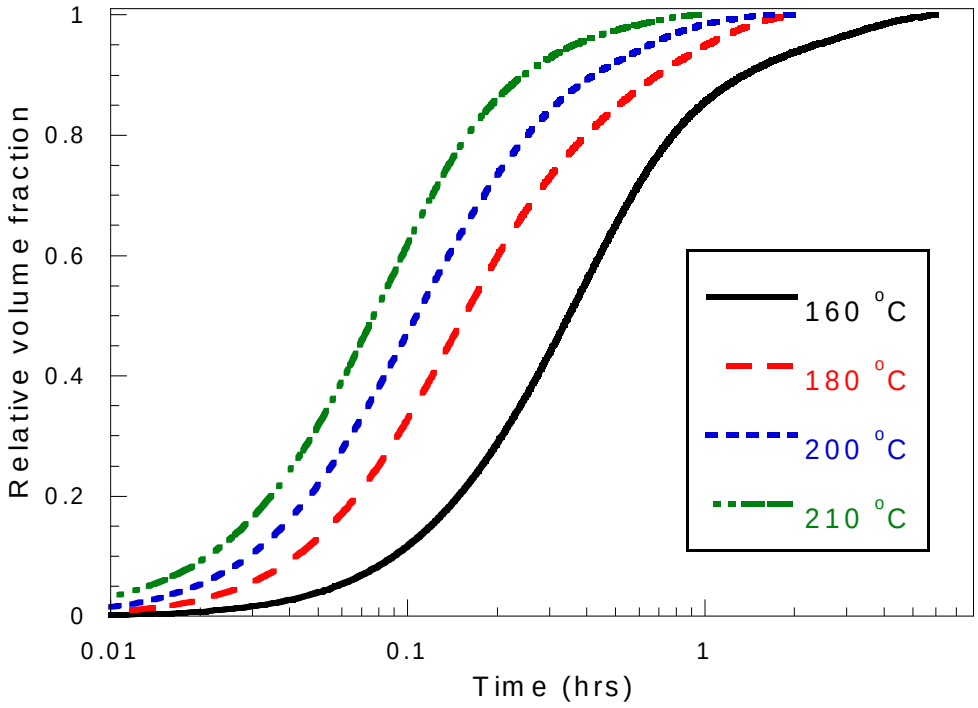


Figure 4-14. The related volume fraction calculated from the IC traces.

Kinetics of precipitation can then be applied to the Johnson-Mehl-Avrami-Kolmogorov (JMAK) model. JMAK formulation is as follows [106]:

$$f_r = 1 - exp(-kt^n) \quad (4\text{-}1)$$

$$k = k_0 exp(-\frac{Q}{RT}) \quad (4\text{-}2)$$

where *t* is time and *k* follows an Arrhenius relationship with temperature *T*. *n* is considered to be independent of temperature. $k_0$ and *Q* is the proportionality constant and apparent activation energy, respectively. In fitting the experimentally-determined values of the relative volume fraction $f_r$ with the JMAK equation, an agreement is found between the experimental result and the model with n close to 1, and varied values of *k* for each temperature. As Figure 4-15 presents, *Q* is estimated to be approximately 48 kJ/mole (± 10 kJ/mole considering the variability of JMAK fits). The calculation method is the same as ref. [41] , and the value of Q is close to the value reported for AA6111 in this reference.

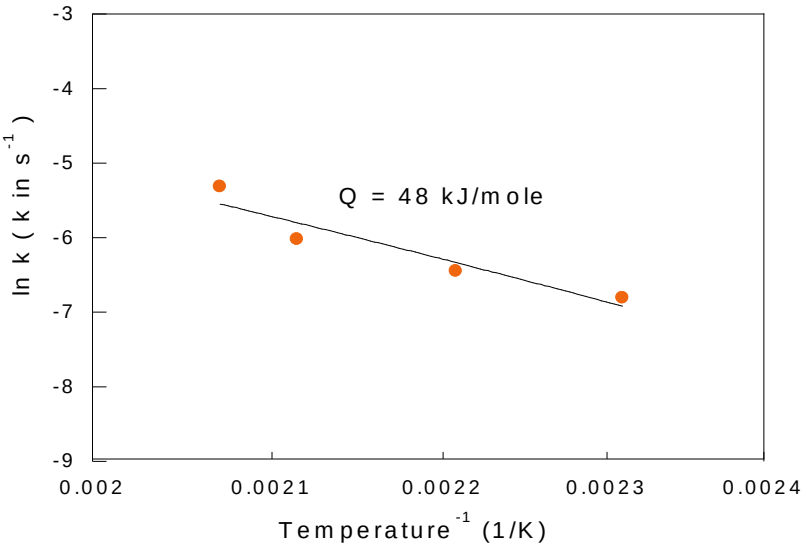


Figure 4-15. Arrhenius relationship of kinetic parameter *k* with temperature

The calculated volume fraction as presented in Figure 4-14 and the JMAK modeled values are compared in Figure 4-16, and the result demonstrates a great match. However, a larger JMAK modeled value is found for the early stage of aging for all the investigated temperatures. There is also a deviation between the calculated and modeled values for the later stage of aging at 160$^{o}$C as shown in Figure 4-14 (a).

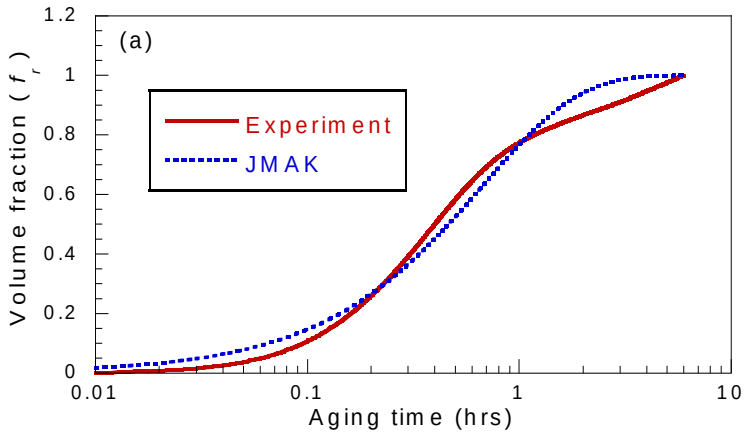


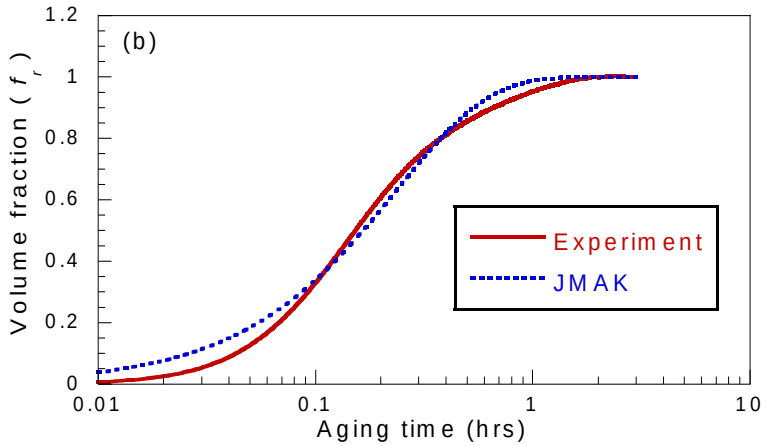

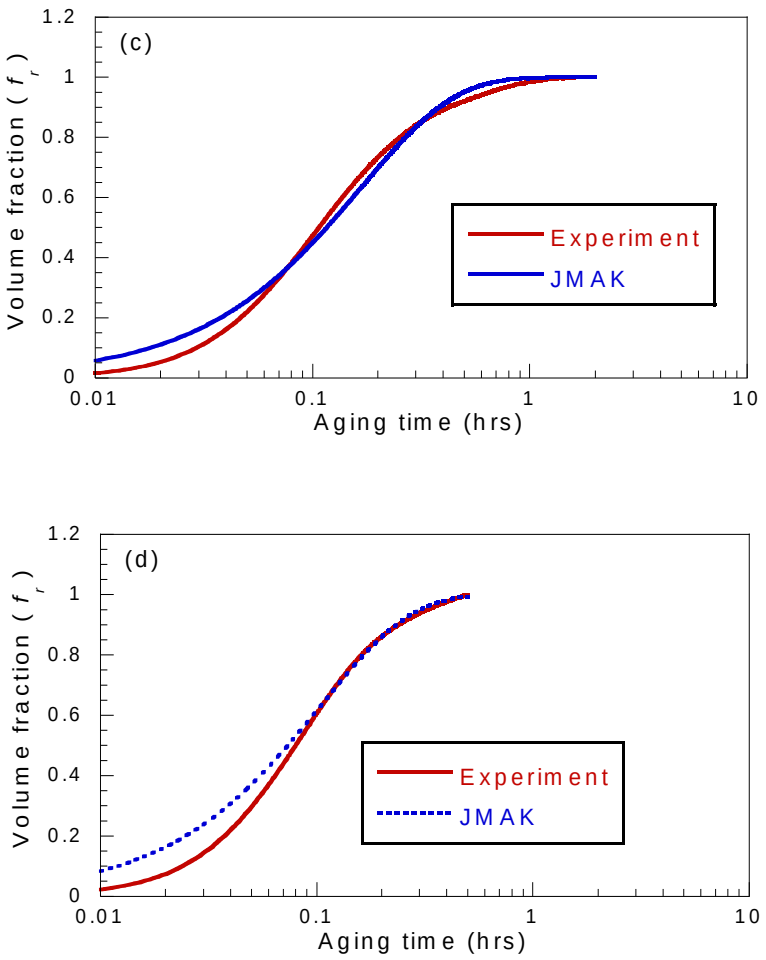


Figure 4-16. Comparison of experimentally calculated and modeled volume fractions of precipitates with aging at (a) 160$^{o}$C, (b) 180 $^{o}$C, (c) 200$^{o}$C and (d) 210$^{o}$C .

*Yield strength modeling*

In order to estimate the yield strength of the aged samples, the hardness values are converted to yield strength according to the following relationship, described by Myhr et al. [42]:

$$HV = 0.33\sigma_y + 16.0 \qquad (4\text{-}3)$$

where *HV* and $\sigma_y$ are the Vicker's hardness and yield strength (MPa), respectively. The estimated yield strength values are then used for the yield strength modeling. The yield strength of the core layer is modeled according to the strong obstacle formulations developed by Esmaeili and co-workers [41]. Accordingly, the contribution to the yield strength by precipitates (i.e. $\sigma_{ppt}$) and solutes (i.e. $\sigma_{ss}$) can be obtained using equations (4-4) and (4-5):

$$\sigma_{ppt} = C f_r^{1/2} \tag{4-4}$$

$$\sigma_{ss} = \sigma_{0ss}(1 - f_r)^{2/3} \tag{4-5}$$

where *C* is a calibration parameter and $\sigma_{0ss}$ is the solid solution contribution to yield strength in the as-quenched condition. The constant parameters *C* and $\sigma_{0ss}$ are obtained from the yield strengths of peak-aged and as-quenched samples, respectively [41]. The yield strength, $\sigma_y$, is then modeled by a linear summation of the above contributions, as well as considering the intrinsic strength of the pure aluminum matrix ($\sigma_i$) according to equation (4-6):

$$\sigma_y = \sigma_i + \sigma_{ss} + \sigma_{ppt} \tag{4-6}$$

The constant modeling parameters used in this work are listed in Table 4-1. In the absence of the experimentally-obtained yield strength value for the as-quenched condition, $\sigma_{0ss}$ is assumed to be similar to that of AA6111 [41]. It should be noted that parameter $\sigma_i$ is from ref. [37] and parameter *C* is an average estimated value from hardness measurements of the peak-aged samples, found to be very close to that of AA6111 [41].

Table 4-1. Modeling parameters.

| Parameters | Value |
|---|---|
| $n$ | 1.0 |
| $Q$ | 43 (kJ/mole) |
| $k_0$ | 54 ($s^{-1}$) |
| $\sigma_i$ | 10 (MPa) |
| $\sigma_{oss}$ | 50 (MPa) |
| $C$ | 330 (MPa) |

The results of the model predictions are presented in comparison with the experimental values (estimated from hardness) in Figure 4-17. The modeling results are generally in good agreement with the experimental values. It is therefore concluded that the approaches developed by Esmaeili and co-workers [41] for modeling the precipitation hardening behavior in monolithic AA6xxx alloys are equally applicable to predict the precipitation hardening within the core layer of the laminated AA6xxx alloys by the mass correction.

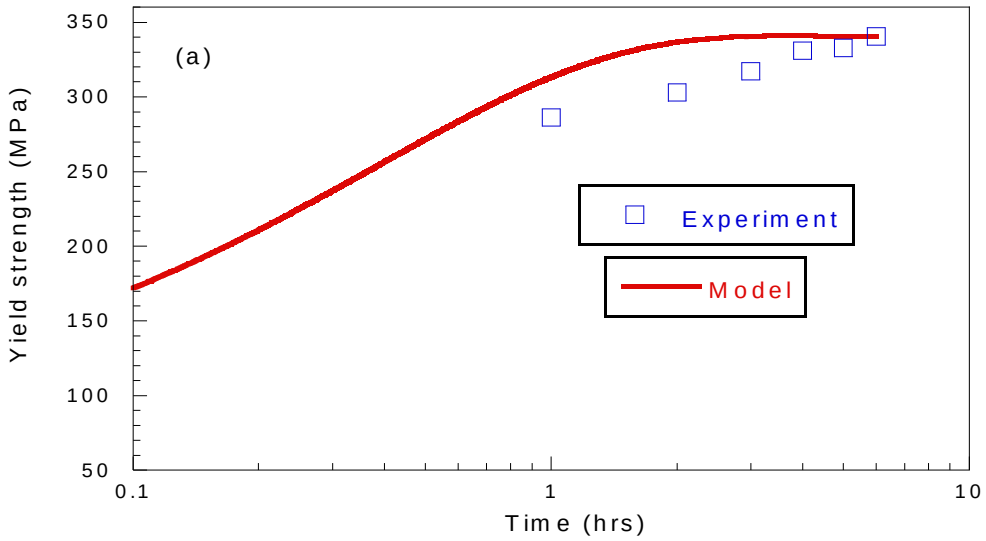
(a)
Yield strength (MPa)
350
300
250
200
150
100
50
0.1
1
10
Time (hrs)
Experiment
Model

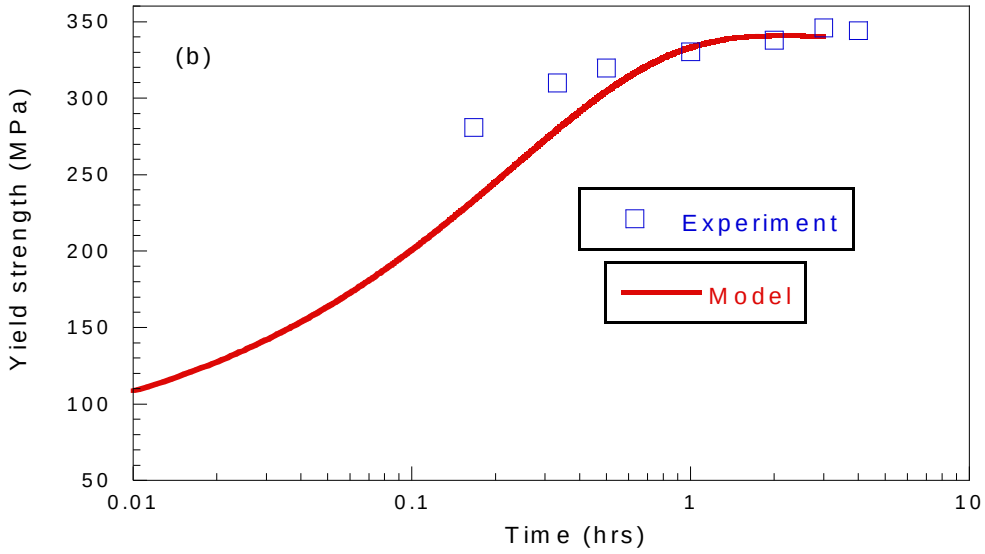
(b)
Yield strength (MPa)
350
300
250
200
150
100
50
0.01
0.1
1
10
Time (hrs)
Experiment
Model

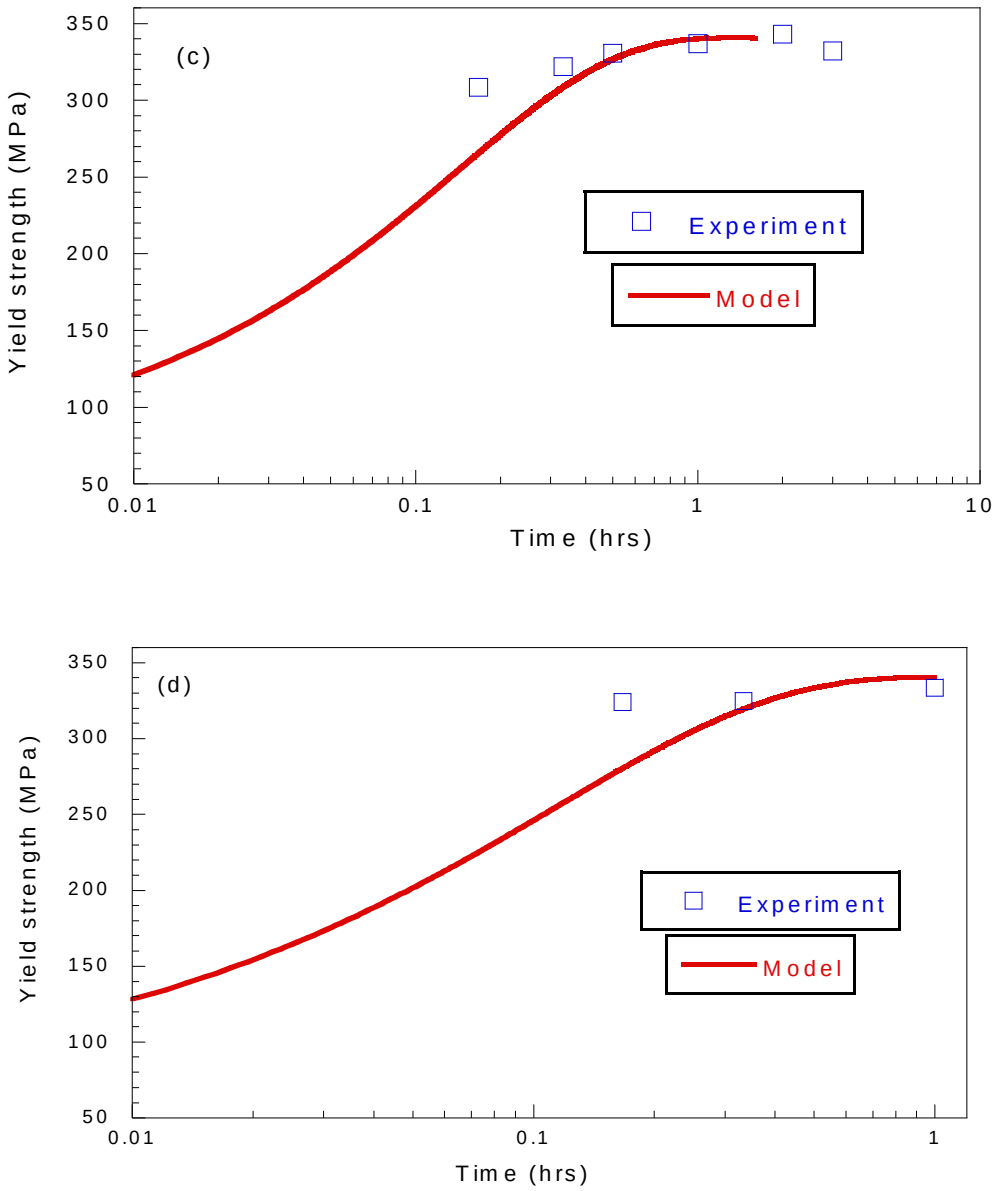


Figure 4-17. The results of model predictions for yield strength in comparison with the experimentally obtained results for (a) 160$^{o}$C, (b) 180$^{o}$C, (c) 200$^{o}$C, and (d) 210$^{o}$C.

## 4.4 Discussion

### 4.4.1 Precipitation behavior associated with the compositional gradient

During nucleation, only nuclei reaching a critical radius, $r^*$, can grow successfully. The critical radius is determined by solute concentration of the matrix, as shown for a given temperature by equation (4-7) and (4-8) [37]:

$$r^* = \frac{r_0}{ln(C_i/C_{eq})} \quad (4\text{-}7)$$

$$r_0 = \frac{2\gamma v_{at}}{kT} \quad (4\text{-}8)$$

Where $C_i$ and $C_{eq}$ are the solute concentration in the matrix and the equilibrium solute concentration in the matrix, respectively. $\gamma$ is the interfacial energy. $k$ and $v_{at}$ are Boltzman constant and atomic volume, respectively. The critical radius of nuclei at the aging temperature of 180$^o$C is calculated for the various matrix concentrations along the cross-sectional profile of the material, and is given in Figure 4-18. The calculation for each curve given in Figure 4-18 is carried on using a single value of interfacial energy γ between the precipitates and matrix. Since the main precipitation phase for aging condition of 180$^o$C-1 h is β″, and the ratio of Mg/Si for both the interface and core layer is larger than 1.73:1 based on the EPMA result given in Figure 4-6, $C_i$ and $C_{eq}$ are chosen as the solute content of Mg, and equilibrium concentration of Mg at 180$^o$C, respectively. The interfacial energy can vary widely from a very low value for coherent interfaces to a high value for incoherent interfaces between precipitates and matrix [106]. It is noted that three different values of γ ranging

from a coherent interfacial energy (0.15 $Jm^{-2}$) to an incoherent interfacial energy (0.8 $Jm^{-2}$) reported for precipitates in Al alloys and the value of atomic volume $2.468\times10^{-29}$ are employed for the calculation [34–36,39,106].

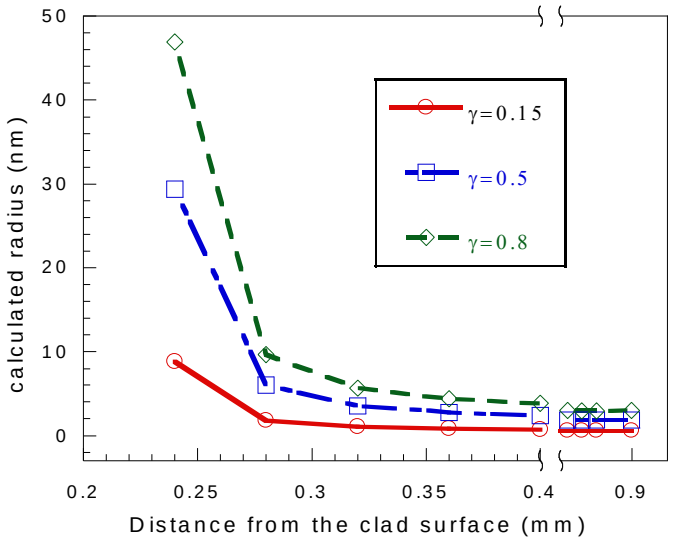


Figure 4-18. The calculated radius of nuclei at different concentrations of matrix.

As Figure 4-18 shows, the critical radius of the nuclei decreases with the increasing concentration of solutes. Moreover, the concentration has a greater effect on the critical radius of the nuclei at a lower value range of concentration. The effect of the value of the interfacial energy γ on the critical radius of nuclei is also compared in Figure 4-18, and it displays that a larger critical radius is needed in the case of a larger interfacial energy for a constant concentration of the matrix. In the case of a coherent precipitate-matrix interface, the critical size of nuclei in the interface region from 0.24 to 0.28 mm from the clad side can be significantly increased with a decreased content of solutes as shown in Figure 4-18.

Miyazaki et al. [161] has also studied precipitation behavior for a Ni-Al alloy containing a macroscopic composition gradient, and their results have shown that larger-sized precipitates form at the location with a lower solute content of the compositional gradient than the location with a higher solute concentration.

In conclusion, a higher number density of precipitates with smaller size is expected for the core layer due to the higher driving nucleation rate and the smaller critical size of nuclei than the interface region, as shown in the TEM images. The hardness profile of aging at 180$^{o}$C for 1 h is attributed to the distribution of precipitates as given in Figure 4-19. It shows that hardening ability scales with the total content of solutes that form the precipitates.

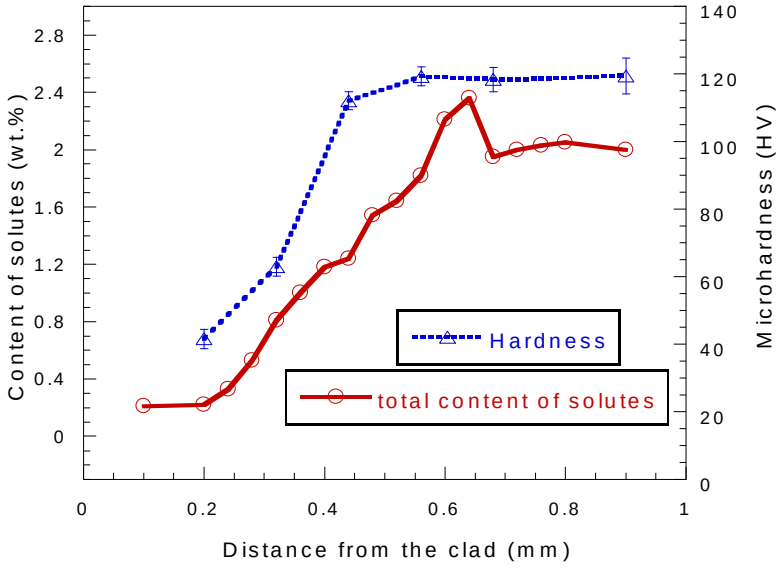


Figure 4-19. Comparison between hardness for the aged sample at 180$^{o}$C for 1 h and composition gradient of total solute for solutionized and quenched condition.

### 4.4.2 **Modeling of the precipitation hardening**

The yield strength modeling employed in this study is effective from unaged until peak-aged stage of aging, and β″ is assumed to be the main strengthening precipitates [41]. It is therefore essential to study if the two conditions apply for the studied laminated material. The DSC traces for both the as-quenched samples, and samples aged at different temperatures are compared and given in Figure 4-20. The aging time for the DSC samples are chosen as the time when the heat flow reach to zero as shown in Figure 4-14 for the IC thermograms as given in Figure 4-9 (6 hrs for 160°C, 3 hrs for 180°C, 2 hrs for 200°C, and 1 h for 210°C). The results shown in Figure 4-20 demonstrate that the first two peaks I and II are almost completely eliminated by aging; whereas the last two peaks III and IV are still present with the same heights as found for the as-quenched condition. It is then concluded that precipitates β″ is the main strengthening phase for the studied aging condition, which is in agreement with the modeling of a monolithic AA 6111 [41].

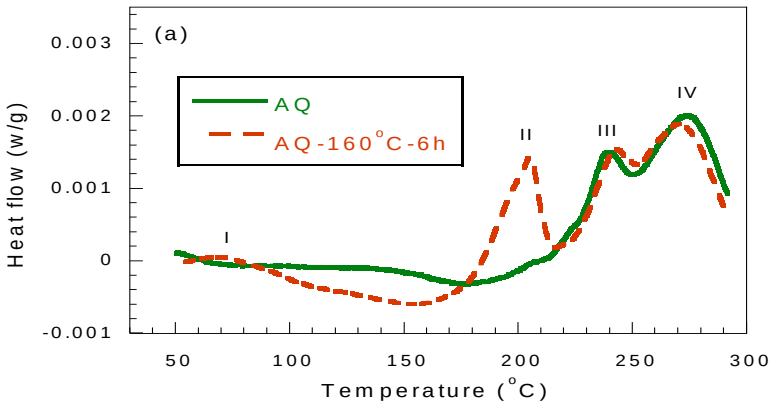

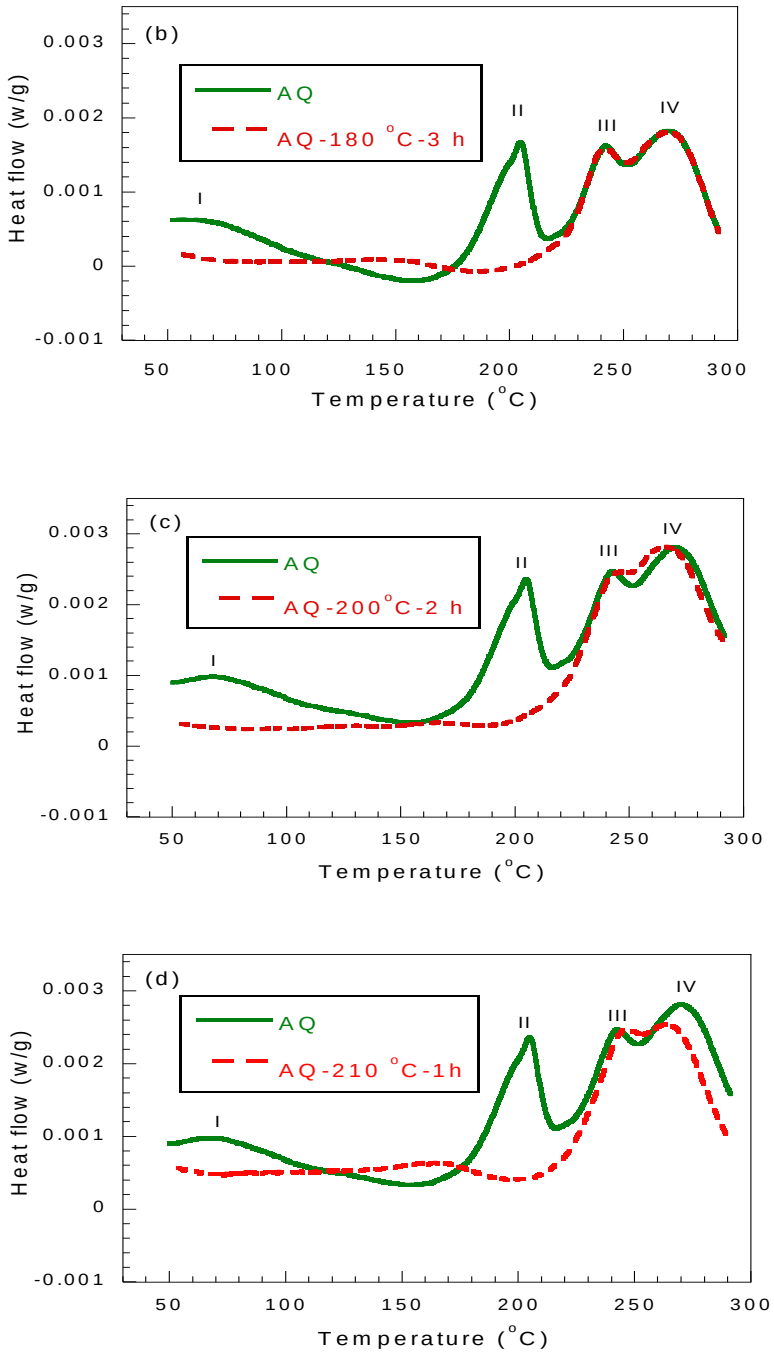


Figure 4-20. DSC traces comparing as-quenched and aged conditions for aging temperatures of (a) 160°C, (b) 180°C, (c) 200°C, and (d) 210°C.

To further understand the behaviour of the bulk laminated system, the studied evolution of $f_r$ during aging is compared with the $f_r$ evolution in previously studied monolithic AA6xxx alloys with the solute contents of those alloys listed in Table 4-2, and the result is given in Figure 4-21. As Figure 4-21 demonstrates, the evolution of $f_r$ with time at 180°C for the laminated system is very similar to those of alloys A (AA6111) and B (AA6451) that contains a high enough level of Cu [162]. It is also clear that there is significant difference of precipitation kinetics between alloys contain a higher level and a lower level of Cu due to the role of Cu on the formation of solute clusters that potentially form during or immediately after quenching (i.e. quenching clusters), as proposed by Esmaeili and Lloyd [27,162].

Table 4-2. Alloy designation and solute concentration (wt. %) of alloys studied in ref. [162]

| Alloy | Mg | Si | Cu |
|---|---|---|---|
| A (AA6111) | 0.79 | 0.6 | 0.70 |
| B | 0.59 | 0.77 | 0.30 |
| C | 0.58 | 0.77 | 0.03 |
| D | 0.62 | 0.81 | - |

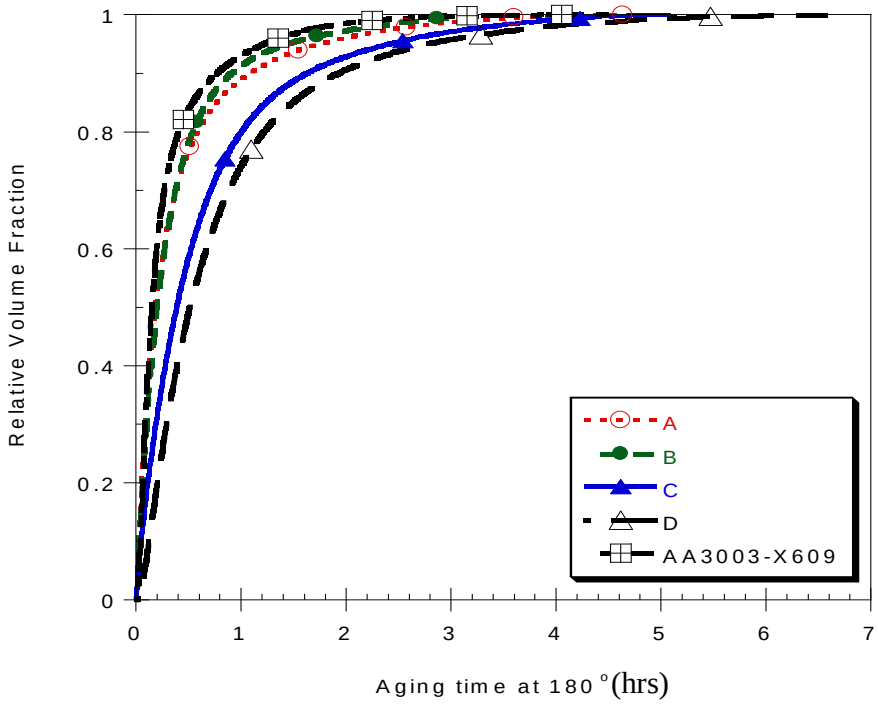


Figure 4-21. The evolution of $f_r$ with aging time at 180°C in A, B, C and D alloys of ref. [162] and the current laminated system (all samples initially solution treated at 560°C and water quenched).

Due to the similar precipitation kinetics featuring the above mentioned main precipitation phase and $f_r$ evolution, the yield strength modeling results are generally in good agreement with the experimental values as given in Figure 4-17. However, there are discrepancies for the lowest aging temperature and short times at higher aging temperatures which are believed to be related to the modeling and experimental error sources discussed in ref. [41]. Hardness measurements and conversion of that data to yield strength values might also be another reason. It also should be noted that the peak yield strength value estimated/predicted in this

work is higher than the value reported for the core alloy in ref. [16] (i.e. ~ 250 MPa for 8 hours aging at 180°C). It is suggested to be caused by natural aging history prior to artificial aging in the work reported in ref. [16]. The effect of natural aging on the following artificial aging behavior of AA6xxx alloys has been widely reported [20,21,41,163]. A natural aging history generally leads to a slower precipitation kinetics and reduced yield strength during artificial aging over temperatures that are relevant to this work.

It is therefore concluded that the approach developed by Esmaeili and co-workers [41,43], for modeling age hardening behavior of monolithic AA6xxx alloys, are equally applicable to predict the precipitation hardening within the core of the Fusion™ AA6xxx alloys.

### 4.5 Summary

The precipitation hardening for precipitates at the interface and core layers are studied for different aging temperatures. Precipitation hardening at the temperatures is also modeled. The findings are summarized as follows:

Combining the results of IC and DSC, reveals that the exothermic heat evolved during isothermal aging at the investigated temperatures is mostly attributed to the formation of β″ precipitates. TEM analysis for the aging condition of 180°C for 1 h at the core layer confirms that the precipitates are needle-shaped β″.

The precipitates at the interface region, 0.3 mm from the clad surface, are smaller in size and lower in number density than in the core layer. It is concluded that a lower nucleation rate

and a larger critical size for nuclei give rise to a lower number density of precipitates with larger sizes at the interface region.

The hardness evolution with aging time at the investigated temperatures demonstrates that the time to reach the peak-aged condition is shorter for a higher aging temperature. The hardness in the interface region shows a gradual increase with distance from the clad surface, which matches the solute profiles of Mg, Si and Cu. At the clad side, a steeper increase is observed than at the core side.

The modeling result is in good agreement with calculated yield strength using the measured hardness. The precipitation hardening model designed for monolithic AA6xxx alloys can be therefore applied to estimate the hardening behavior of the laminated alloy system through an effective mass correction, since the precipitation kinetics of monolithic and laminated AA6xxx alloys is found to be similar.

# Chapter 5 Annealing behavior of a cold rolled AA3003-X609 laminated system

This chapter reports on the investigation of the annealing behavior of the cold rolled laminated alloy system. The annealed microstructure and hardness evolution at various annealing temperatures are studied for the clad and core layers with various thickness reductions. The annealing behavior of the interface region containing a compositional gradient is also emphasized.

## 5.1 Introduction

The annealing behavior of the cold rolled monolithic AA3xxx and AA6xxx alloys has been investigated with various starting microstructures [61,77,82,84–87,141,144,150,164,165]. In order to investigate the effect of precipitation and pre-existing precipitates on recrystallization, custom-designed initial conditions have been employed [65,84,85]. However, the microstructural state in a laminated system processed from thermal-mechanical routes is more complex than those in the studies for monolithic systems. The complexities mainly arise from: (1) the temperature for solutionizing and precipitation behavior are different for the two layers, which makes it is impossible to design an initial condition such as solutionized or aged laminated sheet in order to study the effect of precipitation and pre-existing particles; (2) the difference in the precipitation behavior of AA3xxx and AA6xxx layers during the fabrication history; (3) the presence of a microstructural gradient between the two layers. The current laminated system with an Al-Mn alloy as the clad layer and an

Al-Mg-Si-Cu alloy as the core layer, has been studied for compositional characteristics as the hot rolled and hot rolled and solution treated conditions by Foroozmehr and co-workers [90]. They have shown that compositional gradient in the hot rolled laminated sheet further evolves during solution treatment. In such a laminated system with a dynamic through-thickness compositional gradient and different precipitation capacity through the cross section, a complex recrystallization behavior is then expected. It is therefore important to understand the annealing behavior of such complex systems in order to develop optimized laminated alloys for various applications.

The present work for the first time reports the annealing behavior of a cold rolled laminated AA3xxx-AA6xxx system fabricated using Fusion$^{TM}$ the co-casting technology. This type of laminated sheet can provide desirable combination of strength through the precipitation-hardening capability of the AA6xxx core layer and improved formability due to the presence of the thin AA3xxx layer at the surface [13]. The focus of this study is to establish an understanding of annealing behavior for the clad and core layers in the laminated system fabricated through commercially employed thermal-mechanical processing routes. A better understanding of the annealing behavior for the interface region containing a through-thickness compositional gradient is also addressed.

## 5.2 Material and experimental methodology

### 5.2.1 Material

A laminated AA3003-X609 sheet in the cold rolled condition with a thickness of 2 mm received from Novelis Inc. was employed for the study. The composition profile of the 2 mm thick cold rolled was measured by EPMA (with methodology details given in section 3.3.4), and the result is shown in Figure 5-1. It is clear that there is a compositional gradient of Mg, Si, Cu and Mn between 100 μm and 240 μm from the clad surface of the cold rolled sheet.

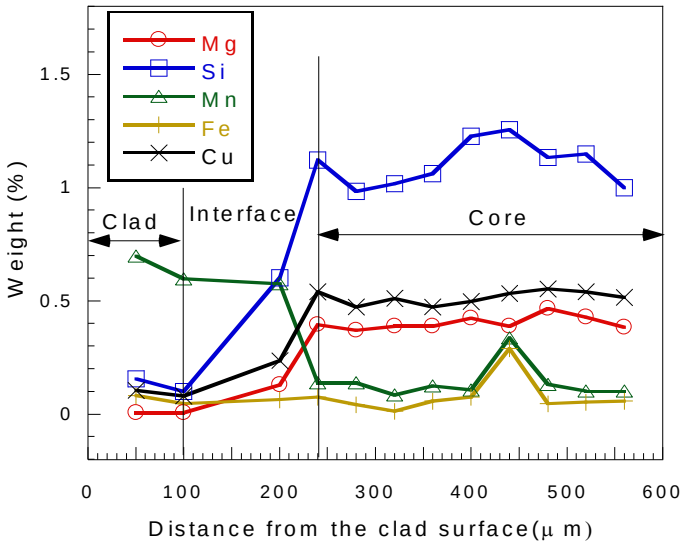


Figure 5-1. The EPMA test results showing through-thickness elemental profiles of the 2 mm thick cold rolled sheet.

Except for the as-received 2 mm thick sheet, two types of cold rolling processes were designed in this study: one was directly cold rolled from the 2 mm sheet; the other one was

solid solutionized at 560$^{o}$C for 15 min, and then was kept at room temperature for 2 weeks before cold rolling. The related sample identification and applied tests are given in Table 5-1.

Table 5-1 Sample identification

| Designation | Process route | test |
|---|---|---|
| 60% CR | As-received 2 mm thick cold rolled sheet | Annealing |
| 80% CR | Directly cold rolled from 60% CR | Annealing, DSC |
| SBR | Solutionizing at 560$^{o}$C for 15 min + water quenching +1 week at room temperature + cold rolling to 1 mm | DSC |

### 5.2.2 **Experimental methodology**

The annealing treatments employed to study the annealing behavior of the cold rolled sheets were given in section 3.2. The microstructure characterization including OM, SEM, EBSD, and TEM were preformed according to the procedures outlined in chapter 3. Image Pro was employed for particle analysis. Each average particle size was obtained from five SEM images as the mean values of particle length and width.

To analyze the recrystallized grain size, misorientation angles between neighboring pixels were first calculated using Euler angles [166]. A standard linear intercept method was then employed to measure the grain size [167], and five lines of data points in the RD and ND

were analyzed for the clad and core layers separately. The average linear intercept size $L_X$ in each direction was calculated by the following equation [168]:

$$L_X = \frac{P_X R_X \delta}{N_X} \qquad (5\text{-}1)$$

$P_X$ , $R_X$ and $N_X$ are the number of pixels, rows of data and the number of the intercepted high angle boundaries, respectively, intercepted in the x direction. Parameter $\delta$ is the scanning step size. The corresponding calculation area for the clad and core layers of the 60% CR sheet was determined based on Figure 5-1: the clad layer is defined as the range with the distance from the clad surface to 100 μm, and the core layer is the region with distance larger than 240 μm.

## 5.3 Results

### 5.3.1 The cold rolled condition

#### 5.3.1.1 60% CR sheet

*The distribution of the pre-existing particles*

SEM images of the cold rolled sample given in Figure 5-2 demonstrate the distribution characteristics of the coarse particles in the cross section of the 60% CR sheet for the clad layer (Figure 5-2 (a)) and the middle region of the core layer (Figure 5-2 (b)). These particles are mostly aligned along the RD in both layers, and the average length of those particles in

the clad layer ranges from 5 to 20 μm with an approximate average aspect ratio of 3.4 (Table 5-2).

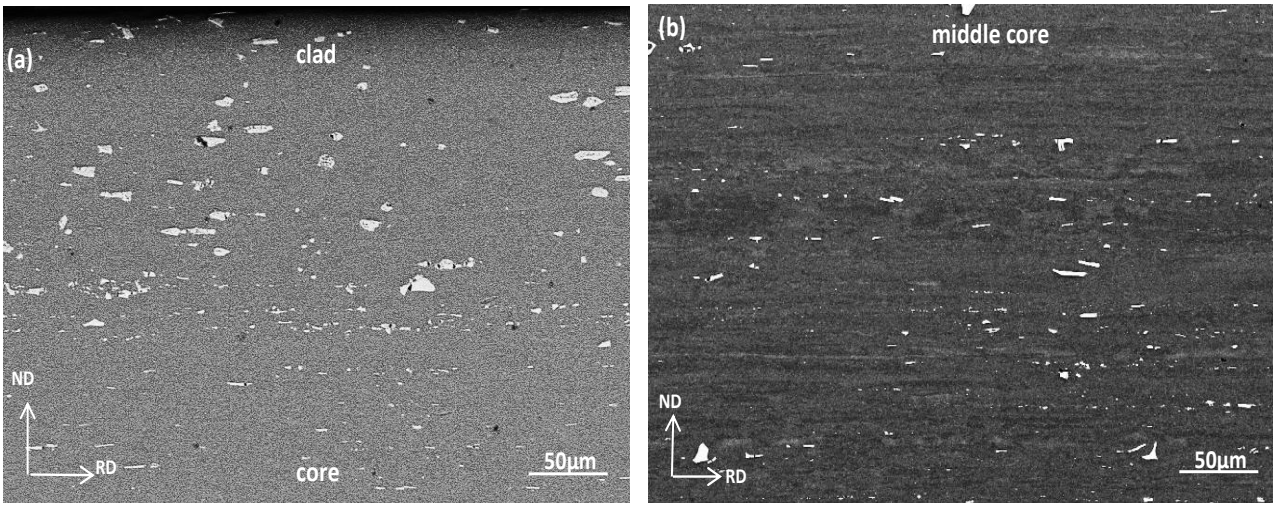


Figure 5-2. SEM images showing coarse particles distribution in (a) the clad and (b) core regions of the 60% CR sample.

EDX analysis shows these particles contain Al, Mn and Fe as shown in Figure 4-1, which is in accordance with the description of the constituent particles Al(Fe,Mn) in AA3xxx alloys [90,113]. The clad might also contain Al(Fe, Mn)Si intermetallic particles [90]. Compared to the clad layer, smaller elongated particles with a length range of 1 to 20 μm are observed in the core layer (Table 5-2). These particles are Al(Fe, Mn)Si intermetallic phase based on the EDX results and the calculated phase diagram [90]. The average aspect ratio of particles in the core appears to be larger than that in the clad layer. Those coarse particles resolved in Figure 5-2 are probably constituent particles formed during casting [146].

Table 5-2. Average size of coarse particles in both layers of the 60% CR sheet with standard deviations in bracket.

| | Length (μm) | Thickness (μm) | aspect ratio |
|---|---|---|---|
| clad | 14.25 (0.79) | 4.19 (0.25) | 3.40 |
| core | 7.23 (0.73) | 0.91 (0.045) | 7.95 |

In addition to coarse particles, fine submicron particles are observable in Figure 5-3. The number density of those particles is significantly reduced in the vicinity of some large particles in both the clad and core layers. Examples of these areas, referred to as precipitate-free zones (PFZs) are circled in Figure 5-3. The size of PFZs is observed to scale with the size of the associated large particles.

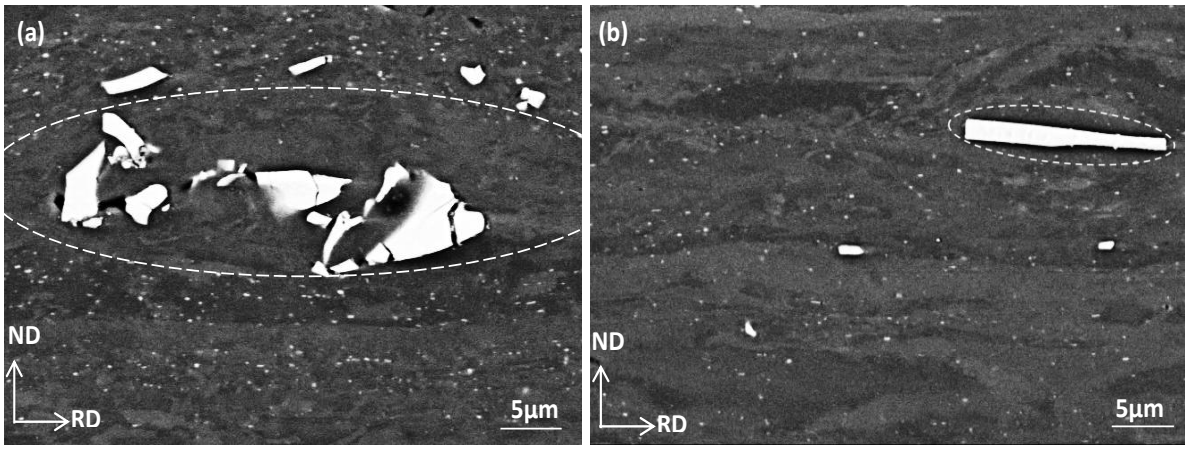


Figure 5-3. SEM images showing fine particles distribution in the ( a) clad and (b) core layers of the 60% CR sheet.

*The deformed structure*

The deformation structure is presented in Figure 5-4. The grains in both the deformed layers are elongated in RD, but grains appear to have a smaller thickness in RD at the clad layer than those at the core layer. The alignment of the deformed grains as given in Figure 5-4 is also found to be disturbed around large constituent particles at both the clad layer and the core layer. It is also noted that the original grain boundaries appear more curved around a particle with a larger size.

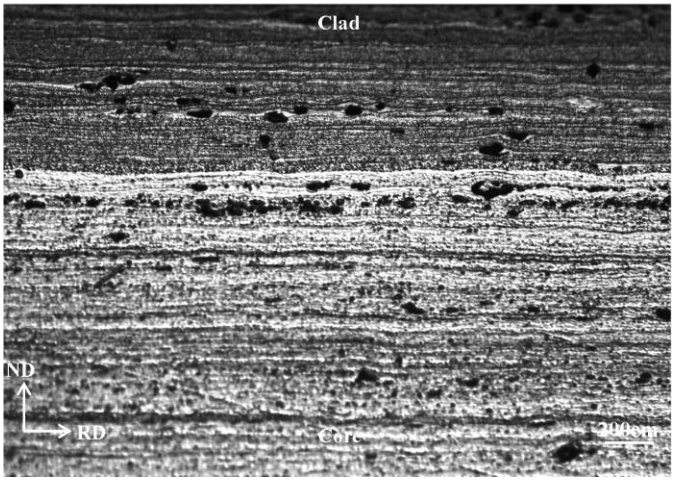


Figure 5-4. The general deformed microstructure of the 60% CR sheet.

Under a close-up observation, deformation zones with a characteristic flow pattern, as shown in Figure 5-5 (a) and (b), are found to surround large particles. The size of the deformation zones are scaled with the size of the large particles in both layers. Deformation zones associated with clusters of large particles, shown in Figure 5-6 (c), are also observed to

overlap. The fine particles in the deformation zones are also observed to distribute along the deformation pattern.

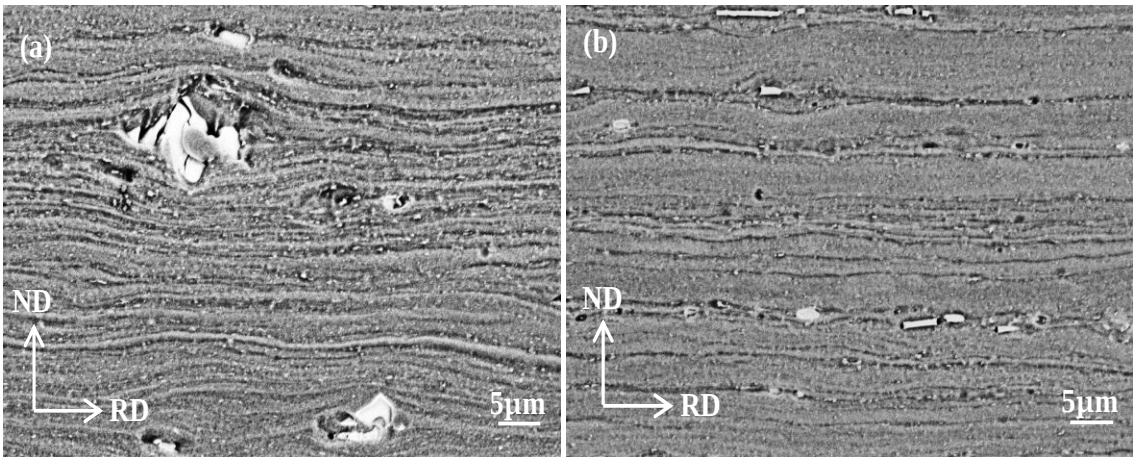


Figure 5-5. The deformation structure associated with coarse particles at (a) the clad layer and (b) the core layer of the 60% CR sheet.

*The effect of fine particles on deformed substructure*

The TEM studies on the as-deformed sample have revealed that a higher number density of dislocations generated during cold rolling tends to form an elongated subgrain structure, as presented in Figure 5-7. The deformation bands shown in Figure 5-7 (b) display a thickness range of 0.15 to 2 μm. The deformation bands are also observed to orientate in different directions, as shown in Figure 5-7 (c), with elongated fine particles distribute along them. A close-up observation, as presented in Figure 5-8, has demonstrated a well-developed cell structure inside the deformations bands. The pinning of particles on the dislocation movement indicated by arrows is also observed as presented in Figure 5-9.

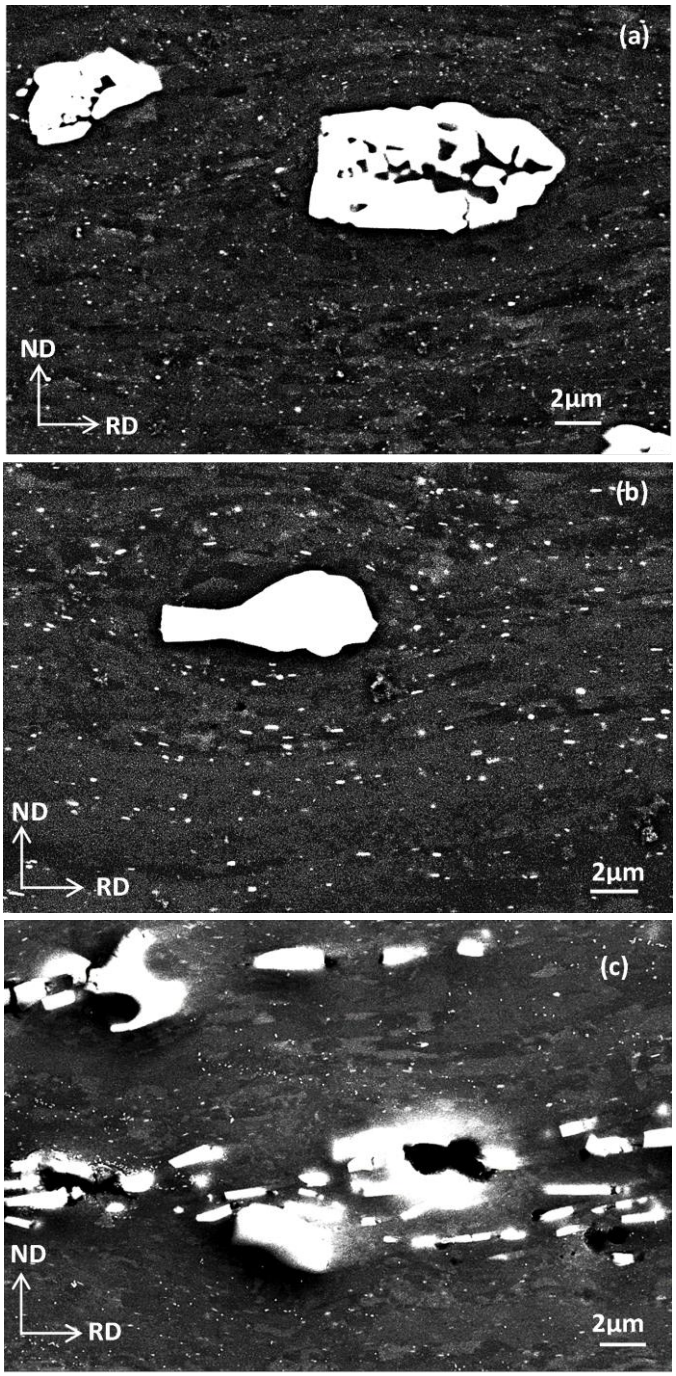


Figure 5-6. SEM images showing the deformation zones associated with the coarse particles in the (a) clad layer, (b) the core layer and (c) the interface region of the 60% CR sheet.

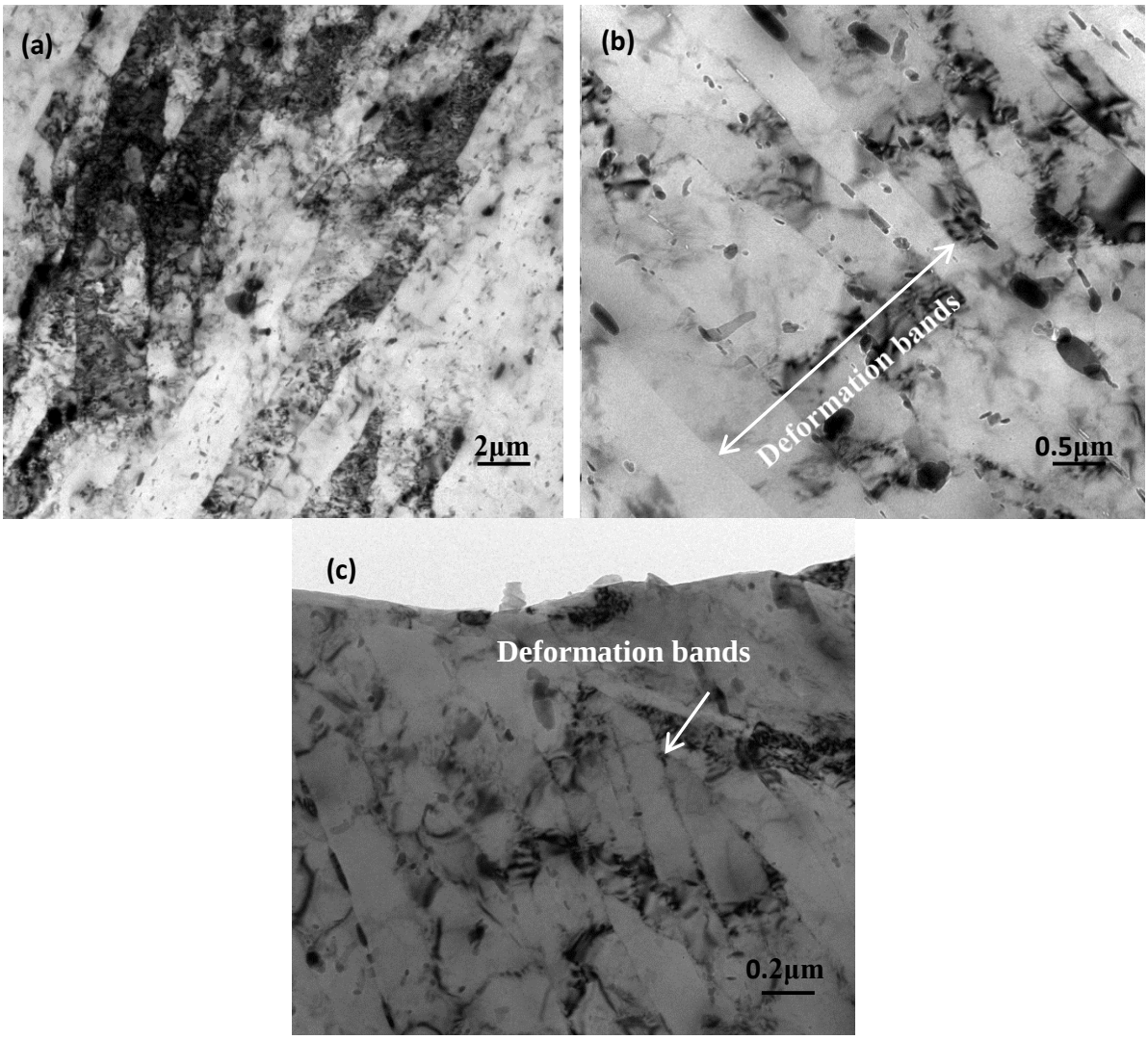


Figure 5-7. The deformed structure of the 60% CR sheet.

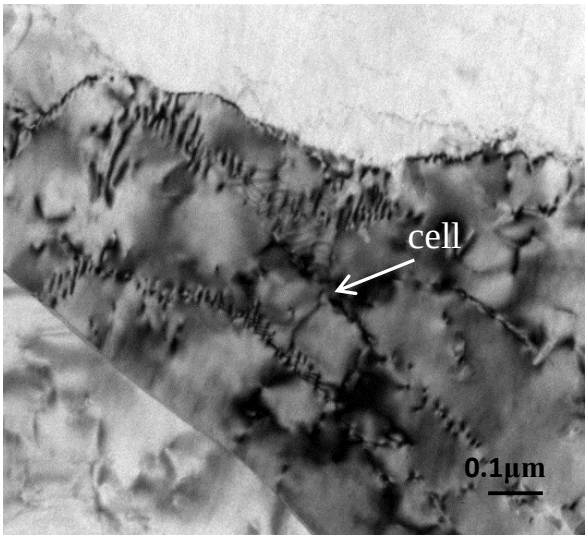


Figure 5-8. The cell structure in a deformation band of the 60% CR sheet.

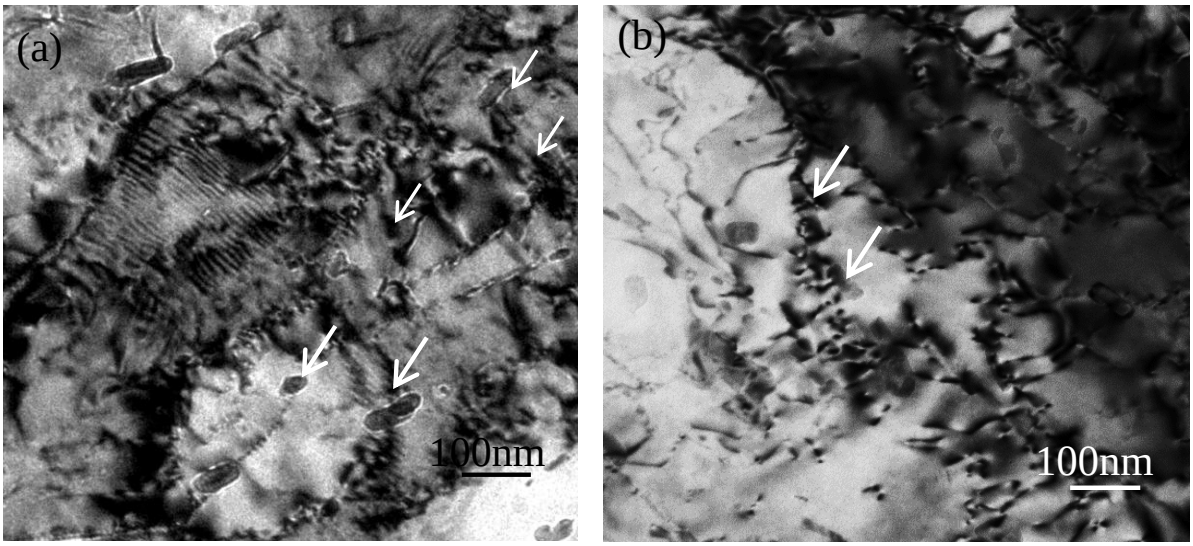


Figure 5-9. TEM images of the formation of dislocation cells associated with fine particles in the 60% CR sheet.

*Hardness profile*

The hardness along the thickness was measured for hot rolled 5 mm thick plate and 60% CR sheet, and the result is given in Figure 5-10. It is clear that hardness of the hot rolled plate increases from the clad surface toward the interface region, and then drops gradually to a hardness value of about 70 HV. The hardness then levels out starting approximately from 350 μm towards the center of the core layer. The highest hardness exists at the range from 250 μm to 300 μm approximately. After the cold rolling with a 60% thickness reduction, the hardness profile of the laminated sheet increases significantly, but follows a similar trend with the distance. The interface region between the clad and core layer demonstrates the largest hardness increase in comparison with the hardness of the hot rolled plate and 60% CR. The largest value of hardness (90 HV) is presented at about 140 μm from the clad side after the cold rolling.

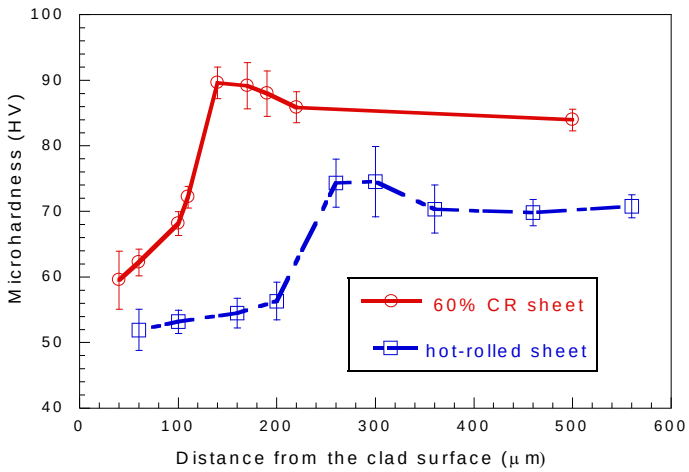


Figure 5-10. Hardness along the distance from the clad surface for 2 mm thick cold rolled plate and hot rolled 5mm thick plate.

### 5.3.1.2 80% CR sheet

The particle distribution for the 80% CR sheet is expected to be similar as that of the 60% CR sheet, therefore only the hardness and EPMA profiles were studied for the 80% CR sheet. The measured hardness was superimposed with the particle distribution across the cross section and given in Figure 5-11. The hardness profile of the 80% CR sheet demonstrates an increasing trend from the clad surface to the highest value at the interface region, and followed by a small and short decrease towards the core layer as shown in Figure 5-11. The highest value of hardness is found to present at the core side of the interface region.

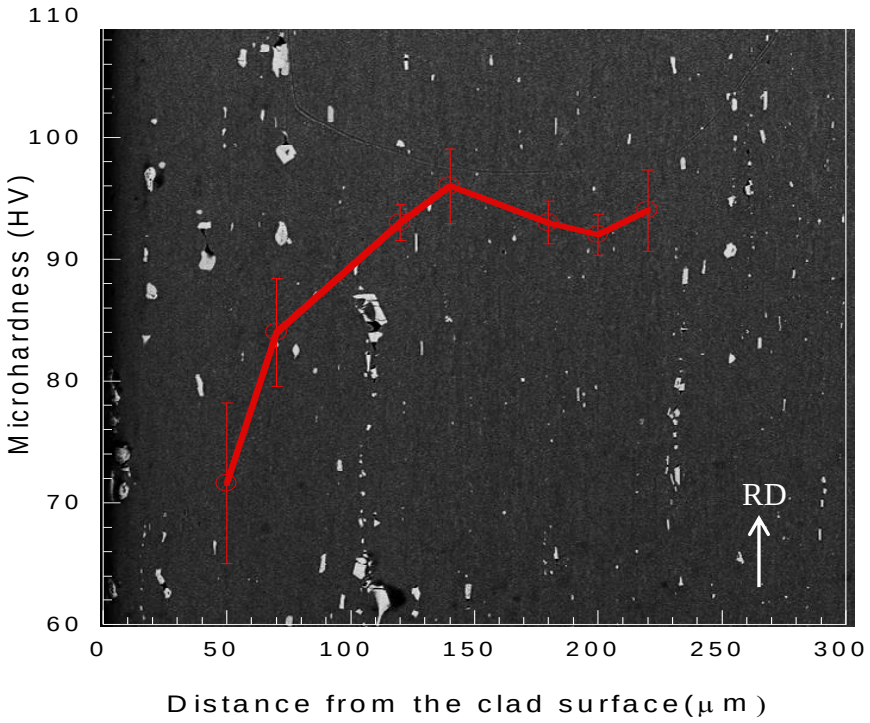


Figure 5-11. The overall distribution of coarse particles for the 80% CR sample superimposed with hardness profile.

The characterization of the compositional gradient together with the particle distribution is plotted together and given in Figure 5-12. The EPMA results display an increasing trend in the content of Mg, Si and Cu, and a decreasing trend in the content of Mn approximately from 60 μm towards 120 μm from the clad surface as shown. The interface range is found to be approximately between 60 and 120 μm for the 80% CR.

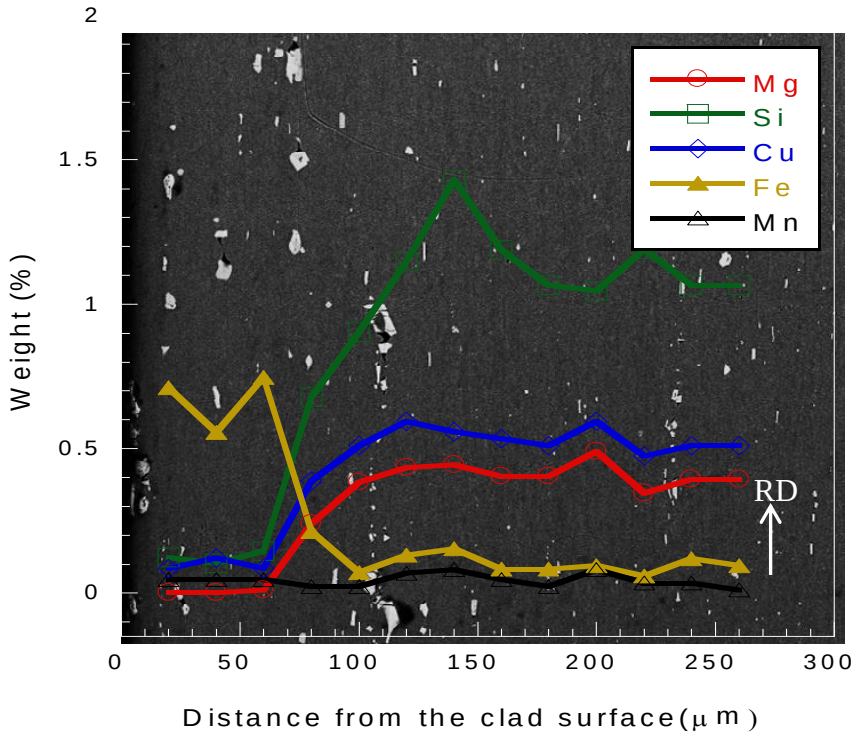


Figure 5-12. The overall distribution of coarse particles for the 80% CR sample superimposed with EPMA results.

### 5.3.2 **Annealing behavior of the clad and core layers**

#### 5.3.2.1 Recrystallization below the solutionizing temperature

##### 5.3.2.1.1 Initial condition: 60% CR sheet

*Hardness evolution with temperature*

The hardness after isochronal annealing at various temperatures for 1 hour for the clad and core layers was measured and given in Figure 5-13. Hardness is observed to decrease after annealing for both the clad and core layers. The clad layer demonstrates a fast hardness reduction for temperatures higher than 300$^{o}$C, whereas, the hardness of the core layer is found to decrease apparently for temperatures higher than 340$^{o}$C. The extent of the hardness reduction is greater at a higher annealing temperature for both the clad and core layers. The lowest hardness for the two layers is obtained at an annealing temperature of around 400$^{o}$C, and the lowest hardness indicates a fully recrystallized condition. A small increase in hardness at 420$^{o}$C observed for the core layer can be caused by the formation of clusters associated with quenching from a high temperature and the partial natural aging process [163].

The hardness evolution with annealing time at 380$^{o}$C was also measured and given in Figure 5-14, with the first hardness values of the clad and core layers as the hardness of the cold rolled condition. As shown in Figure 5-14, the clad layer displays a higher level of hardness reduction in the first ten minutes of annealing. The core layer demonstrates a two-stage

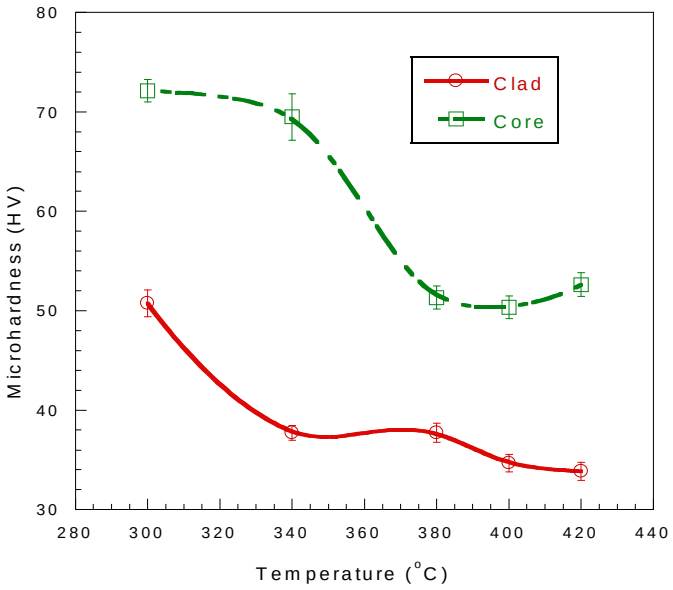


Figure 5-13. Hardness evolution of the 60% CR sheet annealed at various temperatures for 1 h.

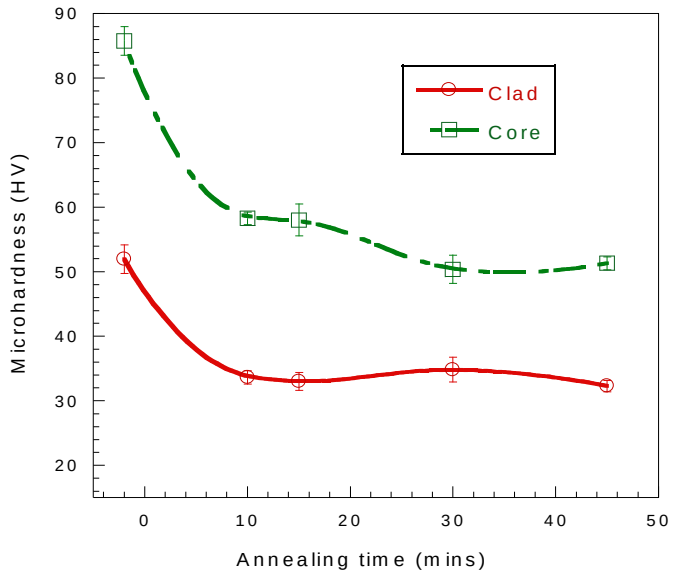


Figure 5-14. Hardness evolution of the 60% CR sheet during annealing at 380°C for 1 h.

reduction of hardness during annealing at 380$^{o}$C. The greater hardness reduction takes place in the first ten mins, but followed by a second smaller reduce between ten and thirty minutes of annealing. The hardness evolution therefore suggests a faster recrystallization at the clad layer than at the core layer.

*EBSD and SEM results*

EBSD maps for the recrystallized samples annealed for 1 hour at different temperatures are shown in Figure 5-15 with grain boundary superimposed. The black and blue boundaries denote high angle boundaries and low angle boundaries, respectively. It is worthy to mention that most of the boundaries in Figure 5-15 are high angle boundaries and only a few low angle boundaries are in blue. The annealed microstructure in the entire area consists of the mixtures of large elongated and small equiaxed grains for the investigated temperatures. It is noted that some of the small equiaxed grains are surrounded by large elongated ones. Most of the recrystallized grains are surrounded by high angle boundaries. A small portion of low angle boundaries is observed to align in RD. The recrystallized grains are more elongated with long straighten boundaries at the core layer than those at the clad layer.

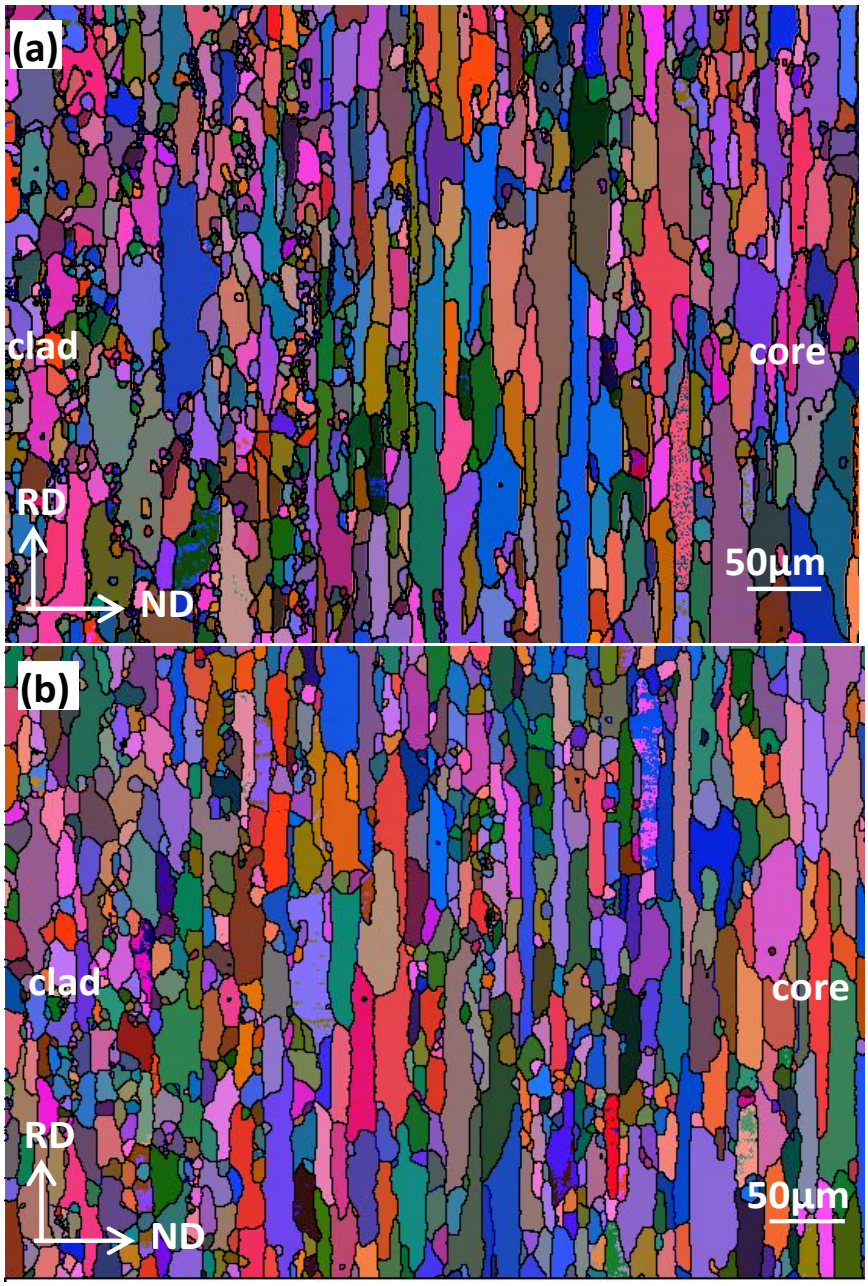
(a)
clad
core
RD
ND
50μm
(b)
clad
core
RD
ND
50μm


Figure 5-15. EBSD maps for the 60% CR sheet annealed for 1 h at the temperatures of (a) 380°C, (b) 420°C, and (c) 480°C (EBSD was conducted by H. Jin).

The calculated average grain sizes in RD and ND for the clad and core layers are presented in Figure 5-16. It can be observed that the grain size of the clad layer demonstrates a slight increase when the annealing temperature increases from 380°C to 420°C, and a slight decrease with the increasing temperature to 480°C. However, the recrystallized grain sizes at core layer display an increasing trend with all the temperatures as shown in Figure 5-16 in both RD and ND.

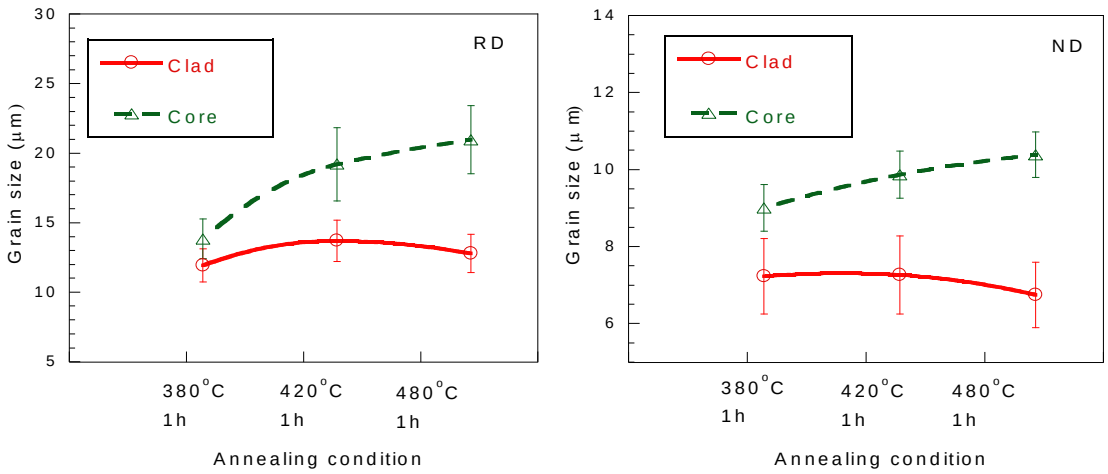


Figure 5-16. The average recrystallized grain size in RD and ND for the annealed 60% CR sheet.

5.3.2.1.2 Initial condition: 80% CR sheet

*EBSD and SEM results*

EBSD maps of recrystallized microstructure for the 80% CR sheet annealed at different temperatures of 380, 420 and 540$^{o}$C are shown in Figure 5-17. The annealed microstructure at 380$^{o}$C for 1 hour consists of a combination of large elongated grains and small equiaxed grains. This is similar to the recrystallized microstructure of the 60% CR sheet under the same annealing condition. However, elongated recrystallized grains become equiaxed for the clad layer and less elongated for the core layer at the annealing temperatures higher than 380$^{o}$C. The transition of the recrystallized grain shape is observed at the temperatures higher than 480$^{o}$C for the 60% CR sheet.

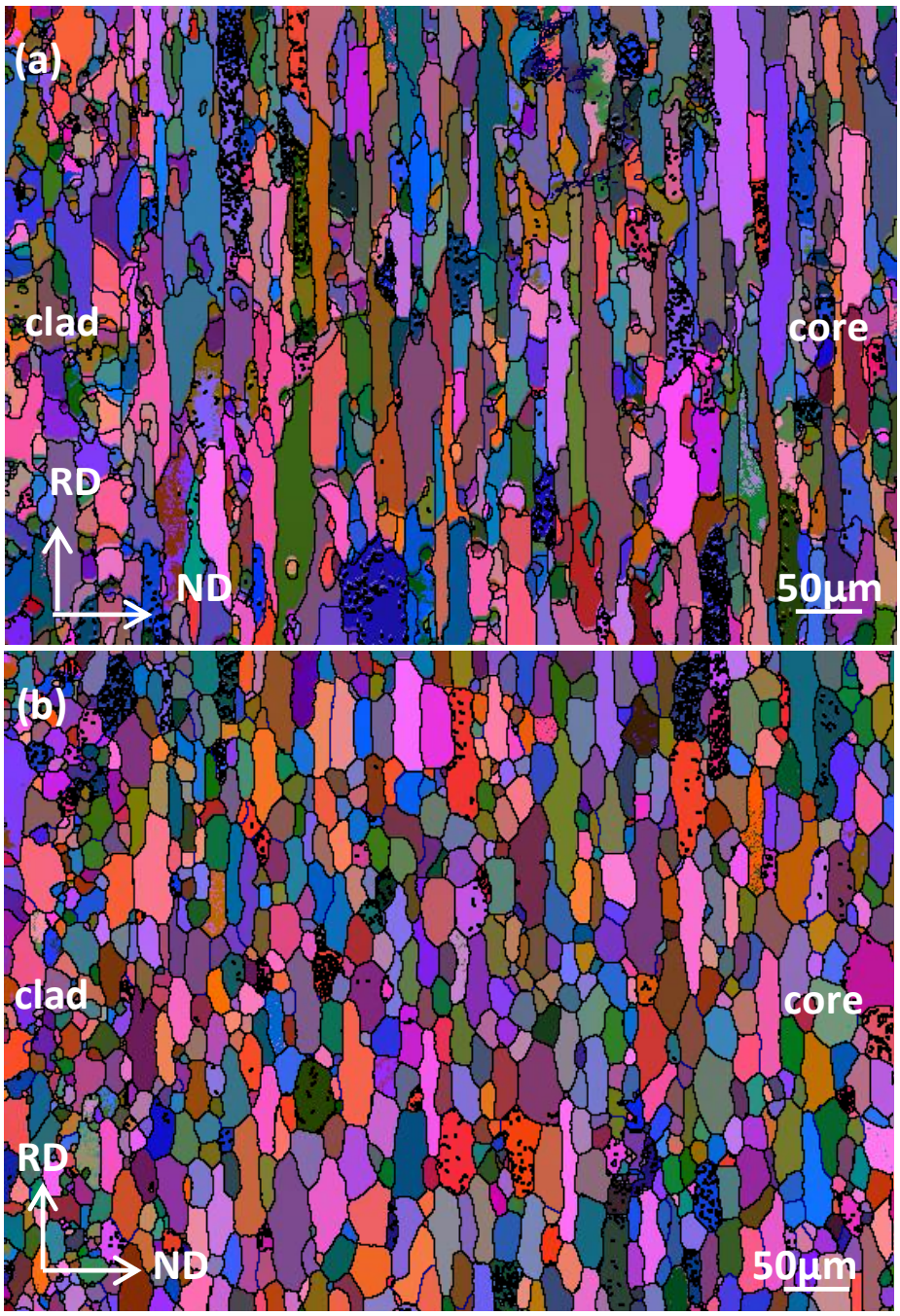


Figure 5-17. EBSD maps of the 80% CR sheet at the annealing conditions of (a) 380$^{o}$C for 1 h, and (b) 420$^{o}$C for 1 h (EBSD was conducted by H. Jin).

The calculated average grain sizes for both RD and ND for the clad and core layers are presented in Figure 5-18. It is observed that the clad layer shows a decreased recrystallized grain size in RD and ND, however, the recrystallized grain size in the core layer displays an increasing trend with the increasing temperature from 380°C to 420°C.

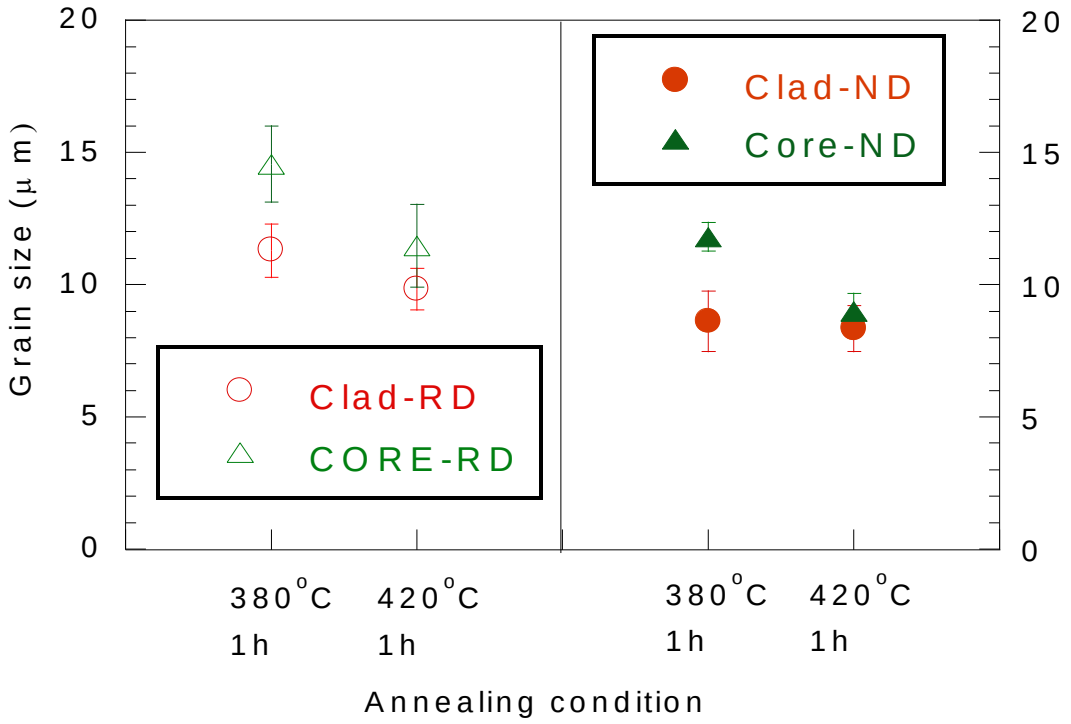


Figure 5-18. The average recrystallized grain size in RD and ND for the annealed 80% CR sheet.

#### 5.3.2.2 Recrystallization at the solutionizing temperature (540$^{o}$C)

*EBSD and SEM results*

The recrystallized grain structures of the 60% CR sheet obtained through annealing at 540$^{o}$C is shown in Figure 5-19. It demonstrates a fully recrystallized microstructure after 30 seconds at this temperature with smaller and less elongated recrystallized grain structure than those annealed at lower temperatures for 1 h. As can be seen in Figure 5-19, an equiaxed grain structure is obtained in the clad layer; whereas, the core layer still shows an elongated grain structure but the grains are less elongated compared to the grains formed at annealing temperatures lower than the solutionizing temperature. Interestingly, the grain sizes in both clad and core layer at 540$^{o}$C are smaller qualitatively than those of samples recrystallized at lower temperatures.

The recrystallized grain structures for the 80% CR sheet samples annealed at the same annealing conditions of 540$^{o}$C for 30 s and 1 min shown in Figure 5-20 are similar to those as shown in Figure 5-19 for both the clad and core layers, but with a slightly larger size in ND. Small amount of low angle boundaries in blue shown in Figure 5-19 and Figure 5-20 is found between neighboring recrystallized grains aligning in the RD direction.

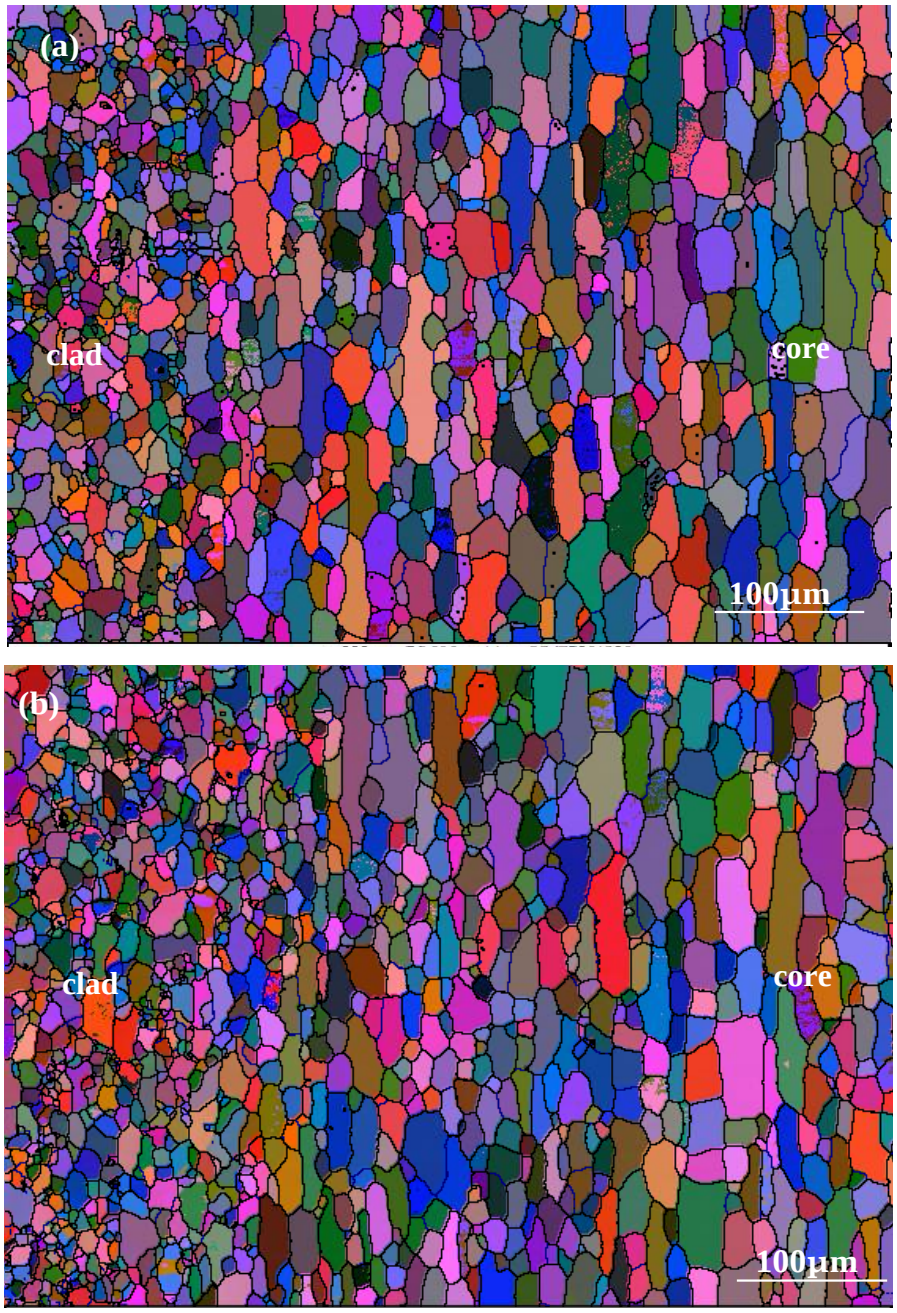


Figure 5-19. The EBSD map for the 60% CR sheet samples at the annealing conditions of 540$^{o}$C for (a) 30 s and (b) 60 s (EBSD was conducted by H. Jin).

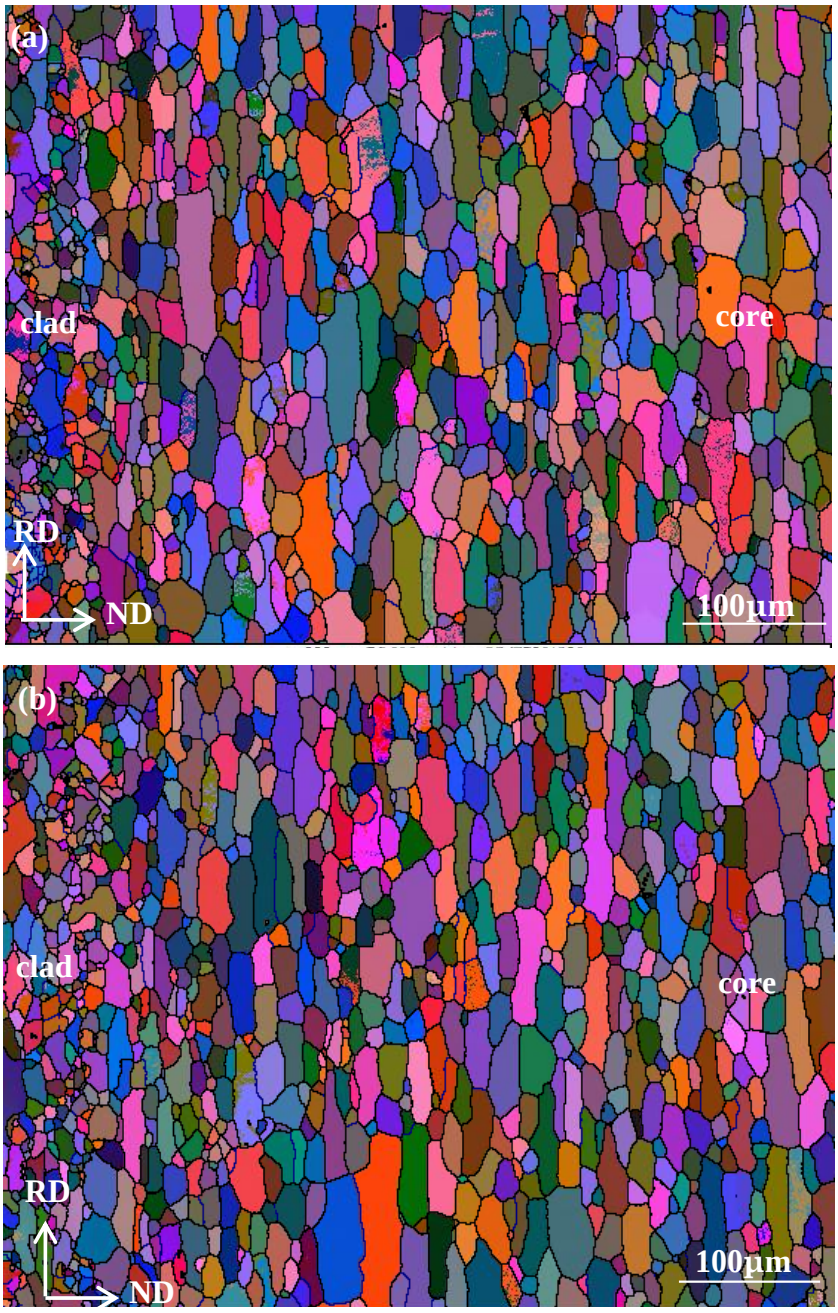


Figure 5-20. The EBSD map for the 80% CR sheet at the annealing conditions of 540$^{o}$C for (a) 30 s and (b) 60 s (EBSD was conducted by H. Jin).

### 5.3.2.3 The aspect ratio of the recrystallized grains

The temperature-dependence of the average aspect ratio of the recrystallized grains for the 60% CR sheet, described as the grain diameter along RD divided by the diameter along ND, is calculated and given in Figure 5-21. The aspect ratio is observed to increase with the annealing temperatures between 380°C and 480°C. The temperature-dependence of the aspect ratio is more apparent in the core layer than in the clad layer in this same temperature range. The smallest aspect ratio is obtained at the annealing condition of 540°C-30 s.

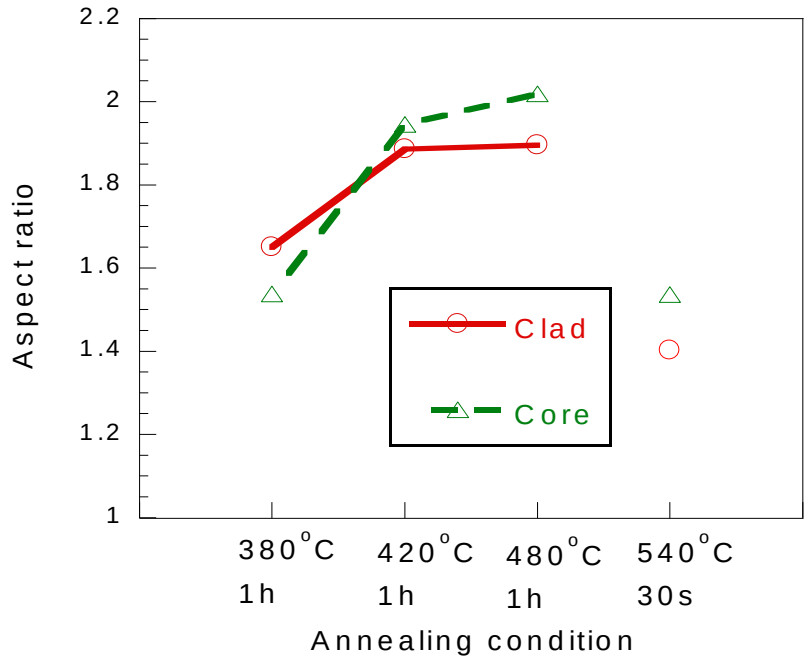


Figure 5-21. The temperature-dependence of the average aspect ratio of the recrystallized grains for the 60% CR sample.

The temperature-dependence of the average aspect ratios of the recrystallized grains for the 80% CR samples is shown in Figure 5-22. The aspect ratios of both clad and core layers decrease with the annealing temperature from 380°C to 420°C. The average aspect ratio of the grains for the samples annealed for 1 h at 420°C is similar to that of the sample annealed for 30 second at 540°C.

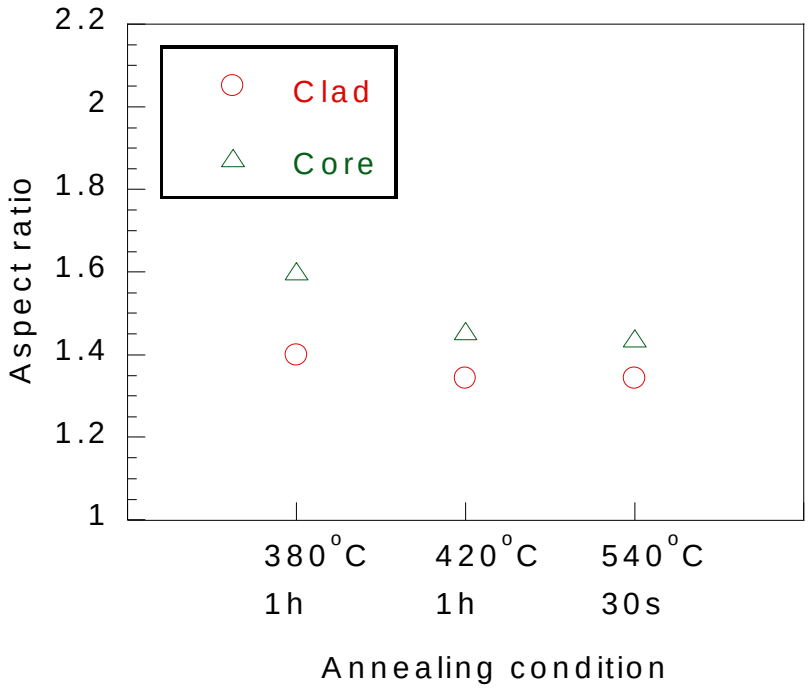


Figure 5-22. The temperature-dependence of the average aspect ratio of the recrystallized grains for the 80% CR sample.

*Phase transformation during annealing at 540 °C*

The particle distributions for the core layer before and after the annealing at the solutionizing temperature are compared in Figure 5-23. It is recognized that the number density of fine

particles resolved in Figure 5-23 (a) increases, and the plate-like particle transfer into globular, which suggest a phase transformation taking place during annealing at this temperature.

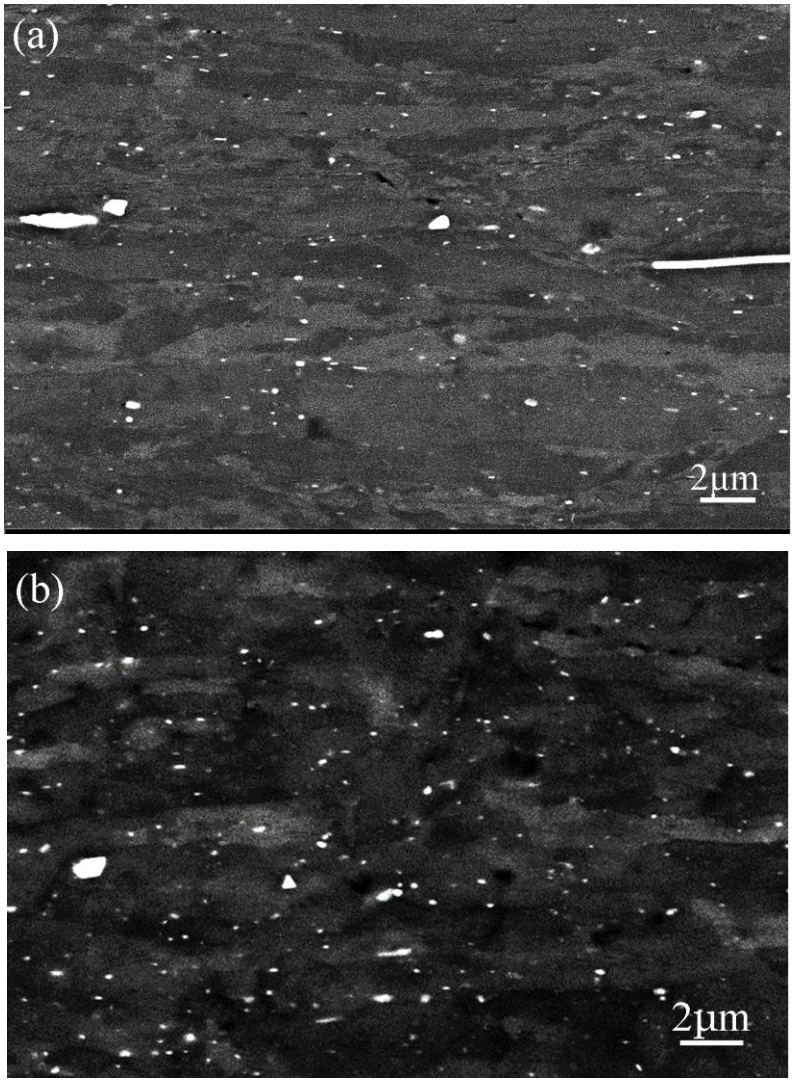


Figure 5-23. The particle distribution in the core layer of the 2 mm cold rolled sheet (a) before and (b) after annealing at 540$^{o}$C for 30 s.

The precipitates at the core layer including $Mg_2Si$, Si and Q phase are expected to dissolve at 540°C [90]. The dissolution of fine particles at 540°C was confirmed by comparing EPMA data for hot rolled condition. In order to obtain more data points across the interface, the hot rolled sample with 5 mm thickness was chosen of EPMA measurement. The solute profile of Mg, Si and Cu for both the hot rolled plate and the plate after heat-treatment at 540°C for 30s are compared in Figure 5-24. The content of Mg, Si and Cu is observed to increase due to the dissolution of $Mg_2Si$, Si and Q phases. There is no apparent change in the weight percent of Mn, which indicates that the particles containing Mn are very stable. A more appreciable enrichment of solutes is also observed in the interface than the core layer.

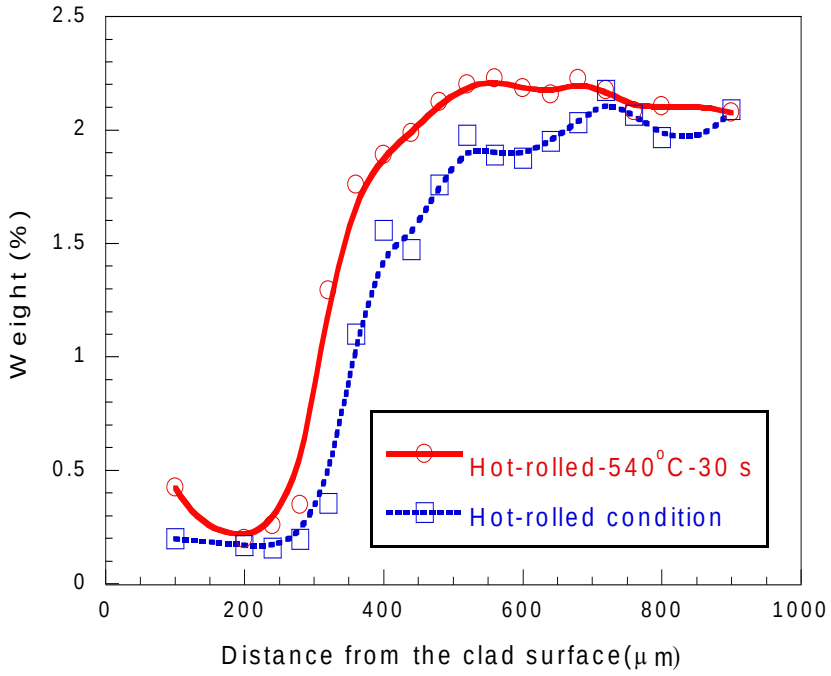


Figure 5-24. The distribution of the total weight percentage of Mg, Si and Cu for the hot rolled condition and the heat treated condition

(Hot rolled and solutionizing at 540$^{o}$C for 30 s).

### 5.3.3 **Recrystallization behavior associated with the interface region**

The investigation of the recrystallization behavior associated with the interface region was conducted on the 80% CR sample annealed at a low temperature of 300$^{o}$C. The recrystallized microstructure was studied using EBSD. Precipitation and evolution of the pre-existing particles during annealing were also investigated by hardness measurement, DSC and SEM.

*EBSD and SEM results*

The EBSD orientation maps for different annealing conditions presented in Figure 5-25 demonstrate the progress of recrystallization in different layers during annealing at 300ºC. As given in Figure 5-25 (a), there is no sign of recrystallization in the entire investigated area after annealing for 1 h. Recrystallization of the laminate is found to initiate from the interface region between the clad and core layers within the first 2 hrs of annealing. With increasing the annealing time to 4 hrs, the recrystallized region is observed to develop slightly towards the core side with a width of ~95 μm. The recrystallized range is further extended towards the core side into an approximate 220 μm-wide range with continuing annealing for 6 hrs.

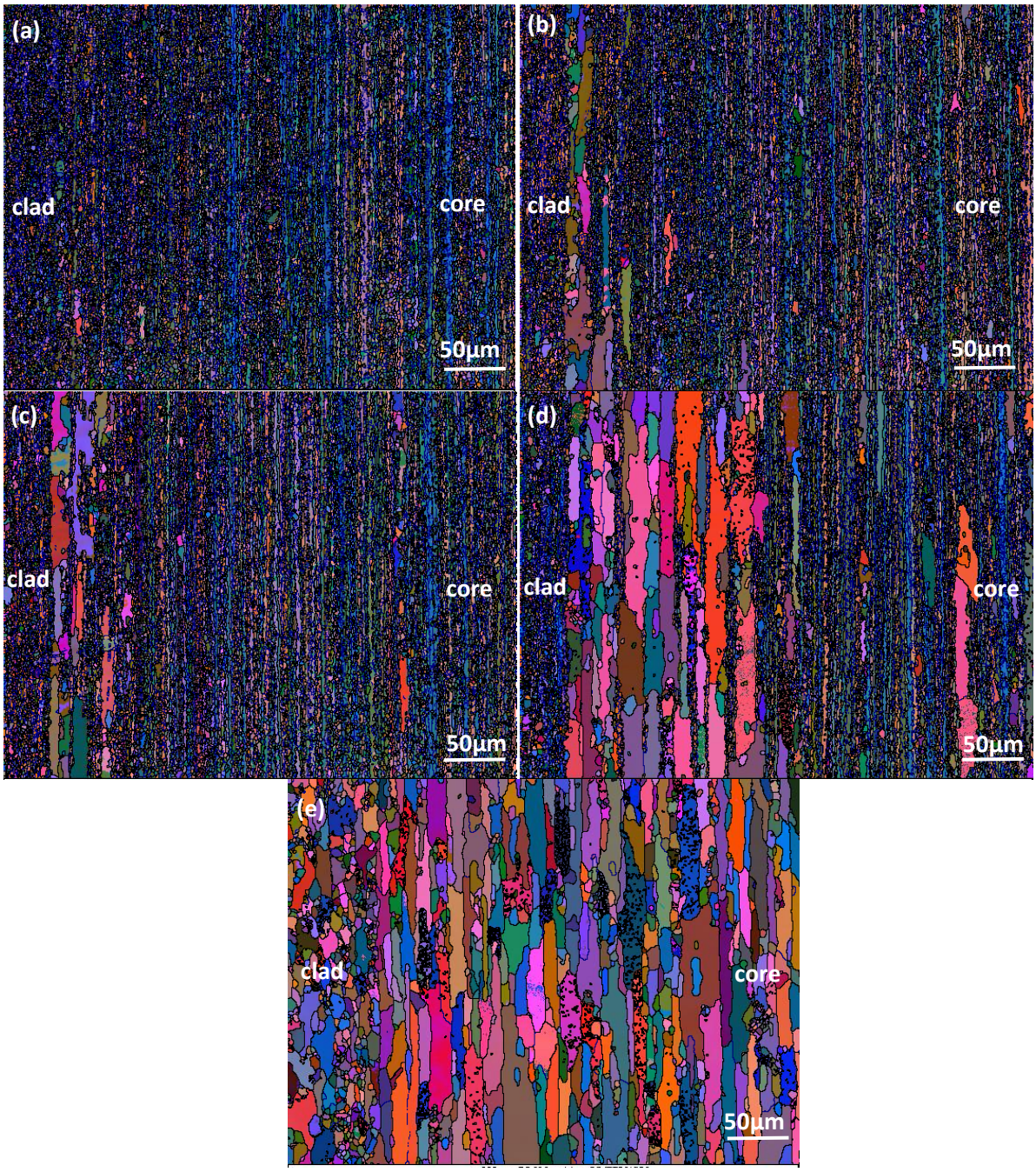


Figure 5-25. EBSD maps showing the microstructure of the 80% CR samples annealed at 300$^{o}$C for (a) 1 h, (b) 2 hrs, (c) 4 hrs, (d) 6 hrs and (e) 24 hrs (EBSD was conducted by H. Jin).

It is also noticed that the apparent initiation of recrystallization at the clad and the core layers are still retarded in the first 6 hrs of annealing, although recrystallized grains are observed at some scattered locations of the core layer. The fully recrystallized grain structure for the entire cross section is obtained after annealing for 24 hour as shown in Figure 5-25 (e). Interestingly, the finest recrystallized grain structure is observed in the clad layer and the interface region, while the largest grains form in the core layer.

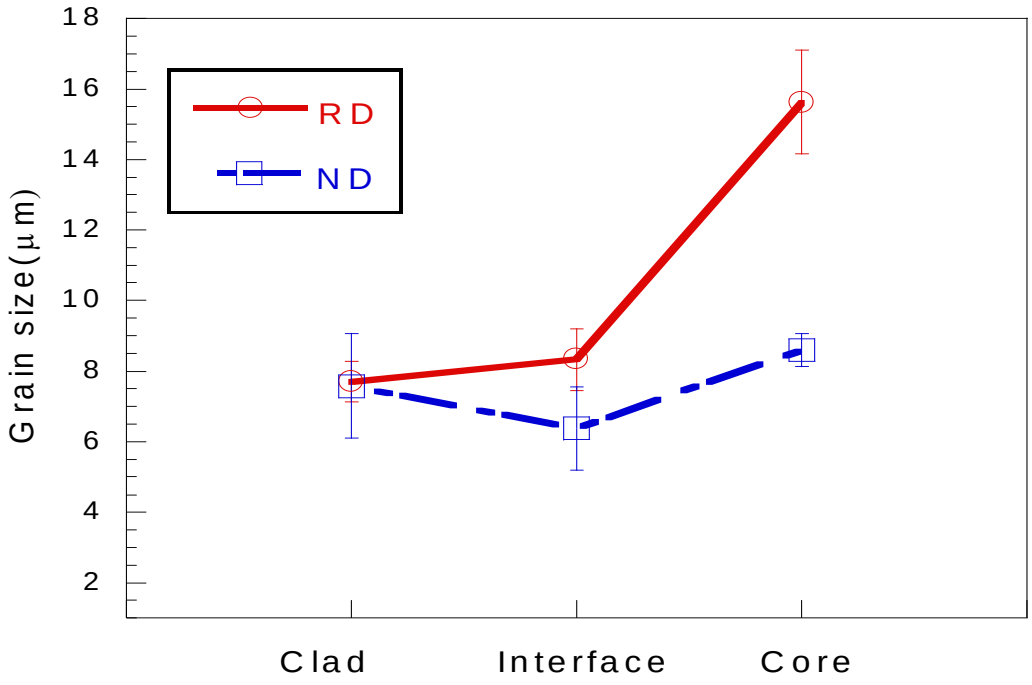


Figure 5-26. The average grain diameter in the RD and ND for the 80% CR sample annealed at 300$^{o}$C for 24 h.

The average grain size data calculated separately in RD and ND for the three different layers is shown in Figure 5-26. The EBSD maps in Figure 5-25 (e) show that the clad layer contains

a high fraction of very fine equiaxed recrystallized grains. The average size of this layer is approximately 8 μm in both RD and ND, as reported in Figure 5-26. Figure 5-26 further indicates that the calculated average grain diameters in RD are larger than in ND at both interface region and core layer. Particularly, the grain structure in the core layer is highly elongated in the RD. The calculated grain diameters in the ND of all locations of clad, interface and core are generally similar.

*Precipitation during annealing*

To investigate the precipitation capacity of different layers of the 80% CR sample, DSC experiments were carried out on both the bulk laminated material and the material with the clad layer removed. In the latter case, the clad layer was removed by mechanical grinding prior to the DSC testing of the sample. As shown in Figure 5-27, the DSC trace of the material with the clad layer demonstrates two exothermic peaks in the temperature range of 50-300$^{o}$C, centered at about 175$^{o}$C and 270$^{o}$C, respectively. The DSC trace of the sample without clad layer reveals a single exothermic peak centered approximately at 175$^{o}$C, but no peak is observed at the higher temperature range. The comparison of the two traces suggests that the peak centered at 270$^{o}$C for the bulk laminated material is associated with a precipitation transformation in the clad layer, as it disappears when the clad layer of the sample is removed. Peak I, therefore, represents the reactions that take place mainly in the core layer, with some potential effects from the relatively thin interfacial layer.

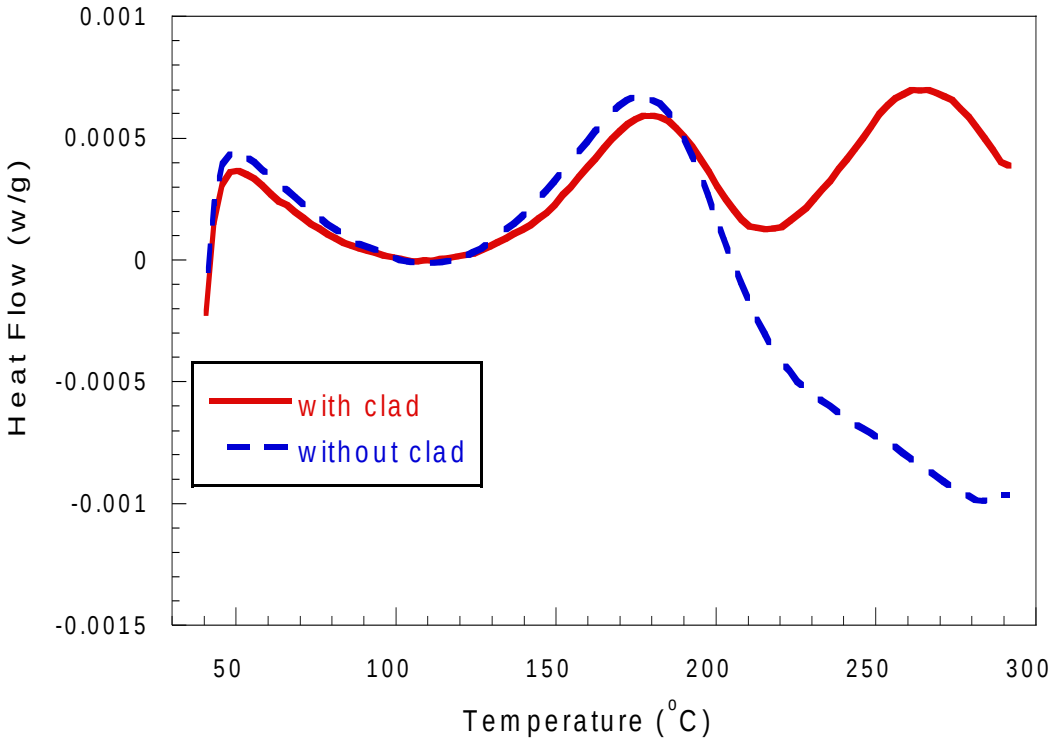


Figure 5-27. DSC traces obtained from the 80% CR samples with and without the clad layer.

To further study the precipitation reactions that possibly take place during annealing, DSC experiments were conducted on samples with different starting conditions. Figure 5-28 presents the results for the cold rolled sample (CR), SBR sample, and the samples cold rolled and annealed at 300°C for 1 h and 4 hrs (CR-300°C-1 h, CR-300°C-4 h, respectively). The DSC traces for the CR and SBR samples show two exothermic peaks centered approximately in the range of 170-190°C (peak I) and at ~270°C (peak II). However, the magnitude of peak I for the CR sample is significantly smaller than that for the SBR sample. This finding further supports the above suggestion that Peak I represents the core layer. As the core of the SBR

sample undergoes solutionizing prior to cold rolling, more precipitates form during its DSC run and thus a larger heat release is detected.

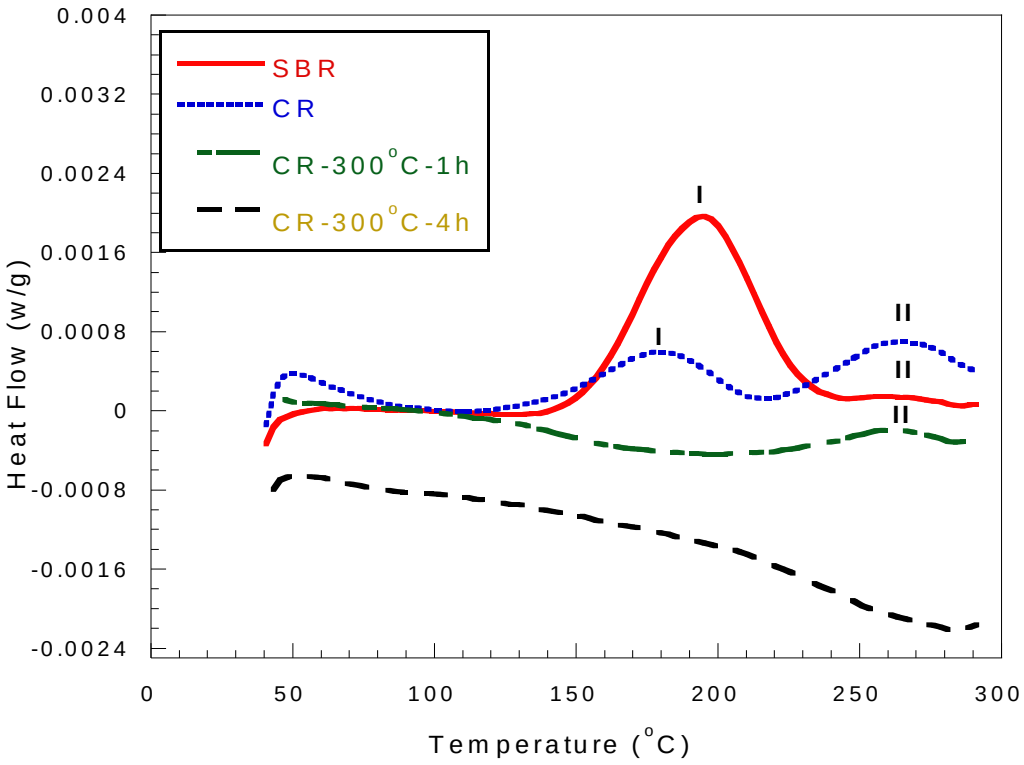


Figure 5-28. DSC test results of samples with different starting conditions.

The DSC trace for the CR-300-1 h sample shows only peak II, while no exothermic peak is detected for the CR-300-4 h sample, which suggests that the precipitation reactions associated with peak I, i.e. core (and potentially interface), already occurs during the first 1 h of annealing at 300°C. The DSC trace also demonstrates that precipitation processes associated with peak II are also completed after annealing for 4 hrs. It is therefore suggested that the precipitation reactions in the clad layer takes longer compared to the core layer but

mainly occur within the first 4 hrs of annealing. Considering the above findings in connection with the EBSD results, it is concluded that the entire laminate system experiences precipitation prior to recrystallization when annealing is conducted at 300$^{o}$C.

The distribution of the fine particles revealed by SEM under a high magnification for the cold rolled condition and annealed condition are compared and shown in Figure 5-30. It is clear that the SEM resolvable particles at the interface region increase in number density after annealing for 6 hrs at 300ºC by comparing Figure 5-29 (a) and (b). The increase in number density of these particles indicates precipitation of new precipitates and also the growth/coarsening of the pre-existing fine particles during annealing. It is noteworthy that the observed particles cannot fully represent their number density (i.e. total volume fraction), since the existing smaller particles could not be resolved by SEM.

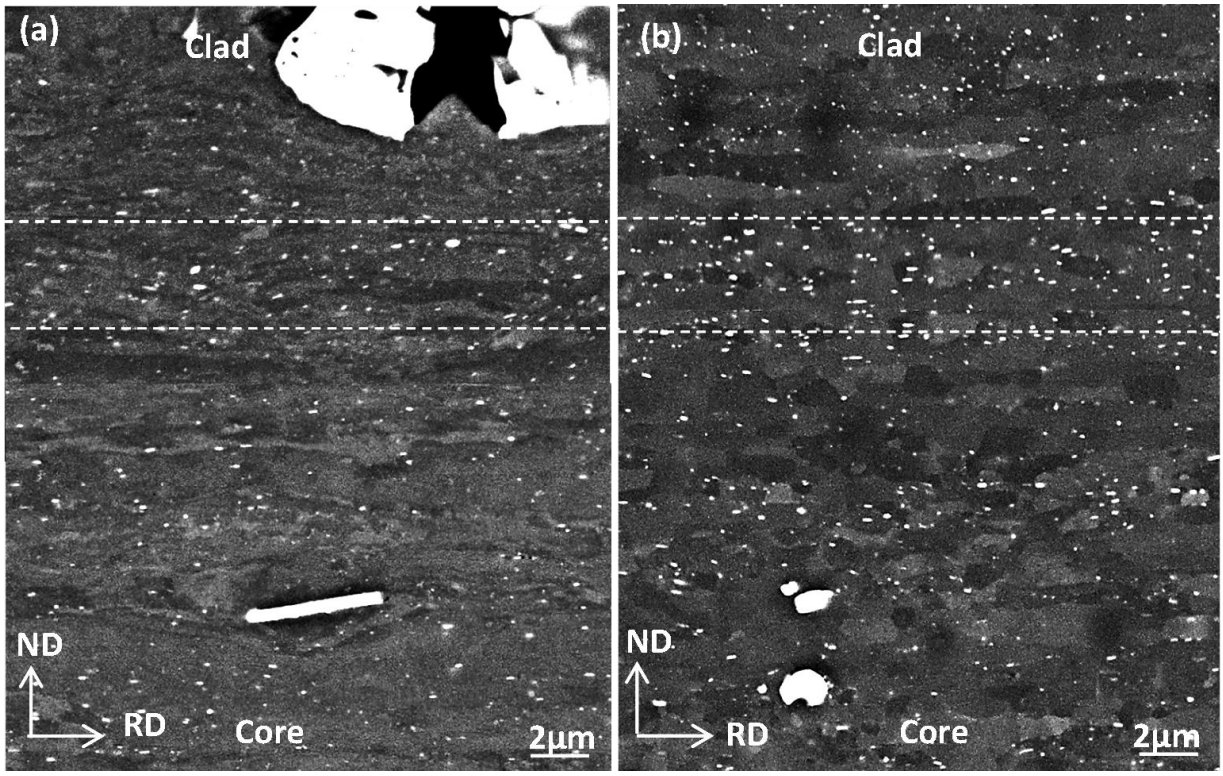


Figure 5-29. The distribution of resolvable particles for (a) the 80% CR and (b) the 80% CR annealed for 6 hrs at 300ºC.

The solute distributions through the cross section after annealing for 4hrs and 6 hrs were measured using EPMA. The results are superimposed in the corresponding EBSD maps in Figure 5-30. Comparison between the EPMA profiles of the cold rolled condition as given in Figure 5-12 and the annealed conditions as shown in Figure 5-30 demonstrates a more significant and uneven distribution of the content of Mg, Cu and Si. The recrystallized regions show a large fluctuation of Si as shown in Figure 5-30.

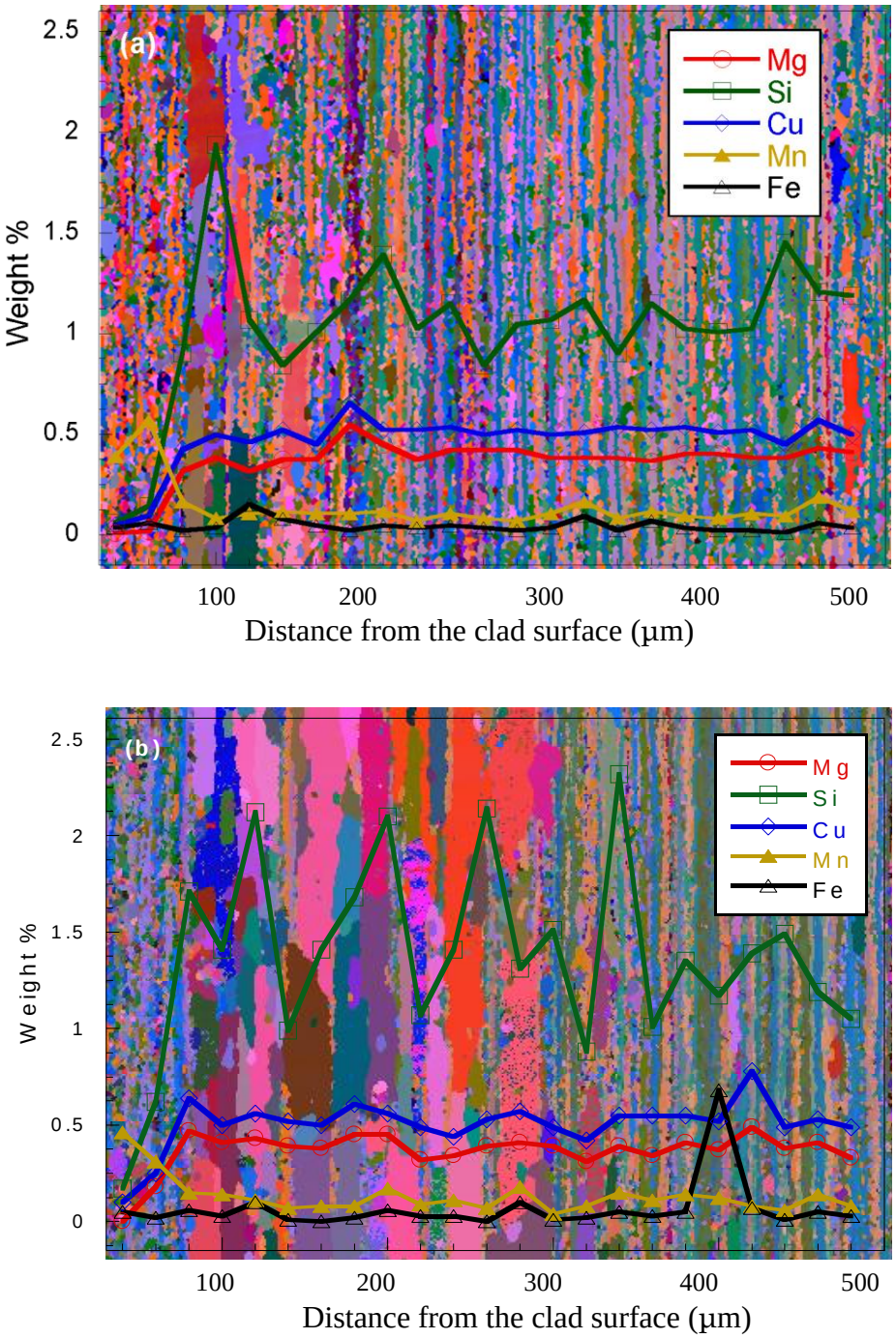


Figure 5-30. The EBSD maps with EPMA profile for the 80% CR samples annealed for (a) 4 hrs and (b) 6 hrs at 300$^{o}$C (EBSD was conducted by H. Jin).

*Evolution of hardness during annealing*

In order to investigate the softening rates of different layers, the hardness profile through the cross section of the cold rolled sample was measured. Figure 5-31 presents the hardness development after annealing for 1 h, 6 hrs and 24 hrs, respectively. It is observed that the hardness of the 80% CR sample increases from the clad layer towards the core layer with the highest value at the distance of about 140 μm. The hardness at the distance larger than 140 μm is similar to the hardness of the core layer. The hardness of the entire laminate decreases significantly, and the original hardness peak disappears after annealing for 1 h. With increasing the annealing time to 6 hrs, the hardness in the region with the distances from about 100 μm to 240 μm displays a greater reduction than that of the core and clad layers. The hardness profile of the laminate demonstrates a continuous decrease after annealing for 24 hrs, but hardness of the interface region from 100 μm to 160 μm remains similar.

Hardness evolution during annealing for the representative distance of the interface and core layers (the middle of the interface region and core layer, respectively) was also measured and is shown in Figure 5-32. The boundary of the original interface region is indicated in Figure 5-32 base on the EPMA profile as given in Figure 5-30. Both layers demonstrate a fast decrease in hardness in the first 6 hrs of annealing, but with a faster reduction at the interface region. The hardness of the interface region remains at a plateau level between 6 and 24 hrs, in which recrystallization is completed at the interface region according to the EBSD results.

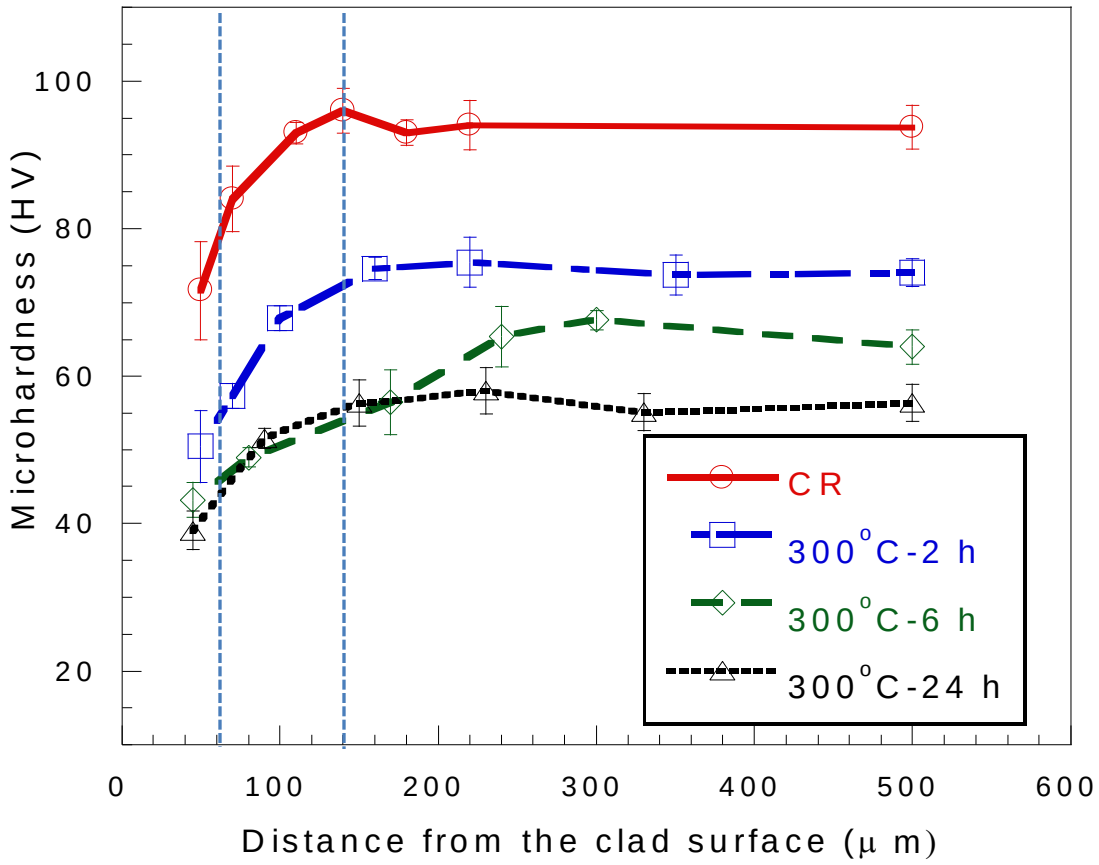


Figure 5-31. The development of the hardness through cross section for both the 80% CR and annealed conditions at 300°C.

The average hardness of the core layer slowly decreases during the extension of annealing to 24 hrs, which suggests the continuation of recrystallization at the core layer, and it is in agreement with EBSD results. The starting time of recrystallization is also marked by arrows in Figure 5-32 as approximate 2 hrs for the interface region and about 6 hrs for the core layer based on the EBSD maps shown in Figure 5-25. The hardness evolution data combined with the EBSD maps therefore indicates that significant hardness reduction occurs at both the

interface region and the core layer before the corresponding onset of recrystallization. It is well-known that recovery generally leads to a small hardness reduction [52], the large portion of reduction in hardness for the both layers is therefore suggested to be partly attributed to the precipitate coarsening before the initiation of recrystallization.

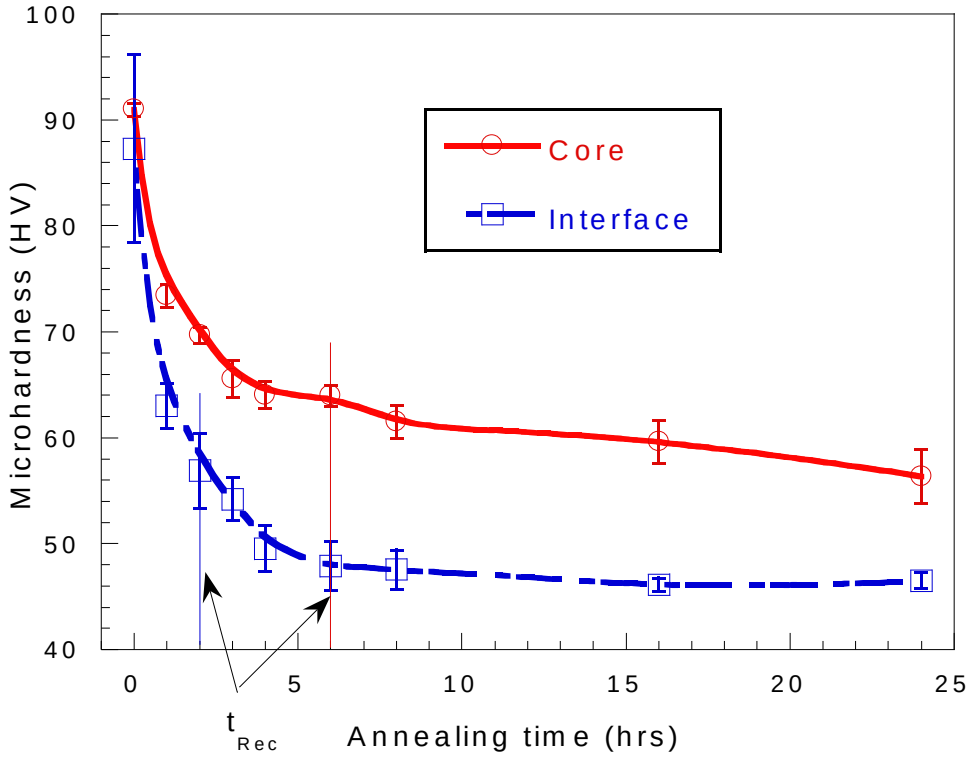


Figure 5-32. The hardness development of the 80% CR sheet with annealing time at 300°C.

### 5.3.4 **Grain boundary characterization**

The percentage of high angle boundary for a fully recrystallized microstructure was analyzed and is presented in Figure 5-33. It shows a similar evolution with annealing temperatures for both 60% and 80% CR samples: the higher temperature the larger percentage of high angle

boundaries. Meanwhile, the percentage of the higher angle boundaries is larger for the 80% CR sample than the 60% CR sample when annealed at a same temperature.

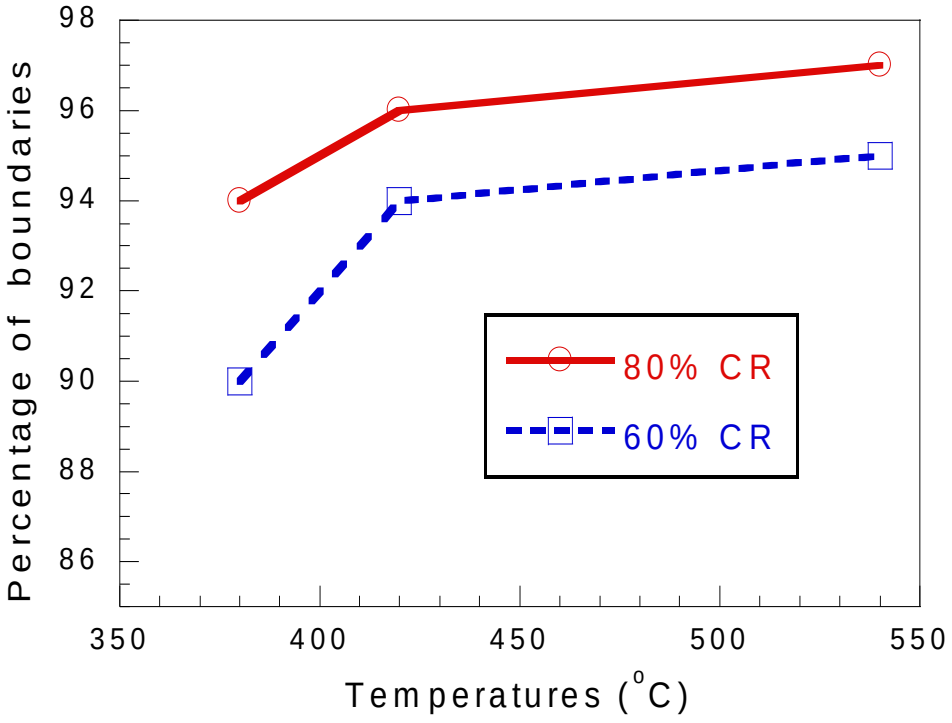


Figure 5-33. The percentage of high angle boundaries at different annealing conditions.

The distribution of high angle boundaries obtained together with EBSD maps is compared and given in Figure 5-34 for different levels of deformation. It is noticed that that a higher amount of boundaries with angle between 45° and 62.5° presents at the annealed 80% CR sample that has a higher level of thickness reduction.

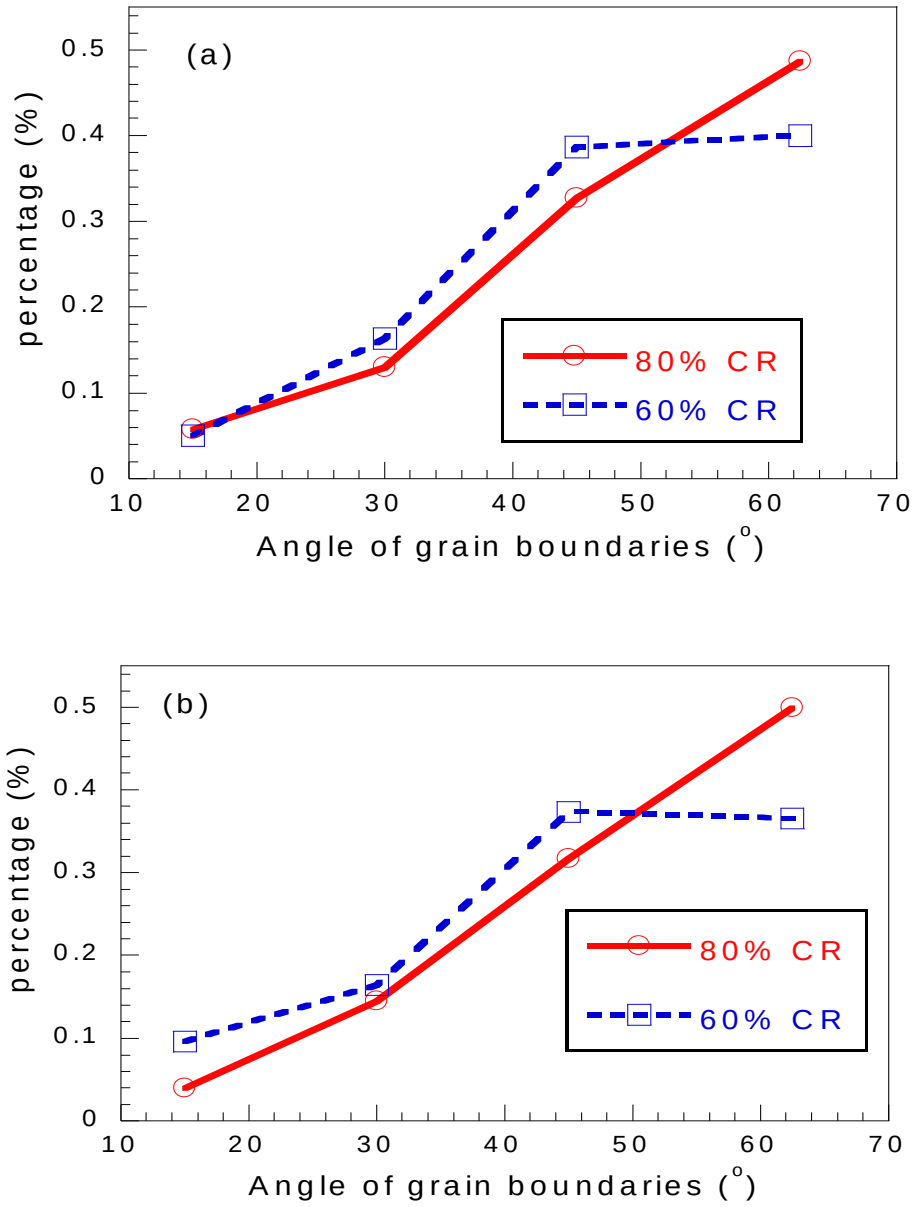


Figure 5-34. Grain boundary misorientation of the samples with two deformation levels and annealed at (a) 380°C and (b) 420°C.

### 5.3.5 **The role of large particles and grain boundaries in recrystallization**

*Large particles*

SEM images shown in Figure 5-35 display the formation of the recrystallized grains in the vicinity of various large particles in the 60% CR sheet annealed at 480$^{o}$C. Six recrystallized grains are observed to distribute along the edges of an elongated large particle (Figure 5-35 (a)) in the clad layer and a single recrystallized grain is observed in the vicinity of an elongated particle in the core layer (given in Figure 5-35 (b)).

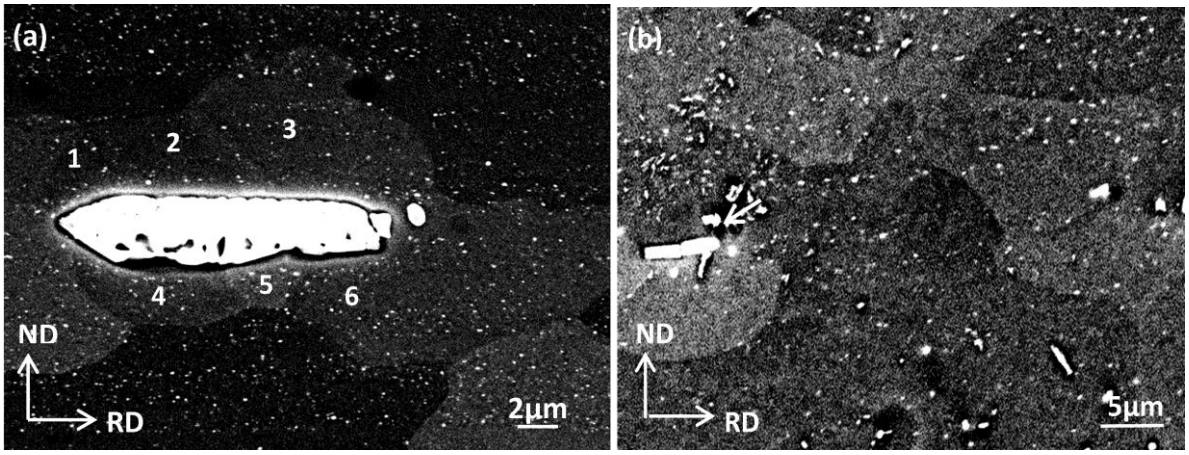


Figure 5-35. SEM images of recrystallized grains associated with various large particles for (a) the clad layer and (b) the core layer of the 60% CR sample annealed at 480$^{o}$C for 1 h.

Multiple recrystallized grains are also found around particles with a large size for an annealed 80% CR sheet as shown in Figure 5-36 (a); whereas a single recrystallized grain grown from small particles is given in Figure 5-36 (b) for the same sheet. The multiple recrystallized grains given in Figure 5-35 and Figure 5-36 demonstrates a straight boundary

between them. The growth of the recrystallized grains associated with large particles shown in Figure 5-36 is found to be limited by the small precipitates due to the fact of a high number density of precipitates aligned along the bowing boundaries.

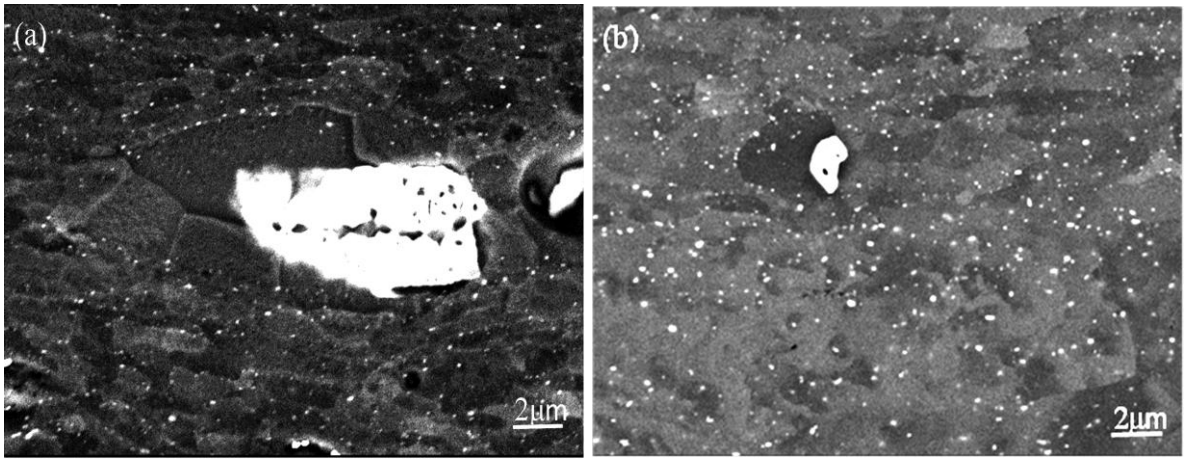


Figure 5-36. Recrystallized grains associated with large particles with various shapes in the 80% CR sample annealed at 300$^{o}$C for 24 h.

The early stage of the recrystallized grains associated with large particles is further studied for both the clad layer and core layer for the annealing condition of 300$^{o}$C for 10 mins, and the result is given in Figure 5-37. Recrystallized grains are also found around large particles in the clad layer as shown in Figure 5-37 (a) and (b); whereas, there is no sign of recrystallized grain around particles in the core layer as presented in Figure 5-37 (c).

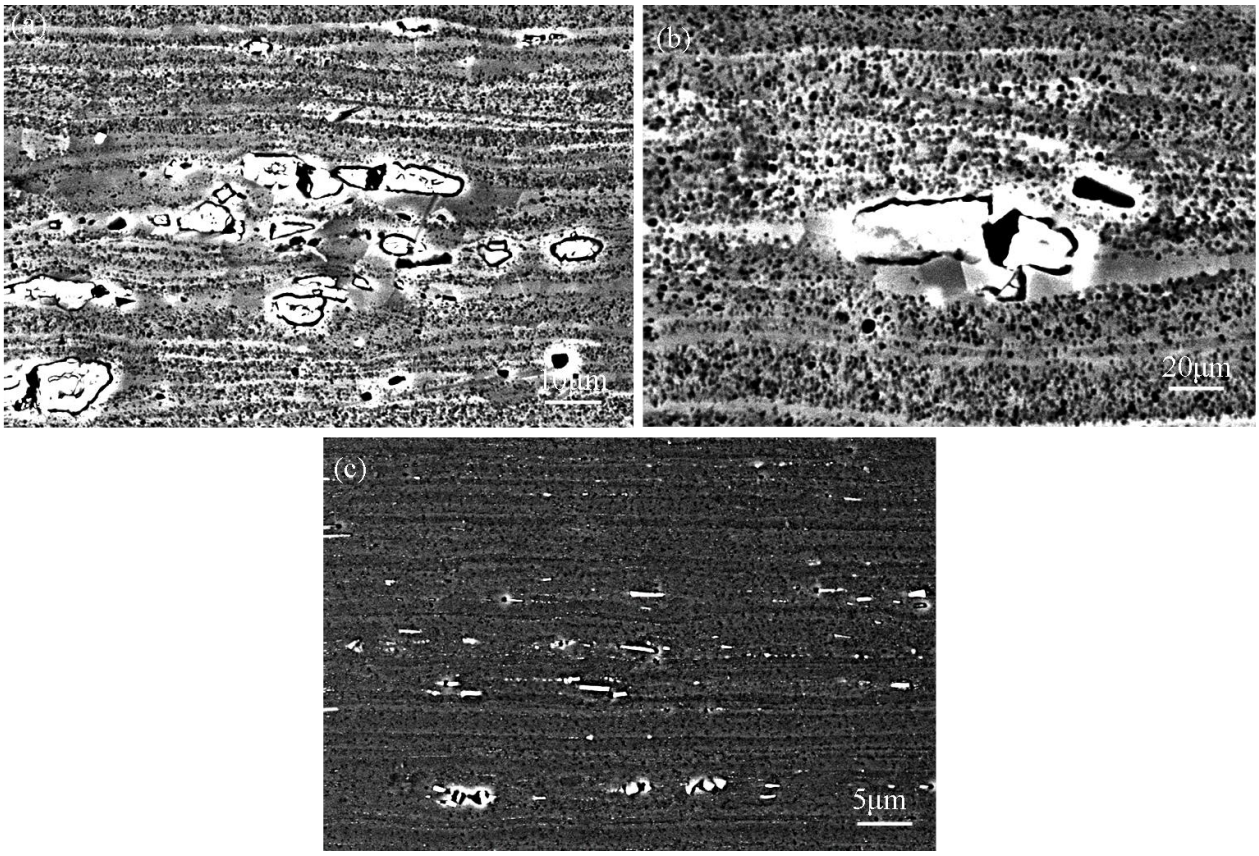


Figure 5-37. Recrystallization associated with large particles (a) and (b) at the clad layer and (c) at the core layer for the 80% CR sheet annealed at 380$^{o}$C for 10 mins.

*Grain boundaries*

In addition to the formation of large particles, recrystallized grains from grain boundaries are also observed in this system. Recrystallized grains are found around grain boundaries for all the layers of the annealed 60% CR sheet: the core layer, the interface region and the clad layer as given in Figure 5-38. A recrystallized grain is observed at a triple point of grain

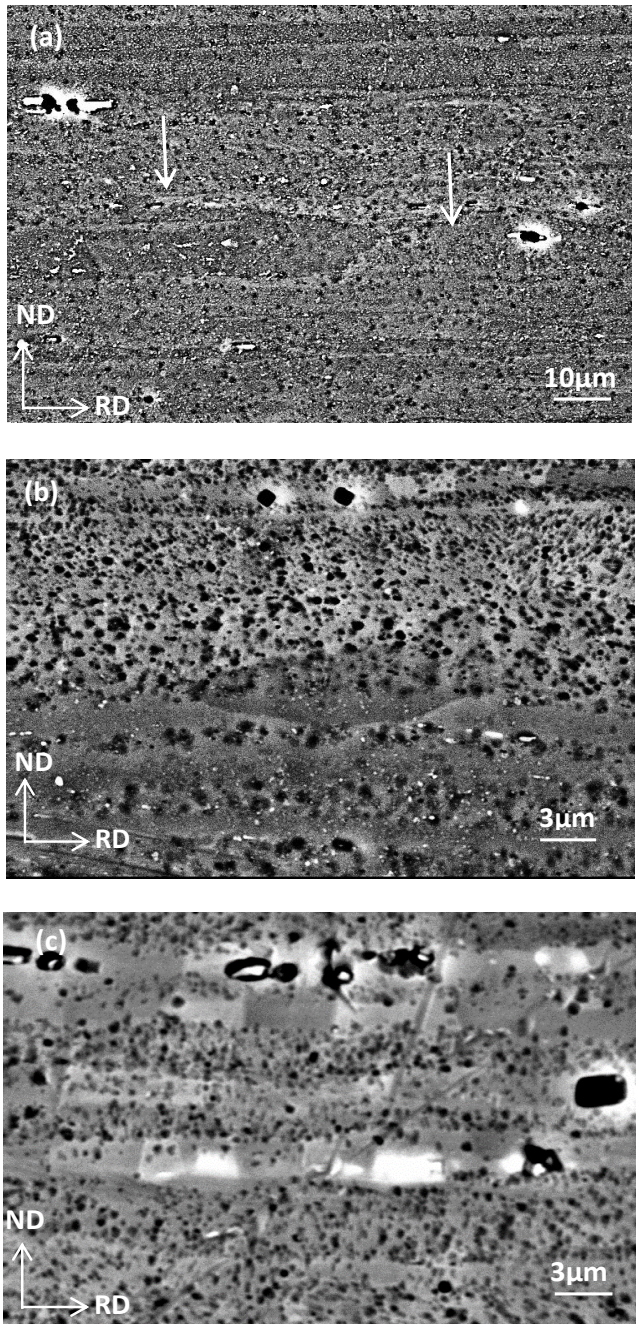


Figure 5-38. Microstructure of the 60% CR sample annealed for 10 mins at 380$^{o}$C for (a) the core layer, (b) the interface region, and (c) the clad layer.

boundaries at the core layer, whereas, a grain is found at an original higher angle boundary with migrating into both sides of the boundary at the interface region; the clad demonstrates a more significant evidence of recrystallization from grain boundaries with multiple grains growing in the same direction as shown in Figure 5-38 (c). The nucleation at the core and interface regions is a classical nucleation from grain boundaries which is one type of deformation heterogeneities; whereas, the characteristic of newly-formed recrystallized grains at the clad layer is in agreement with the fact of nucleation from grain boundaries. Nucleation from grain boundaries has also been reported as an active nucleation mechanism in Al-Mn alloys [52,61,87]. It is worthy to mention that this typical character cannot be observed with same sample preparation for the 80% CR sheet annealed at 380$^{o}$C.

## 5.4 Discussion

The starting conditions of the annealed samples, the potential precipitation reaction, and evolution of pre-existing particles during annealing is discussed first separately for the clad layer and core layer. The effect of temperatures and deformation levels on the recrystallized microstructure of the clad and core layers, the recrystallization behavior associated with the composition gradient of the interface, and the operative nucleation mechanisms are then discussed.

### 5.4.1 Fine particle distribution and potential precipitation

At high temperatures, heterogeneous precipitation nucleation is energetically favorable due to a small undercooling [106]. Dislocations being produced during the hot deformation of an

Al-Mg-Si-Cu alloy have been reported to form subgrains boundaries [169]. These boundaries are known as efficient sinks for solutes and providing short-circuiting diffusion paths through the dislocation lines [118]. Therefore, subgrain boundaries are favorable heterogeneous nucleation sites due to the solute segregation, as well as their low activation energy which is reduced by the misfit strain energy of the dislocations. A similar heterogeneous precipitation behavior has also been observed in a deformed Al-Mn alloy [64]. These heterogeneously distributed fine particles can limit or even hinder the formation of dislocation cells during the cold rolling if the inter-particle spacing is less than the dislocation cell size [52]. It is therefore believed that such a process has retarded the formation of cell structure, and thus generates the observed fine particle distribution at the core layer as given in Figure 5-9.

The volume fraction of fine particles formed during hot rolling is believed to be affected by the heat treatment history and composition of the matrix. The study on the precipitation behavior of the hot bands of AA6xxx series has demonstrated that a relative 66 to 87 vol.% of the precipitation occurred during hot rolling of AA6016, AA6061 and AA6111 alloys [170]. The area fraction and density of particles measured for AA3103 alloy in a hot rolled condition are also found to increase after annealing due to new precipitation [170]. The DSC analysis of the cold rolled material indicates the occurrence of precipitation reactions at all the layers during heating. It is therefore concluded that the precipitation reactions were not completed during the thermal-mechanical processing and before annealing. However, whether the precipitation reactions continue to take place during annealing depends on the

precipitation kinetics which is determined by both the temperature and the degree of supersaturation [52].

Chen et al. [118] have shown that the precipitation kinetics of AA3003 displays two nose temperatures, which are ~450$^{o}$C and 500$^{o}$C for an Al-0.48 wt.% Mn alloy within the strain range of 0.5 to 3.0. Liu and Morris [80] attributed the elongated coarse recrystallized grain structure of a supersaturated cold rolled Al-Mn alloy with a 60% thickness reduction (equivalent to a true strain of 0.9) to the occurrence of precipitation reactions during annealing. Moreover, the investigation on a supersaturated Al-Mn with a 90% thickness reduction showed that an equiaxed recrystallized grain structure formed at 482$^{o}$C which is high enough to allow the recrystallization to initiate first [65]. Last but not the least, the study of temperature-time-transformation diagram of cold rolled Al-Mn alloys with different deformation levels has showed that precipitation is accelerated by both the amount of Mn in the matrix and the deformation level [61]. Considering the clad layer in our study with a 60% thickness reduction (equivalent to a true strain of 0.91) and a composition of ~0.5 wt. % Mn, it is believed that the precipitation takes place before the recrystallization when the cold rolled sample is annealed at the investigated temperatures of 300$^{o}$C, 380$^{o}$C, 420$^{o}$C and 480$^{o}$C.

The calculated equilibrium volume fraction of $Mg_2Si$ and Q in AA6111 is reported to decrease dramatically at temperatures above 300$^{o}$C, and the total fraction of Q and $Mg_2Si$ reduces approximately from about 70% at 400$^{o}$C to 25% at 500$^{o}$C [33]. Regarding the large number density of the observed pre-existing particles, the precipitation reaction in the core

layer is negligible during annealing at the investigated temperature range (i.e. 380-540$^{o}$C) due to the small undercooling.

Kuijpers et al. have studied the formation of Al (Fe, Mn) Si in the Al-Mg-Si alloys with various elements, and the result shows that plate-like AlFeSi transform into globular Al (Fe, Mn) Si during homogenization at temperatures between 530$^{o}$C and 600$^{o}$C, and the transformed fraction increases with the content of Mn [171]. The particles as shown in Figure 5-23 are therefore AlFeSi and Al (Fe, Mn) Si. It is therefore reasonable to conclude that new particles and transformation between the two types of particles might take place during annealing at the solutionizing temperature.

### 5.4.2 **The effect of temperature on the recrystallized behavior**

*The effect of Zener drag pressure*

The growth rate (i.e., the movement of grain boundaries) in different directions of RD and TD determines the recrystallized grain structure at a certain temperature. The velocity of high angle boundaries $V$ depends on net driving pressure $P$. The varying growth rate can come from the retarding pressure including Zener drag pressure $P_Z$ and the drag pressure $P_S$ from solutes. The velocity and net driving pressure for the migration of high angle boundaries are determined as follows considering the effect of solutes [52,53]:

$$V = MP \qquad (5\text{-}2)$$

$$P = P_D - P_Z - P_S \qquad (5\text{-}3)$$

$$P_Z = \frac{3\gamma}{2} \cdot \frac{f}{r} \qquad (5\text{-}4)$$

Where $M$ is the mobility of grain boundaries; $P_D$ is the driving pressure from the stored energy; $f$ and $r$ are the volume fraction and averaged radius of the fine particles, respectively; and $\gamma$ denotes the grain boundary energy [52]. $P_s$ , which is proportional to the concentration of solutes in the matrix, is generally smaller than $P_Z$ [52]. It is noted that the magnitude of the Zener drag pressure depends on the nature of particles. The calculations of $P_Z$ demonstrates various formula; however, it is agreed that $P_Z$ is proportional to *f/r* [52,66].

Troeger et al. [86] investigated the effect of precipitate distributions generated through multistage annealing treatments on the recrystallized microstructure of a cold rolled Al-Mg-Si-Cu alloy with a 60% thickness reduction. It is found that precipitate first distributes preferentially along deformation bands after annealing at 300$^{o}$C for 4 hrs, whereas uniformly distributed precipitates were obtained after a continuous annealing treatment at 380$^{o}$C for 24 hours. The distribution of precipitates formed in the early stage of the annealing is therefore believed to be heterogeneous in the interface and core layers. TEM images on the studied cold rolled laminate sheet with a 60% thickness reduction also show that pre-existing particles of the core layer heterogeneously locate along the deformation bands. The pre-existing particles are therefore believed to distribute preferentially on subgrain boundaries in the core layer, which is then mainly responsible for the elongated recrystallized grain structure of the layer. The special distribution with a large portion of fine particles concentrated along deformation bands, shown in Figure 5-9, introduces different volume

fractions of particles at the directions along and perpendicular to the bands. A similar distribution of precipitates has also been observed in AA3xxx [64]. Therefore, as suggested by equation (5-4), the grain boundaries in the direction of or close to the deformation bands encounter a greater Zener drag pressure due to a larger value of *f/r* than the boundaries aligning perpendicular to the deformation bands. The elongated grain structure is therefore attributed to the large Zener drag pressure along the deformation bands than the other direction. Both the precipitates formed before recrystallization during annealing and the pre-existing fine particles formed during thermal-mechanical processing are therefore suggested to give rise to the elongated recrystallized grain structure for the laminated material.

*The temperature-dependence of the recrystallized grain structure*

The temperature-dependence of the aspect ratio of the recrystallized grains is suggested to be determined by grain boundary velocity that depends on both the mobility of grain boundaries and Zener drag pressure on the grain boundaries. The temperature-dependence of grain boundary mobility follows the equation (2-8) indicating the boundary mobility increases with the temperature [52].

The Zener drag pressure on the grain boundaries also varies with temperatures due to the different volume fractions of precipitates formed before recrystallization and to the size distribution. It is well known that, for a system with a certain composition, a lower driving pressure for precipitation is expected at a higher temperature, which therefore leads to a lower volume fraction of precipitates with a larger average size. The corresponding Zener

drag pressure at a higher temperature decreases due to a lower *f* and a larger *r*. It is generally concluded that grain boundary velocity is larger at higher temperature due to the increasing mobility and the decreasing Zener drag pressure. The large mobility of grain boundary at high temperatures gains the ability to overcome the Zener drag pressure, which offsets the effect of Zener drag pressures in RD and ND. The increasing mobility of the grain boundaries helps to reduce the anisotropic growth of the recrystallized grains. In the extreme case the mobility is high enough to overcome the Zener drag pressure, and an equiaxed grain structure is then expected. Assuming that grain boundary mobility in RD and ND is the same, the Zener drag pressure is then suggested to be the main reason for the different increasing rate of the aspect ratio.

For the clad, the aspect ratio shows a great increment with the temperature until 420$^{o}$C, followed by a slight increase at 480$^{o}$C as suggested in Figure 5-21. The increasing rate of the aspect ratio with the temperatures is believed to relate to the precipitation characteristic that is determined by the temperature-depended driving pressure for precipitation. The smaller increase of the aspect ratio beyond 420$^{o}$C can then be attributed to the great reduction in driving pressure a d volume fraction of precipitates. At 540$^{o}$C, recrystallization of the clad layer therefore might take place before the precipitation, which explains the corresponding equiaxed grain structure.

For the core layer there is no precipitation reaction during annealing at the studied temperature range, and the extent of dissolution of the pre-existing fine particles at different annealing temperatures plays an important role in growth of the recrystallized grains. Based

on the calculated equilibrium phase diagram of the core layer [90], dissolution of fine particles is not expected at 380$^{o}$C, and a certain fraction of these particles dissolve at 420$^{o}$C and 480$^{o}$C. All the fine particles, including $Mg_2Si$, Si and Q, are expected to dissolve completely at 540$^{o}$C. The increasing hardness after annealing for 1 h at temperatures higher than 400$^{o}$C as shown in Figure 5-13 indicates the increased level of solutes from the dissolution of particles. A larger size and a smaller volume fraction of fine particles are expected at temperatures higher than 380$^{o}$C due to the dissolution. The lower $P_Z$ reduces the difference of the pinning pressure on boundaries between RD and ND, indicating the aspect ratio of the recrystallized grains decreases. The dissolution modeling of the laminated system at 540$^{o}$C has shown that $Mg_2Si$ and Si dissolve in 20 s [90]. However, the elongated recrystallized grain structure of the core layer at this temperature indicates that the recrystallization process is still retarded to some extent by a fraction of fine particles.

In addition to the velocity of the recrystallized grain boundaries, the nucleation rate of the recrystallized grains can also affect the aspect ratio. The nucleation rate of the recrystallized grains increases with temperatures. A higher nucleation rate generates a larger density of grains, and the impingement of grains alleviates the anisotropic growth. The smallest aspect ratio for 540$^{o}$C is also attributed to the dominated high nucleation rate. Therefore, it is concluded that the increasing mobility of grain boundaries, the higher nucleation rate, and the smaller fraction of precipitates with a large average size facilitate the reduction of the aspect ratio at a higher temperature.

### 5.4.3 **The effect of percentage of the cold work on the recrystallization behavior**

It is well known that deformation levels and temperatures accelerate both the recrystallization and precipitation processes [52]. A combination of a deformation level and a certain temperature can leads to a case that recrystallization takes place before precipitation, and the related recrystallized grain structure is then equiaxed instead of being elongated due to inefficient pinning of precipitates on the grain boundaries [64,65]. Compared with the temperature-dependence of the recrystallized grain structures with different thickness reductions as given in Figure 5-21 and Figure 5-22, it is concluded that a near equiaxed recrystallized grain structure of the clad layer was obtained at 540$^{o}$C for 60% CR sheet, and 420$^{o}$C for 80% CR sheet, respectively. The study on the temperature-dependence of the recrystallized grain structure of the annealed 60% CR sheet suggest that the precipitation preceding the recrystallization during the annealing is the main reason for the elongated recrystallized grains, indicating the recrystallization starts earlier than precipitation at 540$^{o}$C. The critical temperature for an equiaxed recrystallized grain structure in the clad layer is found at 420$^{o}$C for the annealed 80% CR sheet, and at 540$^{o}$C for the annealed 80% CR sheet as shown in Figure 5-15 and Figure 5-19. It is therefore concluded that a higher level of deformation decreases the temperature range at which the recrystallization kinetics dominates, and recrystallization takes place without the retarding pressure from precipitation.

It is generally accepted that the extent of the inhomogeneity of the deformed structure and the fraction of high angle boundaries increase with the strain for Al alloys at an intermediate

strain range [125]. It is then expected that the density of nucleation sites is higher for the 80% CR sheet than for the 60% CR sheet since recrystallization nucleation takes place preferentially at heterogeneities where a large misorientations exist. A smaller recrystallized grain size is therefore expected at a higher deformation level due to a higher density of nucleation sites. In addition to the recrystallization nucleation, the migration of high angle boundaries is another factor that determines the recrystallized grain structure and size. A high level of deformation generates a higher driving pressure $P_D$, which facilitates the grain boundaries escape from the Zener pinning pressure from the precipitates with small sizes suggested by equation (5-4). The increasing nucleation rate and higher velocity of the grain boundaries is therefore suggested to lead to the recrystallized grain structure with a low aspect ratio for the 80% CR sheet.

### 5.4.4 **The effect of composition gradient on the recrystallization behavior**

Considering the mass balance aspects of precipitation (i.e. the lever rule [105]) from a metastable solid solution, a low volume fraction of precipitates is obtained when the alloy contains a low level of solutes that take part in the precipitation processes. In the current system, the interface region is lean in solute elements Mg, Si, and Cu, while the core is rich in these elements. These compositional characteristics of the cold rolled material are measured using the EPMA on the 60% and 80% CR sheets, as well as the EPMA results from the hot rolled plate samples of the current system [90]. As in other Al-Mg-Si-Cu alloys [142,144,172], Mg, Si, and Cu participate in the formation of precipitates in the core layer

and the core-clad interfacial region during the annealing process. However, the volume fraction of the precipitates should be proportional to the content of solutes that participates in the precipitation process. A lower volume fraction of precipitates leads to a less effective Zener drag and thus a faster recrystallization during annealing. This general understanding is in agreement with the layer-specific onset and progress of recrystallization identified by the EBSD test results, indicating the scaling of recrystallization kinetics with solute/precipitate fraction. The significant drop in the hardness values prior to recrystallization, as shown in Figure 5-32, further suggest that precipitate coarsening in both interface and core interior play a significant role in reducing the Zener drag and thus help with the initiation (i.e. the mobility of low angle grain boundaries) and progress of recrystallization.

The EBSD maps and the corresponding EMPA profile for the 80% CR sheet annealed at 300$^{o}$C indicates the concurrent precipitation and/or coarsening of precipitates during annealing. The similar trend of Mg and Cu may suggest the formation of AlSiMgCu as predicted by the phase calculation [90]. The zigzag distribution of Si also indicates another possible precipitation and coarsening of Si, which is reported to be one potential precipitate at 300$^{o}$C in the system [90]. The recrystallization initiates from the place containing a high content of Si as given in Figure 5-12 (b), and develops into the area where a significantly uneven distribution of Si is observed as shown in Figure 5-30. It is therefore concluded that recrystallization of the interface and core layers takes place with the process of the precipitation and coarsening of Si, which is also supported by Figure 5-23 (a) and (b)

showing that a higher number density of coarser particles after annealing for 6 hrs at the recrystallized interface region .

By comparing the hardness profile of the hot rolled material as shown in Figure 5-10 and cold rolled material as given in Figure 5-12, it is noted that the hardness of the clad layer, the interface region, and the core layer increases after cold rolling; however, the hardness of the interface demonstrates the greatest increase, which indicates the largest strain hardening and the highest driving pressure for recrystallization among the studied three layers. The largest strain hardening of the interface region is suggested to be mainly attributed to the interaction between dislocation and particles including both coarse particles and fine particles during cold rolling. The highest hardness at the core layer of the interface side might also be caused by the internal stress due to non-uniformed deformation, which is also reported at the laminated AA5005/AA6061 processed by accumulative roll bonding [5]. The larger value of hardness at the interface region therefore is one reason for an earlier initiation of recrystallization due to a higher driving pressure.

On the clad side of the interface region, a higher number density of coarse Al (Fe, Mn) is observed, and the number density decreases with the distance towards the core layer shown in Figure 5-2. Clusters of the small coarse particles are observed mostly at the interface region. Like the clad layer, the precipitation might take place during annealing due to the presence of a certain level of free Mn. There are two possible precipitates of Al (Fe, Mn) and Al (Fe, Mn) Si, and the formation of Al (Fe, Mn) Si might be accelerated due to the enrichment of Si from the dissolution of $Mg_2Si$ and Si. Due to the high content of Mn, the

amount of the Al (Fe,Mn)Si and Al(Fe, Mn) including both the pre-existing and newly formed during annealing in the clad side of the interface region is more than that in the core side of the interface. The Zener drag effect of these fine particles containing Mn in the interface retards the growth of the recrystallized grains. The high number density of both coarse and fine particles containing Mn or Mn and Si facilitates the refinement of the recrystallized grains of the interface region.

### 5.4.5 **Operative nucleation mechanisms**

The possible potential recrystallization nucleation sites are large particles (PSN) and prior grain boundaries in the studied system. Nucleation from grain boundaries has been reported as an active nucleation mechanism, and the process is usually referred to as strain-induced boundary migration (SIBM) including multiple subgrain and single subgrain [52,61,131,132,173], or to the classical nucleation from grain boundaries for Al alloys.

*PSN mechanism*

The correlation between large particles and recrystallized grains as given in Figure 5-36 and Figure 5-37 indicates an effective PSN mechanism. To further discuss the nucleation mechanism, indexed quality maps (IQ) and SEM images obtained before EBSD scanning and in the same areas of the related EBSD maps are compared in Figure 5-39 and Figure 5-40 for

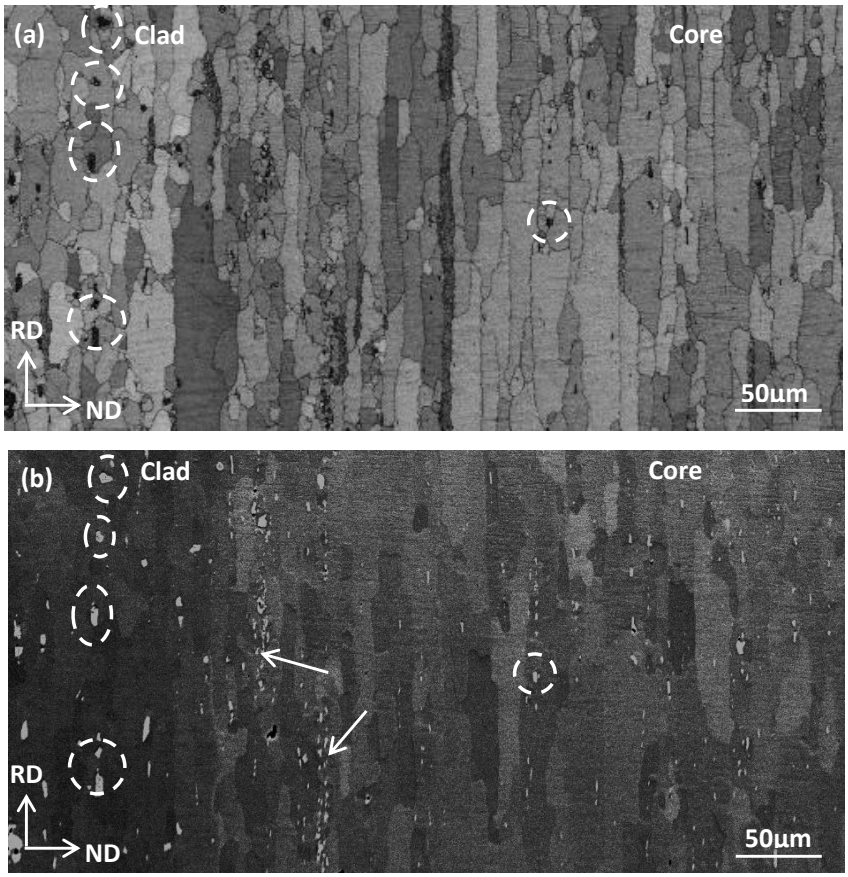


Figure 5-39. (a) IQ map obtained from EBSD data and (b) the corresponding SEM image for the 60% CR sample annealed at 380$^{o}$C for 1 h.

two different annealing conditions for the 60% CR sheet. The IQ map gives the diffraction pattern quality by various gray scales, and can be used to distinguish the coarse particles from the background, as well as the grain boundaries. Multiple small equiaxed grains are observed to be associated with large coarse particles in the clad by comparing the IQ map and the corresponding SEM image at the same area, and typical examples are shown with circles. The areas containing a high density of smaller coarse particles (i.e. particle clusters), indicated with arrows in Figure 5-39 and Figure 5-40, also show a smaller recrystallized

grain size than the area without particle clusters. The presence of a very large coarse particles and a large fraction of fine recrystallized grains in clad layer demonstrates an efficient operative PSN as shown in Figure 5-39 and Figure 5-40.

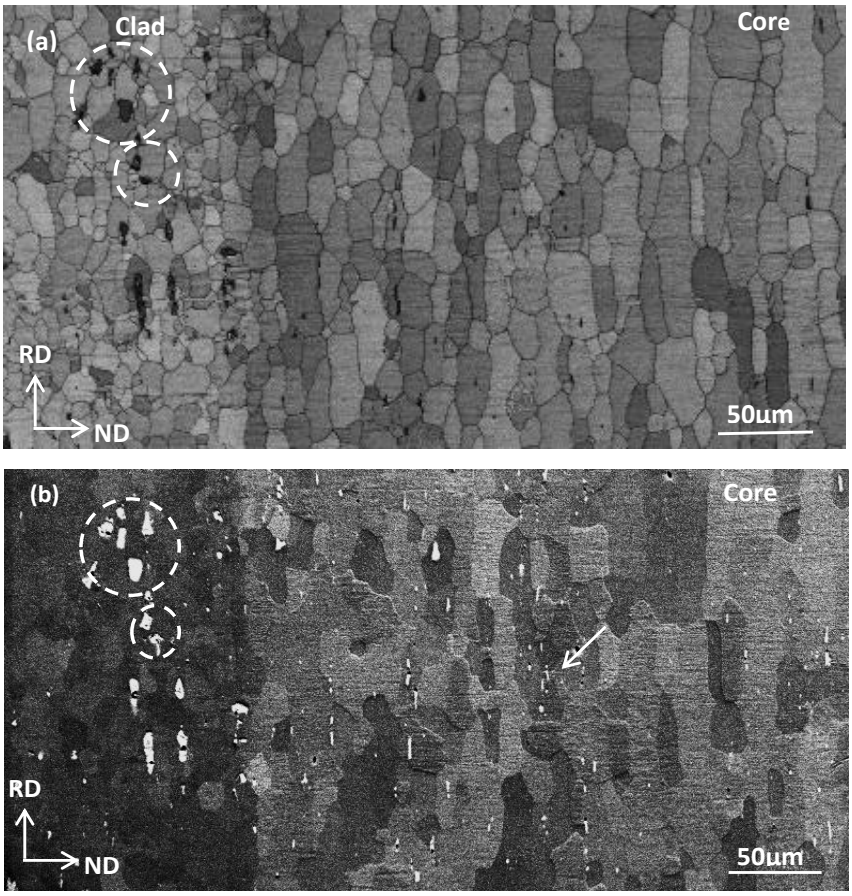


Figure 5-40. (a) IQ map obtained from EBSD data and (b) the corresponding SEM image for the 60% CR sample annealed at 540$^{o}$C for 30 seconds.

The nature of PFZ and defamation zones and the level of deformation are the factors which determine the occurrence and efficiency of PSN. PFZs are often found around the constituent particles in Al-Mn alloys, and it has been suggested that the depletion of Mn around the

constituent particles is responsible for the formation of PFZs [111]. PFZs have also been observed around large β particles nucleated at Al(Fe, Si) particles in a cold rolled Al-Mg-Si alloy [86,87]. The depletion of solutes around large particles is then believed to facilitate the formation of PFZs around coarse particles shown in Figure 5-3. PFZs improve the efficiency of recrystallization nucleation around large particles by allowing the nuclei associated with them to grow free or with a reduced pinning pressure from the fine particles inside these areas [52]. With the existence of PFZs, the opportunity for nuclei to reach the critical size is increased, and the efficiency of PSN thus is improved as well.

As can be seen in Figure 5-35 (a) and Figure 5-36 (a), multiple recrystallized grains nucleated from a large constituent particle, are elongated along RD, and grow in different directions during annealing. This is supported by Tangen et al.'s study [64] on the recrystallization of an Al-Mn alloy, showing that the elongated particles are efficient PSN sites for nucleation of multiple recrystallized grains. Furthermore, needle-shaped dispersoids containing Mn are reported to be more likely to be nucleation sites than fine spherical particles [141]. It is therefore concluded that the size of the large particles in RD and ND play a role in the occurrence and efficiency of PSN. The size and shape of the deformation zones are found to scale with the size of the associated particles, as well as varying with their shape [52]. The deformation zones associated with the elongated large particles, which are observed to be elliptical in the rolling direction (as shown in Figure 5-6), are well-known to be preferential nucleation sites for the recrystallization by providing the nucleation driving pressure and large misorientaion gradients during annealing [52]. The largest lattice

misorientation is found to be at the interface of the particles, and is a function of the size of the associated particles [52,174]. Liu et al. [154] revealed that the largest lattice rotation occurs near the four tips of the elongated particles. This rotation can possibly divide the large deformation zone into multiple individual parts where nuclei can form and grow. The modeling of the strain fields around non-deformable particles by means of the finite element method has shown that a combination of compressive, tensile and shear strain exists in all ND, RD, and RD-ND directions [175]. In the case of the elongated particles, due to a small size in ND, the corresponding shear strain might not be large enough to create the lattice rotation required for nucleation of a recrystallized grain. This explains why only one recrystallized grain is observed around an elongated particle with a size in ND less than 1 μm, as shown in Figure 5-35 (b). It is therefore proposed that the PSN is most efficient around the large elongated coarse particles. The efficiency is enhanced by a larger particle size in ND.

In addition to the PFZs and deformation zones, the occurrence and efficiency of PSN are affected by deformation levels and annealing temperature. A higher driving pressure indicated by a higher level of strain leads to a smaller critical size of particles, which explains the efficiency of PSN at the interface region containing particle clusters and high driving pressure. PSN is also observed to be effective for an 80% CR sheet annealed at 300$^{o}$C for 24 h as given in Figure 5-36; however, PSN cannot be observed at early stage of annealing at 380$^{o}$C. It is interesting to find that PSN initiates at an early stage of annealing at 380$^{o}$C for the 60% CR sheet and the initiation of recrystallization first occurs around large particles at

the clad layer as presented in Figure 5-37. It is therefore concluded that PSN is retarded significantly by the concurrent precipitation as shown in Figure 5-36. It indicates that the slow migration of grain boundaries at a low annealing temperature can be a major factor for the occurrence of PSN.

*Nucleation from grain boundaries*

The grain boundary is also found to be another nucleation site with strong evidence characterized and given in Figure 5-38; however, the characteristics of the grain boundaries are varied at different layers. Multiple recrystallized grains are found to nucleate from the same grain boundary aligning along RD, and grow in RD at the clad layer. The grains at the early stage of recrystallization migrate at a same direction and form a band structure, which indicates a typical SIBM character [61]. EBSD maps of the recrystallized grains as shown in Figure 5-17 has shown that low angle boundaries do exist in some recrystallized grains, which suggests that a SIBM nucleation limited by precipitates might be operative nucleation mechanism in the clad layer.

The recrystallized grains at the core layer and interface region of the 60% CR sheet annealed for 10 mins at 380$^{o}$C demonstrates a classical nucleation from the grain boundaries, and the boundaries surrounding the grains can migrate in two opposite directions as given in Figure 5-38 (a) and (b). It is in accord with the studied result of a cold rolled pure Al. Jones and coworkers [176] have observed and developed a related model that a nucleus formed around grain boundaries, and migrated into parent grains from both sides of the grain boundaries.

Recrystallized nuclei have also been found in copper alloys and to straddle the original high angle boundary [134]. A typical recrystallized grain, observed in interface region of the 80% CR sheet annealed for 6 hrs is shown in Figure 5-41. It is clear that assuming a nucleus forms at the grain boundary, the migration of the high angle boundary of the nucleus can grow into both sides of the boundaries.

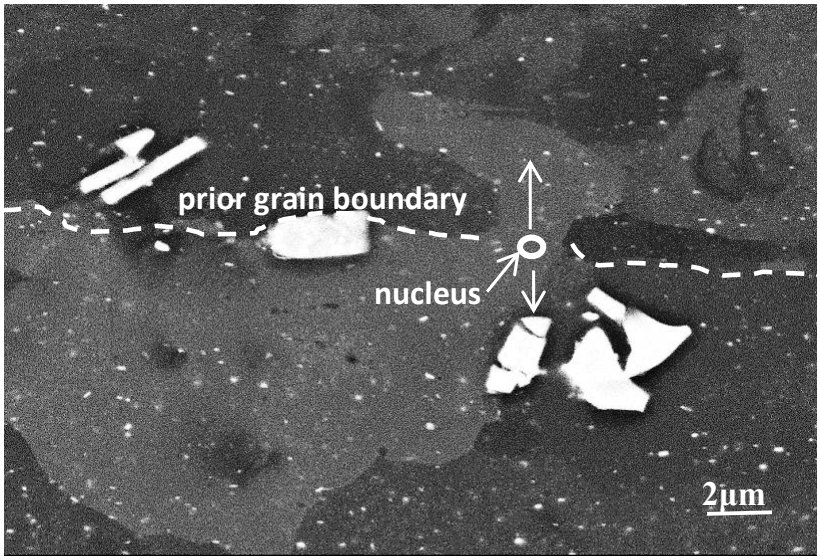


Figure 5-41. A typical recrystallized grain along a prior grain boundary.

The difference between strain introduced boundary migration (SIBM) and nucleation from pre-existing boundaries is not very clear on the current knowledge. They both originate from the high angle boundaries. However, in the case of SIBM, a recrystallized grain forms by the bulging of the prior high angle boundaries instead of nuclei-forming, and the driving pressure is from the difference of dislocation density on the two sides of the boundaries. The nucleation characteristic of the recrystallized grains from both mechanisms is modified by

fine particles. The recrystallized grains formed between 2 and 4 hrs at the interface region of the 80% CR sheet annealed at 300$^{o}$C as given in Figure 5-42 (a), demonstrates an elongated shape with a large fraction of straighten boundaries aligning in RD. Both boundaries in ND and RD migrate by segments as shown in Figure 5-42 (b) and (c) due to the pinning of fine particles. The growth front of the boundaries is also divided into segments bulging at various speeds, which generates curved and serrated boundaries. A large elongated grain illustrated in Figure 5-42 (d) is shown to surround two small grains, and the two long boundaries in RD demonstrates the migration towards opposite directions.

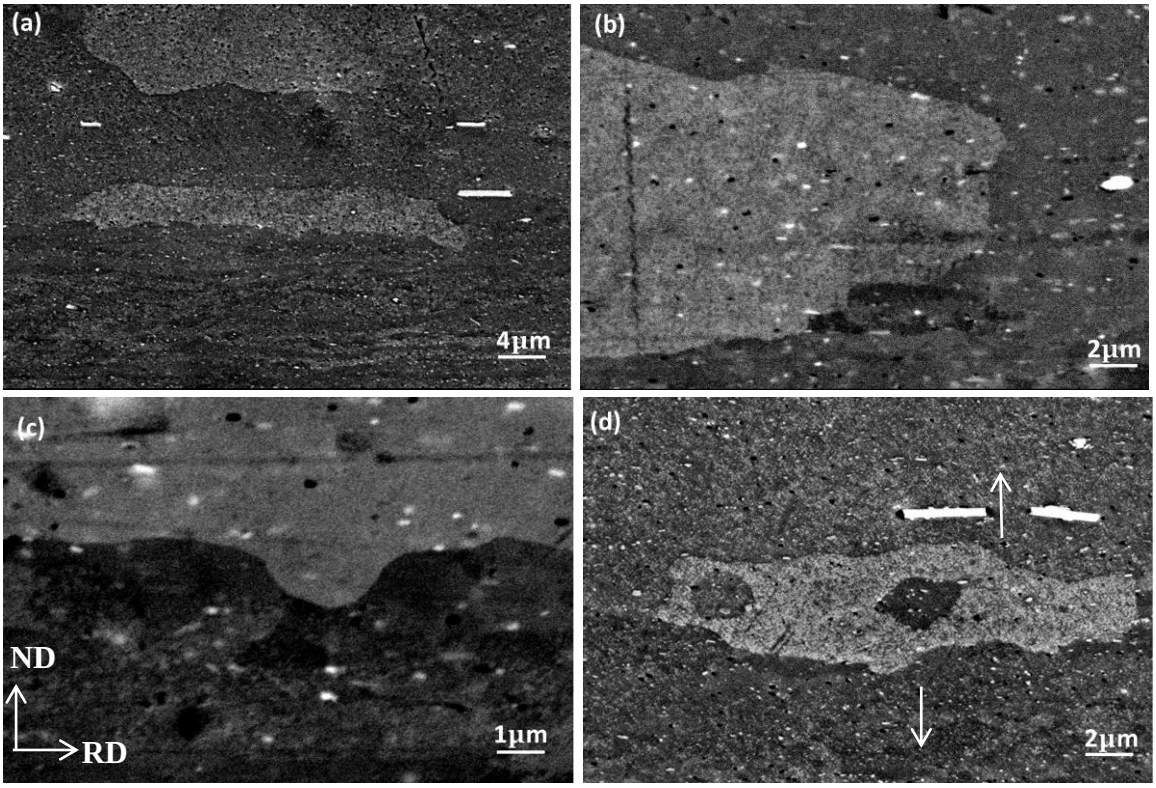


Figure 5-42. The development of recrystallized grains unassociated with large particles for the 80% CR sheet annealed at 300$^{o}$C for 2 hrs.

Based on the above discussion on nucleation from grain boundaries, a nucleation model considering the effect of fine particles can be proposed. The deformed microstructure is believed to comprise mostly high angle boundaries parallel to RD, and mostly low angle boundaries in ND. During annealing, the prior high angle boundary is one of the potential sites for nucleation of recrystallized grains, and their growth is retarded by fine particles. A schematic representation given in Figure 5-43 can then be developed to display the formation of a nucleus around a high angle boundary, and its growth into two sides of the boundaries with pinning from fine particles. In this model, boundaries of the nuclei can migrated into neighboring parent grains. During growth, the boundary parallel to ND experiences a Zener drag pressure, which leads to a slow moving speed and multiple segments of boundaries since the whole length of the boundary is difficult to move together. However, the boundary of the nucleus can migrate faster in RD than in ND, and this nucleation and growth constrained by fine particles finally leads to elongated recrystallized grain structure without or with little misorientation inside them.

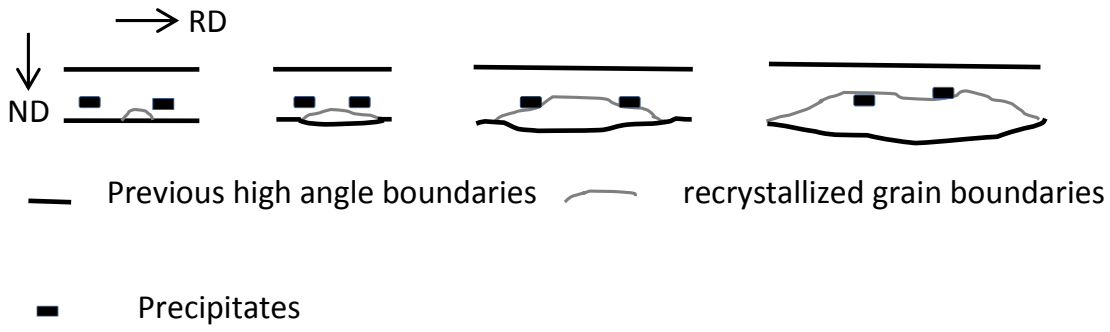


Figure 5-43. Schematic representation of nucleation from high angle boundaries with a dispersion of precipitates.

## 5.5 Summary

Recrystallization behavior of the laminated AA3xxx-X609 system is studied under various annealing temperatures and deformation levels, and it is concluded that:

The clad layer displays larger coarse particles along RD, while smaller ones are found in the core layer. In addition to the coarse particles, fine submicron-sized particles are also present in all the layers of the starting material. However, the DSC results have shown that the starting cold rolled laminated material still has precipitation ability.

The recrystallized grain structure of the laminated sheet is elongated at low annealing temperatures. Precipitates formed either during thermal-mechanical process or before recrystallization and during annealing, are proposed to be the main cause of the elongated recrystallized grain structure due to their preferential distribution along the original grain boundaries. The temperature-dependence of the aspect ratio of the recrystallized grains is found to be affected by both the annealing temperatures and deformation levels. The precipitation kinetics, coarsening/dissolution rates determined by both temperatures and deformation levels determine the recrystallized grain shape due to the different retarding pressure on the migration of recrystallized grain boundaries in RD and ND.

Annealing at the solutionizing temperature, the clad layer displays an equiaxed grain structure; whereas, the recrystallized grains of the core layer are still slightly elongated. Undissoved dispersiods and transformation of different dispersiods might be one of the reasons for the slightly elongated recrystallized grain structure. A higher level of deformation

decreases the temperature where a near equiaxed recrystallized grain structure is obtained for the clad layer due to a larger nucleation rate and the higher velocity of grain boundaries. A recrystallized microstructure with a higher portion of high angle boundaries is found to be obtained under a higher level of deformation.

The recrystallization of the laminated sheet is delayed due to the precipitation during annealing at a low temperature of 300$^{o}$C. Recrystallization is found to first initiate from the clad side of the interface where a composition gradient of Mg, Si and Cu starts. The earliest onset of recrystallization in the interface region is attributed to the lower Zener drag pressure due to the smaller volume fraction of precipitates and the faster coarsening of the precipitates, compared to the core layer. The higher level of accumulative deformation is also one reason for the earliest initiation of the recrystallization at the interface region. With the increasing time at 300$^{o}$C, the recrystallization progresses along the composition gradient into the core layer with the precipitation and coarsening of precipitates. The clad layer displays the slowest recrystallization, and the precipitation associated with Mn is suggested to retard extremely the recrystallization progress of the clad layer.

Particle stimulated nucleation and nucleation from grain boundaries are suggested to be the possible operative nucleation mechanisms in the recrystallization of the laminated system. With deformation zones and PFZs around them, the elongated coarse particles are effective in providing multiple nucleation sites, and the efficiency of PSN is found to increase with the size of the coarse particles in ND. The occurrence of PSN is also found to be retarded by the precipitation concurrent with annealing. Both typical characteristics of SIBM for the clad

layer and the evidence of classic nucleation from grain boundaries for the interface and core layers are found at the early stage of annealing.

# Chapter 6 Conclusions, and Recommendations for future work

The precipitation behavior of the interface and core layers and the annealing behavior of the whole laminated sheet have been investigated. The significant precipitation and annealing behavior associated with the compositional gradient of the interface region has also been studied. The following chapter summarizes the main findings of the research, and offers recommendations for future work.

## 6.1 Conclusions

- TEM reveals that the precipitates in the core layer are needle-shaped β″, for the aging condition of 180°C for 1 h. The precipitates in the interface region (0.3 mm from the clad surface) are found in a lower number density than in the core layer, but with a larger size. The different precipitate distributions in the interface and core layers are attributed to the composition-related precipitation kinetics including both nucleation rate and growth rate.
- The hardness in the interface region shows gradual increase with the distance from the clad surface and corresponds to the solute profiles of Mg, Si and Cu. On the clad side, a steeper increase of hardness is observed than on the core side. Hardness evolution with aging time at the investigated temperatures between 160$^{o}$C and 210$^{o}$C demonstrates a faster precipitation rate for a higher aging temperature.

- The precipitation kinetics is calculated using JMAK model based on the heat flow during aging. A precipitation-hardening model, designed for monolithic AA6xxx alloys, is employed for the laminated sheet through a mass correction, and the modeling result is in agreement with the calculated yield strength from hardness.
- The recrystallized grain structure of the AA3003-X609 laminate is affected by the distribution of the pre-existing particles, including both the large and small ones formed during thermal-mechanical processing, and the precipitation concurrent with recrystallization during annealing. The pre-existing particles affect both the cold rolled condition and annealing behavior. Deformation zones are found around large particles. Small particles are also found to interact with dislocation alignment and cell formation during deformation, and to distribute along deformation bands. Zener pinning pressure of the small particles limits the migration of grain boundaries during growth of the recrystallized grains.
- The recrystallized grain structure of the laminated sheet is elongated at low annealing temperatures. The preferential distribution of fine particles formed during either hot rolling or during annealing and before recrystallization is believed to be the main reason for the elongated grain structure of the bulk laminate. With increased annealing temperatures, the aspect ratio of the recrystallized grains decreases significantly. The preferential distribution of fine particles along the grain boundaries leads to a larger Zener drag pressure in RD than in ND. During annealing at different temperatures, precipitation/dissolution of particles can also change the volume

fraction and size of fine particles. In this case, the Zener drag pressure varies with the parameter of particles, including the size and volume fraction, and determines the temperature-dependence of the aspect ratio of the recrystallized grains.

- A higher level of deformation decreases the temperature where a near-equiaxed recrystallized grain structure of the laminate can be obtained, due to a larger nucleation rate and a higher grain boundary velocity resulting from a higher driving pressure. In the case that the driving pressure is high enough to overcome the Zener drag pressure, an equiaxed recrystallized grain structure is obtained. The fraction of high angle grain boundaries is also found to be larger for a higher level of deformation.

- The interface region, which contains both solute gradients and various particle distributions, demonstrates an increasing hardness from the clad towards the core layer. The highest hardness is observed at the interface region with the highest strain hardening after an 80% thickness reduction. The earliest onset of recrystallization is found at the interface region of the 80% CR sheet annealed at $300^{o}$C. The earliest onset is attributed to the higher driving pressure, and to the lower Zener drag pressure due to the smaller fraction of precipitates, compared to the core layer.

- Large particles and original grain boundaries are observed to be nucleation sites for recrystallization in the studied system. With deformation zones and PFZs around the larger particles, the elongated large particles are effective in providing multiple

nucleation sites. The efficiency of PSN is enhanced by the size of the coarse particles along the ND, and limited by the precipitation during annealing. Nucleation from grain boundaries is suggested to be another operative nucleation mechanism with typical evidence for SIBM and classical features of recrystallized grains associated with grain boundaries.

## 6.2 Recommendations for Future work

### 6.2.1 Interface modeling

The findings of the current study have shown that the precipitate distribution at a representative location of the interface region varies from the core layer, which indicates a composition-related precipitation behavior. A model for precipitation hardening of the interface region is essential for a comprehensive understanding of the precipitation behavior associated with compositional gradients. It is recommended that the relationship between precipitation kinetics and compositional gradients be developed in order to model the yield strength of the interface region.

### 6.2.2 The effect of pre-existing particle distribution on the deformed structure

The current study has shown that the pre-existing particles have a significant effect on the initiation of recrystallization and the recrystallized microstructure. It should also be noted that the shape and interfacial energy of the precipitates of AA6xxx are different at various aging conditions. It is therefore essential to study the effect of pre-existing particles, including the types and sizes of precipitates (β″, β′, $Mg_2Si$, and Q), on the deformed and

recrystallized structure for AA6xxx. By studying these effects, a proper thermal-mechanical process can be designed to obtain an optimal combination of mechanical properties.

### 6.2.3 **Precipitation at the deformed interface region**

Precipitation at the interface has been studied in the aged condition, and the results have shown different precipitation kinetics from the core layer, due to the existence of the compositional gradient present at the interface. The interface has also been observed to recrystallize earlier during annealing at 300$^{o}$C, which indicates a significant effect of precipitation. The effect of deformation on the precipitation behavior has been the subject of many studies; however, the effect becomes more complex with compositional gradients, and needs further investigation. In order to increase the understanding of the interface, it is therefore recommended to study the precipitation kinetics of the deformed interface, containing compositional gradient. Conducting a solutionizing treatment before cold rolling and followed by an annealing at a low temperature is suggested for this purpose.

## References


[1] A. Heinz, A. Haszler, C. Keidel, S. Moldenhauer, R. Benedictus, W.S. Miller, Mater. Sci. Eng. A 280 (2000) 102.

[2] W.S. Miller, L. Zhuang, J. Bottema, A.J. Wittebrood, P. De Smet, A. Haszler, A. Vieregge, Mater. Sci. Eng. A 280 (2000) 37.

[3] D.J. Lloyd, Mater. Sci. Forum 28 (2004) 107.

[4] R.E. Sanders, JOM 53 (2001) 21.

[5] L. Su, C. Lu, G. Deng, K. Tieu, Metall. Mater. Trans. B (2013) 345.

[6] S.H. Lee, Y. Saito, T. Sakai, H. Utsunomiya, Mater. Sci. Eng. A 325 (2002) 228.

[7] H.W. Höppel, J. May, M. Göken, Adv. Eng. Mater. 6 (2004) 781.

[8] L. Peng, L. Yajiang, G. Haoran, W. Juan, Mater. Lett. 59 (2005) 2001.

[9] Y. Li, P. Liu, J. Wang, H. Ma, Vacuum 82 (2007) 15.

[10] Z. Stradomski, Metabk 42 (2003) 185.

[11] H. Jiang, H. Zhang, K. Qin, J. Cui, Trans. Nonferrous Met. Soc. China 21 (2011) 1692.

[12] J.-C. Lee, H.-K. Seok, J.-Y. Suh, Acta Mater. 50 (2002) 4005.

[13] A. Gupta, S.T. Lee, R.B. Wagstaff, Mater. Technol. 22 (2007) 71.

[14] A. Gupta, S. Lee, R.B. Wagstaff, W.M. Gallerneault, J.W. Fenton, JOM 59 (2007) 62.

[15] N. Tedeschi, Adv. Mater. Process. (2007) 3.

[16] D.J. Lloyd, M. Gallerneault, R.B. Wagstaff, Metall. Mater. Trans. A 41 (2010) 2093.

[17] A.R. Baserinia, E.J.F.R. Caron, M.A. Wells, D.C. Weckman, S. Barker, M. Gallerneault, Metall. Mater. Trans. B 44 (2013) 1017.

[18] D.A. Porter, K.E. Easterling, Phase Transformations in Metals and Alloys, 2th ed., Chapman & Hall, London, 1995.

[19] T. Gladman, Mater. Sci. Technol. 15 (1999) 30.

[20] W.F. Miao, D.E. Laughlin, Scr. Mater. 40 (1999) 873.

[21] S. Esmaeili, X. Wang, D.J. Lloyd, W.J. Poole, Metall. Mater. Trans. A 34 (2003) 751.

[22] D.J. Lloyd, D.R. Evans, a. K. Gupta, Can. Metall. Q. 39 (2000) 475.

[23] K. Matsuda, Y. Uetani, T. Sato, S. Ikeno, Metall. Mater. Trans. A 32 (2001) 1293.

[24] E.F. Abo Zeid, Y.-T. Kim, Mater. Sci. Technol. 26 (2010) 440.

[25] C.D. Marioara, S.J. Andersen, T.N. Stene, H. Hasting, J. Walmsley, a. T.J. Van Helvoort, R. Holmestad, Philos. Mag. 87 (2007) 3385.

[26] D.J. Chakrabarti, D.E. Laughlin, Prog. Mater. Sci. 49 (2004) 389.

[27] S. Esmaeili, D.J. Lloyd, Scr. Mater. 50 (2004) 155.

[28] A. Gaber, A.M. Ali, K. Matsuda, T. Kawabata, T. Yamazaki, S. Ikeno, J. Alloys Compd. 432 (2007) 149.

[29] S. Esmaeili, D.J. Lloyd, Mater. Charact. 55 (2005) 307.

[30] P. Sepehrband, S. Esmaeili, Mater. Sci. Eng. A 487 (2008) 309.

[31] C.D. Marioara, S.J. Andersen, J. Jansen, H.W. Zandbergen, Acta Mater. 49 (2001) 321.

[32] W.F. Miao, D.E. Laughlin, Metall. Mater. Trans. A 31 (2000) 361.

[33] B. Raeisinia, W.J. Poole, D.J. Lloyd, Mater. Sci. Eng. A 420 (2006) 245.

[34] O.R. Myhr, Ø. Grong, H.G. Fjær, C.D. Marioara, Acta Mater. 52 (2004) 4997.

[35] D. Carron, P. Bastid, Y. Yin, R.G. Faulkner, Tech. Mech. (2010) 29.

[36] J.D. Robson, Mater. Sci. Technol. 20 (2004) 441.

[37] A. Deschamps, Y. Brechet, Acta Mater. 47 (1999) 293.

[38] Y.H. Hou, Y.X. Gu, Z.Y. Liu, Y.T. Li, X. Chen, Trans. Nonferrous Met. Soc. China 20 (2010) 863.

[39] M. Perez, M. Dumont, D. Acevedo-Reyes, Acta Mater. 56 (2008) 2119.

[40] J.C. Werenskiold, A. Deschamps, Y. Bre, Mater. Sci. Eng. A 293 (2000) 267.

[41] S. Esmaeili, D.J. Lloyd, W.J. Poole, Acta Mater. 51 (2003) 2243.

[42] O.R. Myhr, Ø. Grong, S.J. Andersen, Acta Mater. c (2001) 65.

[43] S. Esmaeili, D. Lloyd, Acta Mater. 53 (2005) 5257.

[44] X. Mn, Y.B. Kim, Y.H. Chung, K.K. Cho, Scr. Mater. 36 (1997) 111.

[45] F.J. Humphreys, Met. Sci. (1979) 136.

[46] C.M. Hefferan, J. Lind, S.F. Li, U. Lienert, A.D. Rollett, R.M. Suter, Acta Mater. 60 (2012) 4311.

[47] R.A. Vandermeer, D. Juul Jensen, Acta Mater. 49 (2001) 2083.

[48] S.J. Hales, T.R. Mcnelley, Acta Met. 36 (1988) 1229.

[49] R.D. Doherty, D.A. Hughes, F.J. Humphreys, J.J. Jonas, D.J. Jensen, M.E. Kassner, W.E. King, T.R. McNelley, H.J. McQueen, A.D. Rollett, Mater. Sci. Eng. A 238 (1997) 219.

[50] A. Duckham, O. Engler, R.D. Knutsen, Acta Mater. 50 (2002) 2881.

[51] R. Roumina, C.W. Sinclair, Acta Mater. 58 (2010) 111.

[52] F.J. Humphreys, M. Hatherly, Recrystallization and Related Annealing Phenomena, 2th ed., Oxford, UK, 2004.

[53] H. Frank, Recrystallization of Metallic Materials, 2th ed., Stuttgart, 1978.

[54] J.D. Robson, D.T. Henry, B. Davis, Acta Mater. 57 (2009) 2739.

[55] R. Higginson, P. Bate, Acta Mater. 47 (1999) 1079.

[56] E. Koken, N. Chandrasekaran, J.D. Embury, G. Burger, Mater. Sci. Eng. A 104 (1988) 163.

[57] J.G. Morris, W.C. Liu, JOM (2005) 44.

[58] J. Li, W.C. Liu, T. Zhai, E. a. Kenik, Scr. Mater. 52 (2005) 163.

[59] R.A. Eivani, H. Ahmed, J. Zhou, J. Duszczyk, Metall. Mater. Trans. A 40 (2009) 2435.

[60] K. Nagahama, I. Miki, Trans. JIM 15 (1974) 185.

[61] M. Somerday, F.J. Humphreys, Mater. Sci. Technol. 19 (2003) 20.

[62] E. Procedures, J.M. Howe, Metall. Trans. A 17 (1986) 593.

[63] H.E. Vatne, O. Engler, E. Nes, Mater. Sci. Technol. 13 (1997) 93.

[64] S. Tangen, K. Sjølstad, T. Furu, E. Nes, Metall. Mater. Trans. A 41 (2010) 2970.

[65] W.C. Liu, B. Radhakrishnan, Mater. Lett. 64 (2010) 1829.

[66] E. Nes, N. Ryum, O. Hunderi, Acta Mater. 33 (1985) 11.

[67] E.A. Grey, G.T. Higgins, Acta Metall. 21 (1973) 309.

[68] Y. Huang, F.J. Humphreys, Mater. Chem. Phys. 132 (2012) 166.

[69] M. Hillert, B. Sundman, Acta Metall. 24 (1976) 731.

[70] A. Lens, C. Maurice, J.H. Driver, Mater. Sci. Eng. A 403 (2005) 144.

[71] S.G. Kim, Y.B. Park, Acta Mater. 56 (2008) 3739.

[72] M.J. Jones, F.J. Humphreys, Acta Mater. 51 (2003) 2149.

[73] R. Kirchheim, Acta Mater. 55 (2007) 5139.

[74] K. Lucke, H.P. Stuwe, Acta Metall. 19 (1971) 1087.

[75] M. Hillert, Acta Mater. 52 (2004) 5289.

[76] J.W. Chan, Acta Metall. (1962) 789.

[77] Y. Birol, Scr. Mater. 59 (2008) 611.

[78] M. Karilik, T. Manik, M. Slamova, H. Lauschamann, Acta Phys. Pol. A 122 (2012) 469.

[79] F. Gatto, G. Camona, M. Conserva, P. Fiorini, Mater. Sci. Eng. (1968) 56.

[80] W.C. Liu, J.G. Morris, Mater. Met. Trans. A 36 (2005) 2829.

[81] R.K. Singh, A.K. Singh, Scr. Mater. 38 (2000) 1299.

[82] A. Yamamoto, M. Tsukamoto, D. Okai, Mater. Trans. 52 (2011) 876.

[83] K. Teichmann, C.D. Marioara, K.O. Pedersen, K. Marthinsen, Mater. Sci. Eng. A 565 (2013) 228.

[84] J. Go, M. Militzer, W. Poole, Proc. 12th Int. Conf. Alum. Alloy. (2010) 1153.

[85] B. Poorganji, P. Sepehrband, H. Jin, S. Esmaeili, Scr. Mater. 63 (2010) 1157.

[86] L.P. Troeger, Starke Jr E.A., Mater. Sci. Eng. A 293 (2000) 19.

[87] S.J. Lillywhite, P.B. Prangnell, F.J. Humphreys, Mater. Sci. Technol. 16 (2000) 1112.

[88] D.J. Lloyd, Met. Sci. 16 (1982) 304.

[89] X.X. Chen, P.D. Wu, D.J. Lloyd, J.D. Embury, Y. Huang, J. Appl. Mech. 77 (2010) 041015.

[90] E. Foroozmehr, S. Esmaeili, D.J. Lloyd, M. Gallerneault, Metall. Mater. Trans. A 43 (2012) 1770.

[91] C.Y. Barlow, P. Nielsen, N. Hansen, Acta Mater. 52 (2004) 3967.

[92] C.M. Cepeda-Jiménez, M. Pozuelo, O. a. Ruano, F. Carreño, Mater. Sci. Eng. A 490 (2008) 319.

[93] M.C. Chen, H.C. Hsieh, W. Wu, J. Alloys Compd. 416 (2006) 169.

[94] J.S. Chang, S. Shin, Mater. Sci. Forum 693 (2011) 457.

[95] D.M. Turriff, S.F. Corbin, M. Kozdras, Acta Mater. 58 (2010) 1332.

[96] S.C.V. Lim, a. D. Rollett, Mater. Sci. Eng. A 520 (2009) 189.

[97] L. Meng, S.P. Zhou, F.T. Yang, Q.J. Shen, M.S. Liu, Mater. Charact. 47 (2001) 269.

[98] M.Z. Quadir, M. Ferry, O. Al-Buhamad, P.R. Munroe, Acta Mater. 57 (2009) 29.

[99] C.-S. Tsao, C.-Y. Chen, U.-S. Jeng, T.-Y. Kuo, Acta Mater. 54 (2006) 4621.

[100] L. Zhen, W.D. Fei, J. Mater. Sci. 2 (1895) 1895.

[101] X. Wang, S. Esmaeili, D.J. Lloyd, Metall. Mater. Trans. A 37 (2006) 2691.

[102] H. Proudhon, W.J. Poole, X. Wang, Y. Bréchet, Philos. Mag. 88 (2008) 621.

[103] J.P. HIRTh, L. Kubin, Dislocation in Solids, 1st ed., North Holland, 2009.

[104] W. Donlon, C. Wolverton, J.W. Jones, J.E. Allison, Metall. Mater. Trans. A 35 (2004) 2407.

[105] R. Ahhaschian, L. Abbaschian, R.E. Reed-Hill, Physical Metallurgy Principles, 4th ed., Cengage Learning, Inc. US, 2009.

[106] D.A. Porter, K.E. Easterling, Phase Transformations in Metals and Alloys, Chapman & Hall, 1995.

[107] J.D. Robson, Acta Mater. 52 (2004) 4669.

[108] E. V Mathew, K.P. Gupta, S. Das, J. Mater. Sci. Lett. 3 (1984) 605.

[109] H.-W. Huang, B.-L. Ou, Mater. Des. 30 (2009) 2685.

[110] A.K. Jena, J. Mater. Sci. 16 (1981) 2544.

[111] Y.J. Li, L. Arnberg, Acta Mater. 51 (2003) 3415.

[112] Y.J. Li, A.M.F. Muggerud, A. Olsen, T. Furu, Acta Mater. 60 (2012) 1004.

[113] D.T.L. Alexander, A.L. Greer, Acta Mater. 50 (2002) 2571.

[114] M. Cabibbo, E. Evangelista, M. Vedani, Metall. Mater. Trans. A 36 (2005) 1353.

[115] B. Dutta, E.J. Palmiere, C.M. Sellars, Acta Mater. 49 (2001) 785.

[116] S. Farè, N. Lecis, M. Vedani, J. Metall. 2011 (2011) 1.

[117] V. Fallah, J. Stolle, N. Ofori-Opoku, S. Esmaeili, N. Provatas, Phys. Rev. B 86 (2012) 134112.

[118] S.P. Chen, N.C.W. Kuijpers, S. van der Zwaag, Mater. Sci. Eng. A 341 (2003) 296.

[119] K. Teichmann, C.D. Marioara, S.J. Andersen, K. Marthinsen, Metall. Mater. Trans. A 43 (2012) 4006.

[120] P.B. Prangnell, J.S. Hayes, J.R. Bowen, P.J. Apps, P.S. Bate, Acta Mater. 52 (2004) 3193.

[121] S.P. Chen, I. Todd, S. Van Der Zwaag, Metall. Mater. Trans. A 33 (2002) 529.

[122] H.E. Vante, T. Furu, E. Nes, Proc. Int. Conf. (1996) 21.

[123] P.R. Rios, F.S. Jr., H.R.Z. Sandim, R.L. Plaut, A.F. Padilha, Mater. Res. 8 (2005) 225.

[124] R.D. Doherty, R.W. Cahn, J. Less-Common Met. 28 (1972) 279.

[125] H. Jazaeri, F.J. Humphreys, Acta Mater. 52 (2004) 3239.

[126] S.P. Bellier, R.D. Doherty, Acta Mater. 25 (1977) 521.

[127] E. Koken, J. D.Embury, T.R. Ramachandran, T. Malis, Scr. Metall. 22 (1988) 99.

[128] O. Engler, X.W. Kong, P. Yang, Scr. Mater. 37 (1997) 1665.

[129] I. Baker, J.W. Martin, J. Mater. Sci. 15 (1980) 1533.

[130] H.E. Vatne, S. Benum, O. Daaland, E. Nes, Textures Microstruct. 26-27 (1996) 385.

[131] P.A. Beck, P.R. Sperry, J. Appl. Phys. 21 (1950) 150.

[132] A.R. Jones, B. Ralph, N. Hansen, Proc. R. Soc. Lond. A 368 (1979) 345.

[133] P. Bate, B. Hutchinson, Scr. Mater. 36 (1997) 195.

[134] H.W.F. Hellerp, C.A. Verbraaks, B.H. Kolster, Acta Met. 32 (1984) 1395.

[135] R.L. Higginson, M. Aindow, P.S. Bate, Mater. Sci. Eng. A 225 (1997) 9.

[136] M.C. Theyssier, J.H. Driver, Mater. Sci. Eng. A 272 (1999) 73.

[137] M. Somerday, F.J. Humphreys, Mater. Sci. Technol. 19 (2003) 30.

[138] Q. Zeng, X. Wen, T. Zhai, Metall. Mater. Trans. A 40 (2009) 2488.

[139] P.N. Rao, S.K. Panigrahi, R. Jayaganthan, Mater. Sci. Technol. 26 (2010) 371.

[140] P. Sepehrband, S. Esmaeili, Scr. Mater. 63 (2010) 4.

[141] R. Hu, T. Ogura, H. Tezuka, T. Sato, Q. Liu, J. Mater. Sci. Technol. 26 (2010) 237.

[142] S. Esmaeili, D.J. Lloyd, H. Jin, Mater. Lett. 65 (2011) 1028.

[143] G. Burger, A.K. Gupta, L. Sutak, D.J. Lloyd, Mater. Sci. Forum 217-222 (1996) 471.

[144] R. Guemini, A. Boubertakh, G.W. Lorimer, J. Alloys Compd. 486 (2009) 451.

[145] R. Kaibyshev, F. Musin, D. Gromov, T.G. Nieh, D.R. Lesuer, Mater. Sci. Technol. 19 (2003) 483.

[146] O. Engler, J. Hirsch, Mater. Sci. Eng. A 336 (2002) 249.

[147] P. Babaghorbani, W.J. Poole, M.A. Wells, N.C. Parson, in:, 13th Int. Conf. Alum. Alloy., 2012, p. 3.

[148] M. Bijak, H. Paul, J.H. Driver, J. Microsc. 237 (2010) 221.

[149] Y. Birol, Scr. Mater. 60 (2009) 5.

[150] P. Furrer, G. Hausch, Met. Sci. (1979) 155.

[151] H.W. Huang, B.L. Ou, C.T. Tsai, Mater. Trans. 49 (2008) 250.

[152] Y. Kwag, J.G. Morris, Mater. Sci. Eng. 77 (1986) 59.

[153] J. Liu, J.G. Morris, Metall. Mater. Trans. A 34 (2003) 2029.

[154] Q. Liu, Z. Yao, A. Godfrey, W. Liu, J. Alloys Compd. 482 (2009) 264.

[155] P. Rangel, A. Fernando, Mater. Res. 6 (2003) 605.

[156] R.L. Higginson, M. Aindow, P.S. Bate, Philos. Mag. Lett. (2006) 37.

[157] X. Xia, Scr. Metall. Mater. 28 (1993) 1213.

[158] Y. Ping, O. Engler, G. Gottstein, Trans. Nonferrous Met. Soc. China 8 (1998) 363.

[159] FactSage 6.3, (2012).

[160] W.C. Yang, M. Wang, Y. Jia, R. Zhang, Metall. Mater. Trans. A 42 (2011) 2917.

[161] T. Miyazaki, S. Kobayashi, T. Koyama, Metall. Mater. Trans. A 30 (1999) 2783.

[162] S. Esmaeili, D.J. Lloyd, Mater. Sci. Forum 169 (2006) 519.

[163] S. Esmaeili, D.J. Lloyd, W.J. Poole, Mater. Lett. 59 (2005) 575.

[164] D.G. Morris, J. Mater. Res. (2006) 329.

[165] X. Li, M.E. Kassner, S.C. Bergsma, JMEPEG 9 (2000) 416.

[166] P. Sepehrband, Ph.D Thesis, University of Waterloo, 2010.

[167] Metals Handbook, 9th ed., Oh., 1990.

[168] F.J. Humphreys, J. Mater. Sci. 36 (2001) 3833.

[169] H. Zhang, L. Li, D. Yuan, D. Peng, Mater. Charact. 58 (2007) 168.

[170] H. Inagaki, Mater. Sci. Forum 558-559 (2007) 77.

[171] N.C.W. Kuijpers, F.J. Vermolen, C. Vuik, P.T.G. Koenis, K.E. Nilsen, S. Van Der Zwaag, Mater. Sci. Eng. A 394 (2005) 9.

[172] S. De La Chapelle, P. Duval, Textures Microstruct. 35 (2002) 55.

[173] R.D. Doherty, Met. Sci. 8 (1974) 132.

[174] B. Radhakrishnan, G. Sarma, Philos. Mag. 84 (2004) 2341.

[175] C. Schäfer, J. Song, G. Gottstein, Acta Mater. 57 (2009) 1026.

[176] A.R. Jones, B. Ralph, N. Hansen, Proc. R. Soc. Lond. A 368 (1979) 345.